ACTA METALLURGICA SLOVACA
2021, VOL. 27, NO. 2, 47-52

RESEARCH PAPER

MICROSTRUCTURE, MECHANICAL AND TRIBOLOGICAL BEHAVIOUR OF AISI 316L STAINLESS STEEL DURING SALT BATH NITRIDING

Elhadj Ghelloudj [1*]

[1] *Department of industrial mechanics, SH/DP Regional Direction Haoud Berkaoui, Ouargla 30000, Algeria*

*Corresponding author: hadjhadj105@gmail.com, tel.: +213676407456, *Department of industrial mechanics, SH/DP Regional Direction Haoud Berkaoui, Ouargla 30000, Algeria*

Received: 26.04.2021
Accepted: 08.05.2021

ABSTRACT

The current work aimed to analyze the impact of salt bath nitriding on the behavior of the tribological characteristics and surface microstructures of AISI 316L stainless steels. Nitriding was carried out at 580 °C for 10 h. The tribological, structural behavior of the AISI 316L before and after salt bath nitriding was compared. The surface microstructures, tribological characteristics, as well as its surface hardness, were investigated using optical microscopy (OM), X-ray diffractometer (XRD), surface profilometer, pin-on-disk wear tester, and microhardness tester. In the current work, the experimental results showed that a great surface hardness could be achievable through the salt bath nitriding technique because of the formation of the so-called expanded Austenite (S-phase), the nitrogen diffusion region. The surface hardness of AISI 316 stainless steel after the nitriding process reached 1100 HV0.025 which was six times the untreated sample hardness. The S-phase is additionally expected to the improvement of wear resistance and decrease the friction coefficient.

Keywords: AISI 316L stainless steel; Friction coefficient; Salt bath nitriding; Surface hardness; S-phase; Wear resistance

INTRODUCTION

Austenitic stainless steel is one of the four categories of stainless steel alloy: austenitic [1], ferritic [2], martensitic and duplex [3, 4]. The austenitic group of stainless steel has a major composition of chromium, nickel, manganese steel, and minor amounts of other additional alloy elements [5, 6]. Because of their exceptionally high toughness [7], good ductility [8,9], formability [10], thermal conductivity [11], good welding properties [12], nonmagnetic properties [13], high impact energy, and great corrosion resistance [14-16] they are widely used in applications of low-temperature technology [17] such as orthopedic [18] industries, ocean technology [19], aerospace [20], food processing equipment [21], nuclear reactors [22, 23], manufacturing of several parts of automotive [24], petrochemical processing [25], etc.

Austenitic stainless steels, which incorporate the AISI 316L stainless steel, have many applications in the industry due to their good mechanical characteristics and their exceptional corrosion resistance [26], especially in certain environments. Low hardness and poor wear resistance [27] are some of the main drawbacks of austenitic stainless steels and are therefore subject to various types of surface characteristics failure [28]. Because of the limited tribological properties of these alloys (poor wear resistance), their scope of industrial applications was limited [29]. Several studies have shown that nitriding treatment has produced a hard surface layer resulting in improved wear resistance. Thus, the nitriding treatment is a perfect alternative for raising the surface hardness, This ensures the efficacy of the wear resistance characteristic when this is required in service [30]. Nitriding is one of the forms of surface treatments used to improve the surface properties of materials [31]. This technique also improves the hardness, mechanical properties, and fatigue strength, and wear and corrosion resistance of various tools [32]. According to [33], nitriding is a thermochemical process through which nitrogen atoms are diffused and dispersed at the surface level of the materials at a proper temperature, which leads to an increase in the surface hardness and as a result increases the performance and the life span of the industrial parts. There are different methods of nitriding operations such as salt bath nitriding (SBN) [34-36], gas nitriding (GN) [37, 38], and plasma nitriding (PN) [39, 40]. A literature survey can easily find several hundred papers published over the last few years on the topic of nitriding of austenitic stainless steel [41-43]. The most common nitriding techniques are a salt bath with a nitrogen concentration-rich medium. This thermochemical process has been used to creating the required properties on the surface of stainless steels as such wear [44], fatigue [45], corrosion [46], and friction properties [47]. The medium used in salt bath nitriding is a salt that contains nitrogen, such as cyanide salt, or potassium nitrate. Salt baths with cyanide have the same, or even greater, nitrogen potential than ammonia. The nitriding behavior can be defined fairly through the diffusion of nitrogen into the parts. Most nitrogen is interstitially absorbed during nitriding. Minor oxidation was observed following nitriding. It can be considered a nitrocarburizing treatment since the salts used often typically contribute carbon to the surface of the workpiece, and the two elements generally permeate into the surface of the industrial parts [48]. There have been researched studies of the effects of nitriding treatments on the behavior of surface microstructure and characteristics of austenitic stainless steel such as AISI 304 [49,50], AISI 304L [51], AISI 321 [52], AISI 201 [53], AISI 316 [54], AISI 316L [55,56], AISI 202

[57], AISI 316LN [58] and AISI 316LVM [59], AISI 310[60], AISI 303[61], AISI 204[62]. However, there is a lack of research about the surface microstructural and tribological behavior of AISI 316L stainless steel during salt bath nitriding by the Tenifer process (TF1) at 580 °C. Therefore, in the present work, the structural and tribological behavior of AISI 316L stainless steel before and after salt bath nitriding (Tenifer) was investigated. The tribological properties and surface structures formed during nitriding were investigated using X-ray diffraction (XRD), microhardness tester, pin-on-disk wear test, surface profilometer, and optical microscopy (OM). The primary objective of the present study is to investigate the effect of salt bath nitriding by the Tenifer process (TF1) at 580 °C on tribological properties and surface microstructure of AISI 316L stainless steel.

MATERIALS AND METHODS

Material and salt bath nitriding processes

The material used in the present research was AISI 316L austenitic stainless steel with the chemical composition shown in Table 1. The specimens for the experiment were machined into dimensions of 30 mm × 10 mm × 5 mm.

Table 1 The chemical compositions of the AISI 316L used in this study (wt %)

C	Si	Mn	P	S	Mo	Cr	Ni	Fe
0.02	0.52	1.52	0.029	0.024	2.09	16.76	10.14	bal

The salt bath nitriding by Tenifer treatments was performed in a DEGUSSA furnace. A small gap was made in each sample with a diameter of about 2 mm, which could be attached to the end of a metal wire for easier get her out of the furnace. As usual, when processing required parts in the industry by salt bath nitriding (Tenifer TF1), The AISI 316L stainless steel samples were preheated to 350 °C for 30 min in preheating tank oven, after that nitriding process was performed at 580 °C for 10 h in the salt bath comprising of cyanates (36 ± 2 %), carbonates (19 ± 2 %) and cyanides (0.8 %). There is a reaction between the molten salt and the AISI 316L stainless steel specimens being processed during the salt bath nitriding process so that nitrogen and carbon are absorbed and diffused through the surfaces of the specimen.

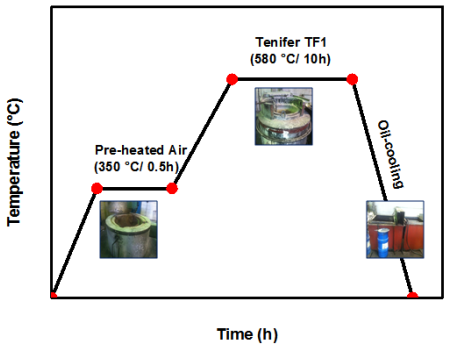

Fig. 1 Temperature - time plot for salt bath nitriding treatment

The emerging nitrogen used for the reaction of nitriding treatment coming out of the dissociation of Cyanate: $4CNO^- \rightarrow CO_3^{-2} + 2CN^- + CO + 2[N]$. The gradual change in the concentration between the surface of the specimen and the nitriding salt bath turns out to be the main thrust for the effective nitrogen atom to penetrate an austenite structure, which leads to the formation of a surface nitride layer. At the same time, a few emerging carbons, which come out during the dissociation of Carbon monoxide: $2CO \rightarrow CO_2 + [C]$, also penetrates austenite structure along with nitrogen. The parameters and processing of nitriding treatment are illustrated in Fig. 1.

Characterizations of the surface treatments

The samples treated with salt bath nitriding were analyzed using optical microscopy examination, microhardness measurements, X-ray diffraction analysis, surface profilometer, and wear tests under dry conditions. The microstructure on the cross-section of nitrided samples was analyzed after metallographic preparation and etching with 2% NITAL (2% HNO_3 in ethanol). The surface microstructure analysis was investigated by optical microscopy (GA-120). Measurements of microhardness profiles were obtained before nitriding using a microhardness tester fitted with a Vickers indentation with a load of 25 gf. This was also used for surface hardness measurements of the specimens treated. Averaging at least 3 measurements was used to determine the hardness value of samples. The surface profilometer was used for measuring and analyzing the surface roughness of treated and untreated specimens of AISI 316L stainless steel. According to ISO 4287:1997 standard, surface roughness was defined by measuring the parameters of surface roughness (Ra, Rq, and Rz). The tribological behaviors (friction and wear) of untreated and treated specimens of 316L stainless steel were evaluated under unlubricated condition by a pin-on-disk tribometer, in which the sample (disc) was rotated against a stationary steel ball as the pin of 5 mm diameter with a speed of 60 revs/min at a load of 5 N. The weight loss of the sample was evaluated using an electronic balance accurate to 0.1 mg.

RESULTS AND DISCUSSION

Surface microstructure analyses

Fig. 2 displays the cross-section microstructure of the sample of AISI 316L stainless steel, which was treated at the salt bath nitriding temperature of 580 °C for 10 h. As shown in the figure, the Tenifer nitrided surface (Researchers call it the "expanded austenite" or " S-phase) appears to have a multi-phase structure judged from the variations in layer composition. The average thickness of this layer was about 72 µm. A clear boundary existed between the top layer and the inner layer, the upper layer made up of a hardened layer of around 6 µm depth, accompanied by a slightly etched layer of around 66 µm depth. Further, the topmost layer (Rich in nitrogen) was bright, while the inner layer was completely darkened due to the Nital etching. Possibly the dark zone in the inner layer is caused by precipitation from CrN. This result ties well with previous studies wherein Gui et al. [63] detailed the nitrided morphology of AISI 316LSS using the optical microscope at 580 °C for 2h under salt bath nitrocarburizing. It was shown that the surface layer consists of Cr2N/ γ'-Fe_4N and CrN/ γ -Fe. In another study, Jiang et al. [64] detailed the surface microstructure of AISI 316 produced during salt bath nitrocarburizing but at low temperature (480 °C) for 6 h. They observed that the S-phase was formed and this nitrocarburized matrix zone was darkened after Nital etching.

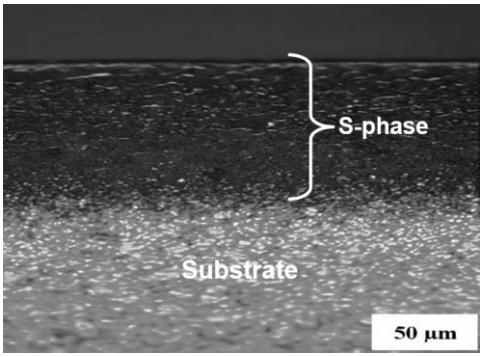

Fig. 2 Typical optical micrographs of the cross-section of AISI 316L after nitriding at 580 °C for 10h

Fig. 3 below illustrates a comparison of the XRD diffraction pattern of AISI 316 stainless steel between the sample that was treated by salt bath nitriding and the untreated sample. It has been shown to the untreated sample has a Face Centred Cubic crystal structure (γ-Fe) which was expected because the Austenitic stainless steels possess austenite as their primary crystalline structure (face-centered cubic). The nitrided sample at 580 °C has been characterized by the appearance of other phases, where a set of peaks, which do not match any existing ASTM X-ray diffraction index was distinguished. These peaks in this figure correspond to the S-phase (γN), chromium nitride phase (CrN), and formation of Fe_4N compound.

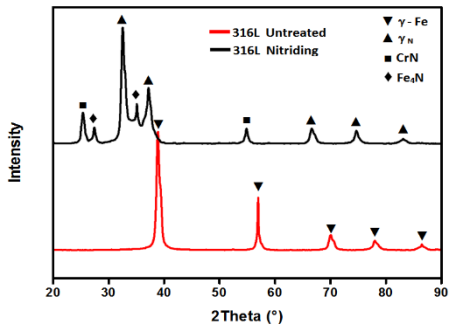

Fig. 3 Typical X-ray diffraction patterns of AISI 316 L SS before and after salt bath nitriding at 580 °C for 10h

It can be seen that the corresponding peaks of the expanded austenite phase are broadened and turned to lessen angles compared to peaks of untreated austenitic stainless steel. The crystal structure of the S-phase also has a face-centered cubic structure, the S-phase was formed due to the incorporation of the nitrogen atoms in the interstitial positions and gaps of the austenite structure. Overall these findings are following results reported by many studies [55, 56].

In addition, the appearance of CrN nitride at 580 °C. It was consistent with the conclusions stated in [53], which noted that at relatively high temperatures CrN nitride is favorably precipitated. The formation of CrN could be explained in the following form: Chromium appears as a solid solution in austenite steel, which emerges as the temperature increases of solid solution due to the contrast between the thermal properties of iron and chromium [65]. Furthermore, the comparatively low concentration of CNO^- (approximately 36%) in the cyanide-cyanate during the Tenifer (TF1) process is likely that the cause for the formation of the γ'-Fe_4N compound rather than the ε-Fe_2 (N, C).

Surface hardness profile

Fig. 4 shows the microhardness profiles presented as a function of the depth of AISI 316L stainless steel after the salt bath nitriding process by the Tenifer method (at 580 °C for 10h). As can see, the maximum microhardness obtained is up to 1100 HV0.025, while the substrate possesses a microhardness of approximately 200 HV0.025. Besides that, according to the graph, it can be seen that the hardness decreases progressively as the depth increases until it approaches hardness values to those of the untreated sample. The increase in hardness as a result of the gas nitriding process has been reported previously by Mahmoud et al. [66], where they found that the AISI 316L after the nitriding process have greater microhardness than compared to the untreated sample. A value surface hardness of about 1400 HV0.025 of the AISI 316L during nitrocarburizing has also been reported by Pinedo et al. [67].

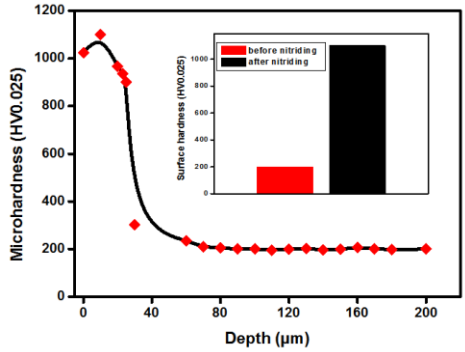

Fig. 4 Hardness profiles in the surface layer of the specimen after salt bath nitriding for 10h at 580 °C

Diffuse nitrogen has strong properties to improve material hardness. Both the hardness values and the nitrogen concentration decreased monotonously with increasing depth of the treated sample surface [68]. The high content of nitrogen is dissolved in austenite (S-phase), in which intensive precipitation of chromium nitride subsists, which significantly improves the hardness property. According to Fader et al. [69], the increase in nitride layer hardness is attributable to the higher nitrogen concentration, larger grain structure, and the appearance of expanded austenite in those regions. The core hardness values of the specimen nitrided before treated by salt bath nitriding were 200 HV0.025. It is noteworthy that the core hardness of the nitrided specimen was measured at the same level as for the specimen nitrided before nitriding in the salt bath (200 HV0.025). This confirms that during nitriding treatment the core of AISI 316Ldoes not soften by nitriding parameters (treatment time and temperature), i.e. microstructure of the core remains unchanged after nitriding of the salt bath.

Surface roughness measurement

Fig. 5 summarizes the average values of surface roughness parameters characterizing the surface topography (Ra, Rq, and Rz) of the untreated and treated samples, it can be observed an

important increase in the surface roughness values of the 316L stainless steel sample during the salt bath nitriding.

The average roughness value of arithmetic mean deviation of the roughness profile (Ra) of the sample nitrided was 0.366 µm, were higher almost 6 times than the average roughness of the sample before treatment. On the other hand, for the square mean deviation of the roughness profile (Rq), the roughness value was 0.574 µm, which was about 6.5 times higher than that of the untreated one. In addition to this, the roughness value of the maximum distance between the lowest and the highest points of the roughness profile (Rz) of the sample nitrided was 5.32 µm, which was about 3 times larger than the of the untreated sample. The increased surface roughness during salt bath nitriding can be attributed to the formation of the sliding bands on the nitrided sample due to the formation of the expanded austenite (S-phase). This result ties well with the previous study reported by Gajendra et al. [70] explained that the increased surface roughness of austenitic stainless steel during plasma nitriding could be due to the high chemical propagation average of hydrogen atoms by plasma in the nitrided layers especially the expanded austenite.

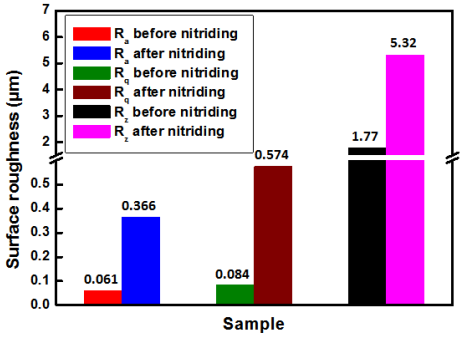

Fig. 5 Surface roughness parameters (Ra, Rq and Rz) before and after salt bath nitriding at 580 °C for 10h

Tribological characteristics

In this work, the friction behavior on the non-nitrided sample surface has been compared with those on the treated sample surface. The variation of friction coefficient measured against a steel ball is illustrated in Fig. 6 for the specimens of AISI 316L before and after salt bath nitriding in terms of rolling distance. At the beginning of the experiment, the coefficient of friction in both salt bath nitrided and untreated samples had a relatively high value, where the values of friction coefficients were 0.45 µm and 0.47 µm, respectively. This is due to the presence of initial static friction. After that, it was found in each sample that the coefficient of friction increased when the test time increases to a relatively constant value (by neglecting minor changes). The average friction coefficient values for the salt bath nitrided sample are approximately 0.486 µm while its value is approximately 0.528 µm for the untreated one.

From the results obtained, it can be said that the friction coefficient of the AISI 316L stainless steel sample was reduced utilizing surface hardening during salt bath nitriding as much as possible. In addition, the behavior of untreated material friction coefficient can be ascribed to adhesion wear that occurred as the result of increased contact temperature and welding points on the surface.

According to Zhang et al. [71], the low friction coefficient measured for the nitrided specimen can be credited to the increase of the surface hardness. Also, Yetim et al. [72] indicated that there in an S-phase with perfect friction-resistant properties in the surface microstructure of AISI 316L stainless steel after nitriding treatment which significantly reduces the values of the coefficient of friction.

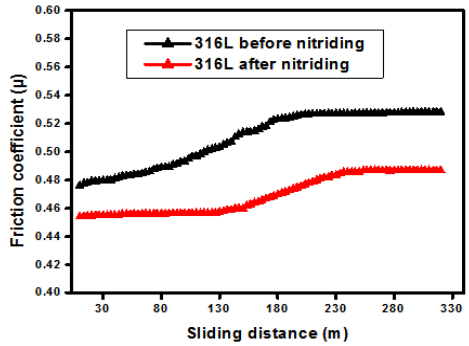

Fig. 6 Variations of friction coefficient of untreated and nitrided specimens of AISI 316L

Fig. 7 illustrates the results of the wear behavior of the nitriding treatment specimen of the AISI 316L compared with the untreated sample under the various dry sliding conditions were measured using a tribometer. It can be observed that, as predicted, the nitrided specimen had the highest wear resistance compared to the untreated one. for example, before salt bath nitriding the loss in weight increased 30 mg for 300 m of the sliding distance, while after salt bath nitriding the loss in weight increased 20 mg for 300 m of the sliding distance. This result ties well with previous studies wherein were confirmed that the resistance of wear resistance was attributable to the surface hardness of materials. Higher-hardness materials usually displayed greater wear resistance. According to Fig. 4, we know that the hardness of alloying elements nitride phase's fine particles (S-phase, CrN and γ' -Fe_4N) in the surface of nitrided sample during salt bath nitriding is more than 1100 HV0.025, that is about six times harder than that of the untreated one. Thus, the nitrided sample was expected to have better resistance to wear [73-76].

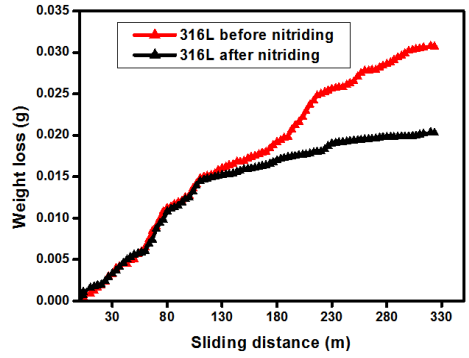

Fig. 7 Variation of weight loss against the sliding distance of AISI 316L SS before and after nitriding at 580 °C for 10h

CONCLUSION

The main goal of this work is to study the surface microstructure, tribological and mechanical behavior of AISI 316L austenite stainless steel at 580 °C during salt bath treatment by Tenifer processing (TF1). The results of this study can be summarized as:

The salt bath nitrided layer was composed of three sublayers, namely the CrN layer, the γ'-Fe_4N layer, and γ_N layer (S-phase).

The salt bath nitriding can very efficiently increase the hardness of the surface of AISI 316L. Maximum values obtained of the nitrided surface approximately 1100 HV0.025 for 10 h, which is around 6 times as hard as the untreated sample (200 HV0.025).

The surface roughness (Ra, Rq and Rz) is increased when compared with the "base material" condition after the salt bath nitriding by Tenifer processing.

The Tenifer process (TF1) can progress the resistance of wear and reduces the friction coefficient of the material under study.

ACKNOWLEDGMENTS

This research was supported by Sonatrach Haoud Berkaoui, Ouargla, Algeria and department of mechanical engineering, University Abbes Laghrour, Khenchela, Algeria

REFERENCES

1. S.H.Muhammad, N.S. Safaa, H. Esah, F.M. Moh.: Annales de Chimie - Science des Matériaux, 43(6), 2019, 369-375. https://doi.org/10.18280/acsm.430602
2. L.C. Gontijo, R.Machado, L.C. Casteletti, S.E. Kuri, P.A.P. Nascente: Materials Science Forum, 638-642, 2010, 775-780. https://doi.org/10.4028/www.scientific.net/msf.638-642.775
3. G. Prakash, S.K. Nath: Journal of Materials Engineering and Performance, 27(7), 2018, 3206-3216. https://doi.org/10.1007/s11665-018-3424-5
4. R. Huang, J. Wang, S. Zhong, M. Li, J. Xiong, H. Fan: Applied Surface Science, 271, 2013, 93-97. https://doi.org/10.1016/j.apsusc.2013.01.111
5. R.M. Oliveira, M. Ueda, I.H. Tan, L. Hoshida, C.B. Mello: Plasma Processes and Polymers, 4(S1), 2007, S655- S659. https://doi.org/10.1002/ppap.200731604
6. T. Czerwiec, H. He, G. Marcos, T. Thiriet, S. Weber, H. Michel: Plasma Processes and Polymers, 6(6-7), 2009, 401-409. https://doi.org/10.1002/ppap.200930003
7. K. Kwangyoon et al.: Metals, 8(11), 2018, 932 - 947. https://doi.org/10.3390/met8110932
8. J.C. Stinville, P. Villechaise, C. Templier, J.P. Riviere, M. Drouet: Surface and Coatings Technology, 204(12-13), 2010, 1947- 1951. https://doi.org/10.1016/j.surfcoat.2009.09.052
9. N. Karimzadeha, E.G. Moghaddam, M. Mirjani, K. Raeissi: Applied Surface Science, 283, 2013, 584-589. https://doi.org/10.1016/j.apsusc.2013.06.152
10. M.G. García et al.: Surface and Interface Analysis, 47(6), 2015, 728-737. https://doi.org/10.1002/sia.5770
11. W.M. Lima et al.: Journal of Physics: Condensed Matter, 17(7), 2005, 1239-1249. https://doi.org/10.1088/0953-8984/17/7/016
12. M. G. García et al.: Surface and Coatings Technology, 218, 2013, 142- 151. https://doi.org/10.1016/j.surfcoat.2012.12.043
13. A.S. Hamdy, B. Marx, D. Butt: Materials Chemistry and Physics, 126(3), 2011, 507-514. https://doi.org/10.1016/j.matchemphys.2011.01.037
14. I. Lee, A. Barua: Surface and Coatings Technology, 207, 2016, 1045-1052. https://doi.org/10.1016/j.surfcoat.2016.07.031
15. L.C. Gontijo, R. Machado, S.E. Kuri, L.C. Casteletti, P.A.P. Nascente: Thin Solid Films, 515(3), 2006, 1093-1096. https://doi.org/10.1016/j.tsf.2006.07.075
16. C.Y. Cui, J.D. Hu, Y.H. Liu, Z.X. Guo: Materials Science and Technology, 24(8), 2008, 964-968. https://doi.org/10.1179/174328408X322088
17. R. Bidulsky, et al.: Materials, 13(15), 2020, 3328. https://doi.org/10.3390/ma13153328
18. C.F. Hung, C.Z. Wu, W.F. Lee, K.L. Ou, C.M. Liu, P.W. Peng: Physics Procedia, 32, 2012, 914-919. https://doi.org/10.1016/j.phpro.2012.03.656
19. C. Paula et al.: Journal of Materials Research and Technology, 8(2), 2019, 1897-1906. https://doi.org/10.1016/j.jmrt.2019.01.006
20. M. Yakout, M.A. Elbestawi, S.C. Veldhuis: The International Journal of Advanced Manufacturing Technology, 95, 2018, 1953-1974. https://doi.org/10.1007/s00170-017-1303-0
21. D.S. Petrovič, D. Food and Bioproducts Processing, 100, 2016, 230-237. https://doi.org/10.1016/j.fbp.2016.07.006
22. T. Moskalioviene, A. Galdikas, J.P. Rivière, L. Pichon: Surface and Coatings Technology, 205(10), 2011, 3301- 3306. https://doi.org/10.1016/j.surfcoat.2010.11.060
23. P. Petrousek, et al: Acta Metallurgica Slovaca, 25(4), 2019, 283-290. https://doi.org/10.12776/ams.v25i4.1366
24. L. Ceschini, C. Chiavari, E. Lanzoni, C. Martini: Materials & Design, 38, 2012, 154-160. https://doi.org/10.1016/j.matdes.2012.02.019
25. Y.Y. Chen, Y.M. Liou, H.C. Shih: Materials Science and Engineering: A, 407(1-2), 2005, 114-126. https://doi.org/10.1016/j.msea.2005.07.011
26. K.H. Lo, C.H. Shek, J.K.L. Lai: Materials Science and Engineering R, 65(4-6), 2009, 39-104. https://doi.org/10.1016/j.mser.2009.03.001
27. M. Egawa, Y. Matsuda, N. Ueda, T. Sone, M. Tsujikawa, K. Nakata: Plasma Processes and Polymers, 6(S1), 2009, S893-S896. https://doi.org/10.1002/ppap.200932205
28. M. Peruzzo, F.L. Serafini, M.F.C. Ordoñez, R.M. Souza, M.C.M. Farias: Wear, 422-423, 2019, 108-118. https://doi.org/10.1016/j.wear.2019.01.027
29. C.E. Foerster et al.: Surface and Coatings Technology, 204(18-19), 2010, 3004-3008. https://doi.org/10.1016/j.surfcoat.2009.12.030
30. T. Watanabe, M. Kondo, A. Sagara: Electrochimica Acta, 58, 2011, 681-690. https://doi.org/10.1016/j.electacta.2011.10.014
31. S.K. Singh, C. Naveen, Y.V Sai, U. Satish, C. Bandhavi, R. Subbiah: Materials Today: Proceedings, 18, 2019, 2717-2722. https://doi.org/10.1016/j.matpr.2019.07.134
32. M. Dai, C. Li, J. Hu: Journal of Alloys and Compounds, 688, 2016, 350-356. https://doi.org/10.1016/j.jallcom.2016.07.189
33. Y.H. Qiang, S.R. Ge, Q.J. Xue: Journal of Materials Processing Technology, 101(1-3), 2000, 180-185. https://doi.org/10.1016/s0924-0136(00)00466-0
34. E. Ghelloudj, M.T. Hannachi, H. Djebaili: Acta Metallurgica Slovaca, 24(4), 2018, 280-286. https://doi.org/10.12776/ams.v24i4.1111
35. T. Peng, M. Dai, W. Cai, W. Wei, K. Wei, J. Hu: Applied Surface Science, 484, 2019, 610-615. https://doi.org/10.1016/j.apsusc.2019.04.134
36. W. Mei, J. Wu, M. Dai, K. Wei, J. Hu: Acta Metallurgica Slovaca, 25(2), 2019, 130-135. https://doi.org/10.12776/ams.v25i2.1271

37. A.R. Clauss, E. Bischoff, R.E. Schacherl, E.J. Mittemeijer: Materials Science and Technology, 26(3), 2010, 297-308. https://doi.org/10.1179/174328409x422266
38. P. Kochmański, J. Nowacki: Surface and Coatings Technology, 200(22-23), 2006, 6558-6562. https://doi.org/10.1016/j.surfcoat.2005.11.034
39. L. Wang, S. Ji, J. Sun: Surface and Coatings Technology, 200(16-17), 2006, 5067-5070. https://doi.org/10.1016/j.surfcoat.2005.05.036
40. E. Grigore, C. Ruset, X. Li, H. Dong: Plasma Processes and Polymers, 6(S1), 2009, S321-S325. https://doi.org/10.1002/ppap.200930703
41. L. Shen, L. Wang, J.J. Xu: Surface and Coatings Technology, 228, 2013, S456-S459. https://doi.org/10.1016/j.surfcoat.2012.05.026
42. S. Lu, X. Zhao, S. Wang, J. Li, W. Wei, J. Hu: Vacuum, 145, 2017, 334-339. https://doi.org/10.1016/j.vacuum.2017.09.020
43. E.D.L. Heras et al.: Plasma Processes and Polymers, 4(S1), 2007, S741-S745. https://doi.org/10.1002/ppap.200731809
44. D.C Wen: Wear, 268(3-4), 2010, 629-636. https://doi.org/10.1016/j.wear.2009.10.012
45. K. Funatani: Metal Science and Heat Treatment, 46(7-8), 2004, 277-281. https://doi.org/10.1023/b:msat.0000048834.48163.2e
46. K. Marušić, H. Otmačić, D. Landek, F. Cajner, E. Stupnišek-Lisac: Surface and Coatings Technology, 201(6), 2006, 3415-3421. https://doi.org/10.1016/j.surfcoat.2006.07.231
47. G. Pantazopoulos, P. Psyllaki, D. Kanakis, S. Antoniou, K. Papadimitriou, J. Sideris: Surface and Coatings Technology, 200(20-21), 2006, 5889-5895. https://doi.org/10.1016/j.surfcoat.2005.09.001
48. Y.Z. Shen, K.H. Oh, D.N. Lee: Scripta Materialia, 53(12), 2005, 1345-1349. https://doi.org/10.1016/j.scriptamat.2005.08.032
49. J. Wang, Y. Lin, Q. Zhang, D. Zeng, H. Fan: Metallurgical and Materials Transactions A, 45(10), 2014, 4525-4534. https://doi.org/10.1007/s11661-014-2418-7
50. X. Liu, C. Mao, M. Wu, W. Cai, M. Dai, J. Hu: Acta Metallurgica Slovaca, 26(1), 2020, 4-6. https://doi.org/10.36547/ams.26.1.458
51. G. Li et al.: Materials Characterization, 59(9), 2008, 1359-1363. https://doi.org/10.1016/j.matchar.2007.09.011
52. L. Bellas, G. Castro, L. Mera, J.L. Mier, A. García, A. Varela: Metal Science and Heat Treatment, 58(5-6), 2016, 369-375. https://doi.org/10.1007/s11041-016-0019-3
53. H.S. Luo, C. Zhao: Physics Procedia, 50, 2013, 38-42. https://doi.org/10.1016/j.phpro.2013.11.008
54. X. Zhang et al.: Metallurgical and Materials Transactions A, 49(1), 2018, 356-367. https://doi.org/10.1007/s11661-017-4382-5
55. M.F.C. Ordoñez et al.: Surface and Coatings Technology, 374, 2019, 700-712. https://doi.org/10.1016/j.surfcoat.2019.06.002
56. F. Borgioli: Metals, 10(2), 2020, 187-233. https://doi.org/10.3390/met10020187
57. F. Borgioli, E. Galvanetto, T. Bacci: Corrosion Science, 136, 2018, 352-365. https://doi.org/10.1016/j.corsci.2018.03.026
58. P. Rajendran, A. Devaraju: Materials Today: Proceedings, 5(6), 2018, 14333-14338. https://doi.org/10.1016/j.matpr.2018.03.016
59. E. Ura-Bińczyk, A. Krawczyńska, R. Sitek, M. Lewandowska: Surface and Coatings Technology, 375, 2019, 565-572. https://doi.org/10.1016/j.surfcoat.2019.07.035
60. R. Djellal, A. Saker, B. Bouzabata, D.E. Mekki: Surface and Coatings Technology, 325, 2017, 533- 538. https://doi.org/10.1016/j.surfcoat.2017.07.014
61. Y. Lin, W. Lan, K. Ou, C. Liu, P. Peng: Surface and Coatings Technology, 206(23), 2012, 4785- 4790. https://doi.org/10.1016/j.surfcoat.2012.03.089
62. D. Zeng, S. Yang, Z.D. Xiang: Applied Surface Science, 258(12), 2012, 5175-5178. https://doi.org/10.1016/j.apsusc.2012.01.167
63. G. Li et al.: Surface and Coatings Technology, 202(13), 2008, 2865-2870. https://doi.org/10.1016/j.surfcoat.2007.10.032
64. Z. Cheng, C.X. Li, H. Dong, T. Bell: Surface and Coatings Technology, 191(2-3), 2005, 195-200. https://doi.org/10.1016/j.surfcoat.2004.03.004
65. A. Fossati, F. Borgioli, E. Galvanetto, T. Bacci: Surface and Coatings Technology, 200(11), 2006, 3511-3517. https://doi.org/10.1016/j.surfcoat.2004.10.122
66. H.R.S. Mahmoud, S.A. Yusoff, A. Zainuddin, P. Hussain, M. Ismail, K. Abidin: MATEC Web of Conferences, 13, 2014, 4021-4025. https://doi.org/10.1051/matecconf/20141304021
67. C.E. Pinedo, A.P. Tschiptschin: International Heat Treatment and Surface Engineering, 5(2), 2011, 73-77. https://doi.org/10.1179/174951411x13051201040703
68. J.F. dos Santos, C.M. Garzón, A.P. Tschiptschin: Materials Science and Engineering: A, 382(1-2), 2004, 378-386. https://doi.org/10.1016/j.msea.2004.05.003
69. A. Feder, J. Alcalá, L. Llanes, M. Anglada: Journal of the European Ceramic Society, 23(15), 2003, 2955-2962. https://doi.org/10.4028/www.scientific.net/amm.529.251
70. P.S. Gajendra, J. Alphonsa, P.K. Barhai, P.A. Rayjada, P.M. Raole, S. Mukherjee: Surface and Coatings Technology, 200(20-21), 2006, 5807- 5811. https://doi.org/10.1016/j.surfcoat.2005.08.149
71. F. Zhang, M. Yan: Journal of Materials Science & Technology, 30(12), 2014, 1278-1283. https://doi.org/10.1016/j.jmst.2013.10.032
72. A.F. Yetim, M. Yazıcı: Journal of Bionic Engineering, 11(4), 2014, 620-629. https://doi.org/10.1016/s1672-6529(14)60073-1
73. B. Hashemi, M. Rezaee Yazdi, V. Azar: Materials & Design, 32(6), 2011, 3287-3292. https://doi.org/10.1016/j.matdes.2011.02.037
74. Y. Li, L. Wang, J.J. Xu, Y.C. Shan: Applied Mechanics and Materials, 268-270, 2012, 269-274. https://doi.org/10.4028/www.scientific.net/amm.268-270.269
75. E.L. Dalibon, D. Heim, Ch. Forsich, S.P. Brühl: Procedia Materials Science, 9, 2015, 163-170. https://doi.org/10.1016/j.mspro.2015.04.021
76. F.C. Nascimento, C.E. Foerster, S.L.R da Silva, C.M. Lepienski, C.J.M. Siqueira, C.A. Junio: Materials Research, 12(8), 2009, 173-180. https://doi.org/10.1590/s1516-14392009000200011

ACTA METALLURGICA SLOVACA
2021, VOL. 27, NO. 2, 53-56

RESEARCH PAPER

PRECIPITATION STATE OF WARM WORKED AA7050 ALLOY: EFFECT ON TOUGHNESS BEHAVIOR

Andrea Di Schino[1]

[1] Engineering Department, University of Perugia, Via G. Duranti 93, 06125, Perugia, Italy

*Correspondence: andrea.dischino@unipg.it, Engineering Department, University of Perugia, Via G. Duranti 93, 06125, Perugia, Italy

Received: 23.03.2021
Accepted: 18.04.2021

ABSTRACT

Usually, strength-toughness combination in aluminum alloys is improved by heat treatment (solid solution followed by quenching and reheating) after a deformation process at high temperature. In some cases, a cold working step is added in the manufacturing process before heat treatment aimed to enhance the alloy strength. In recent time, some trials have been carried out finalized to replace the cold working step with a warm deformation. Such a process route appeared to be quite effective in improving the toughness behavior of 7xxx alloys. Anyway, a metallurgical explanation for such behavior has not still be reported. In this, a comparison of the precipitation state following the two different routes is reported. Results show clear differences in the nanoprecipitation densities in the two cases, claiming for their responsibility in the definition of the toughness behavior.

Keywords: toughness; aluminum alloys; heat treatment; precipitation

INTRODUCTION

Light alloys were considered for a long time the best solution for most the high-tech applications, including sport equipment [1], energy and automotive [2]. Aeronautical industry was considered one mostly requiring such alloys properties. Among lightweight alloys, the aluminum based ones are assuming industrial impact following their specific combination of properties [3]. Following to that, they seem to be the most promising candidates for structural aerospace designers if compared with different alloys [4-6]. Their specific behavior is known to depend on alloying strategies and processes, as reported in a rich literature (e.g. [7-9]). The choice of alloying elements is made based on the their individual and synergic impact on microstructure and hence on mechanical behavior. The above statement is reported in detail in [10]. Savage and colleagues [11] described the effect of Cu addition on the hardening of Al-Mg-Si alloys characterized by a ultra-fine grain. In the large number of aluminum alloys the AA7050 one assumes particular importance, following its specific balance between tensile properties and corrosion resistance [12, 14]. Such quite promising behavior is achieved by proper recrystallization phenomena occurring during and after the hot deformation stage [14-17]. Physically based constitutive equations and their capability to predict the microstructural evolution in such alloy are reported in [18]. A novel approach to recrystallization phenomena in aluminum alloys is proposed in [19], to be applied in the case of complex geometry parts, commonly produced by closed-due forging and solution and quenching heat treatment. Such effect is also reported in detail by Mac Kenzie in [20].
AMS 4333 International Standard calls for an intermediate cold working process step, with a maximum 5% allowed cold upsetting, to be performed before the two ageing final steps, after the solution heat treatment. This with the aim to best define the precipitation state (in terms of precipitation size distribution) so assuring the best achievable mechanical properties combination [21]. Concerning this topic, Wyss et al. proposed the US Patent [22], showing beneficial effect due to an intermediate warm hardening process step, to be executed instead of the standard cold upsetting, on the facture toughness properties. Such process route appeared to be quite promising in the case of 7xxx alloys: in particular an improvement of toughness was found without any deterioration of hardness and tensile behavior [23]. Such route also allowed improving the component homogeneity by means of grain refinement [24]. This was explained in terms of dislocation cross-slip during deformation at the involved temperature range in the considered process. This phenomenon allows a grain re-orientation with a consequent re-organization of sub-grains, moving towards high angle boundaries: the higher the deformation temperature, the easier the process [25]. Such phenomena are reported in literature as Continuous Dynamic Recrystallization (CDR) [26-28]. Other phenomena, such as strain hardening [29, 30] and recovery [31, 32], depend on dislocation evolution in dependence on other present crystallographic imperfections.
In this paper the effect of process routes on the precipitation size distribution is reported.

MATERIAL AND METHODS

The AA 7025 alloy nominal composition is reported in **Table 1**.

Table 1 Chemical analysis of AISI 441 (main elements, mass %).

Elements	Al	Cu	Mg	Zn
Wt, %	balance	2.3	2.2	6.25

Three families 10 cm x 6 cm x 3 cm specimens A, (specimens A1, A2 and A3), B (specimens B1, B2 and B3) and C (speci-

mens C1, C2 and C3) were manufactured from around a hot forged bar, characterized by an initial diameter Φ = 120 mm. The heat treatment satisfied the AMS2770N specification requirements. The process was completed with room temperature up-setting and final two stages aging at 5 h at 394 K + 8 h at 450 K (samples A). The two innovative cycles (samples B and C) just differed from AMS2770N specification requirements in terms of up-setting temperature: as a matter of fact, they were carried out at 423 K and 473 K instead of room temperature. All the other cycle steps were unmodified (**Table 2**).

Table 2 Heat treatment conditions

Specimen	Solution heat treatment	Water Quenching	Deformation temperature (K)	First ageing step	Second ageing step
A	YES	YES	293	YES	YES
B	YES	YES	423	YES	YES
C	YES	YES	473	YES	YES

All specimens underwent a solution heat treatment at T=748 K for 5 h, water quenching, 5% warm deformation, ageing. The process conditions differ on the upsetting temperature, (see Table 2). A1, A2 and A3 samples were deformed at room temperature; samples B1, B2 and B3 at 423 K and samples;C1, C2 and C3 at 473 K. After heat treatment transverse specimens (in agreement with ASTM-E399) were machined and tests KIC toughness were performed (according to the ASTM E399 standard). Specimens machined starting from the three groups (A, B and C) were prepared for metallographic examination. Grain size was measured by light microscopy (LM) according to ASTM E112 specification. Precipitation state analysis was performed with a scanning electronic microscope SEM-FEG (SEM FEG LEO 1550 ZEISS (McQuairie, London, UK) equipped with an EDS OXFORD X ACT system (v2.2, Abington, UK). Precipitates number counting has been performed by means of IMAGE-J Fiji 1.46, a software for the automatic images processing and analyses program. The image analysis was carried out by setting a Feret-diameter threshold of 10 nm. An example of SEM FEG image prepared for precipitation number count by mean of IMAGE-J Fiji 1.46 software is reported in **Figure 1**.

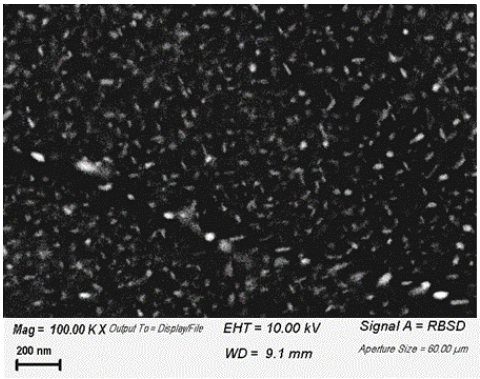

Fig. 1 Example of the SEM-FEG image (specimen A)

RESULTS AND DISCUSSION

The effect of the up-setting temperature increase on microstructure is shown in **Figures 2** and **3**: results clearly show a grain size refinement. Results from mechanical properties related to the considered materials are reported in detail in [33] and are here summarized for the reader (see **Table 3**).

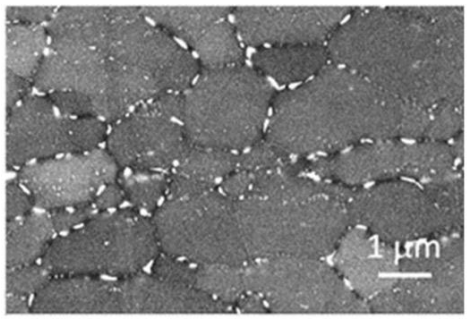

Fig. 2 Sample A microstructure (up-setting T: 293 K)

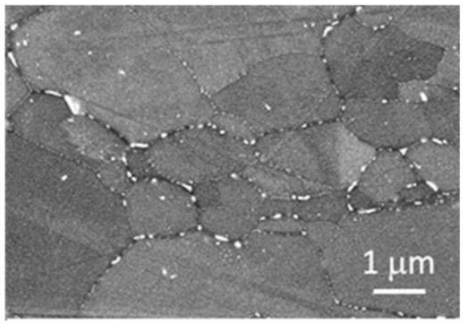

Fig. 3 Sample B microstructure (up-setting T: 423 K)

Table 3 Mechanical properties and grain size evolution with intermediate up-setting temperature

Specimen	Upsetting temperature (K)	HB	YS (MPa)	K_{IC} (MPa $m^{1/2}$)	Grain size (µm)
A	293	145	450	26.8	10.1
B	423	147	455	28.3	8.6
C	473	152	470	30.1	7.5

In particular, results reported in put in evidence a not negligible K_{IC} improvement, even if both Brinell hardness and yield strength were increased. It is worth to be noted that an up-setting increase up to 473 K resulted in a 10% toughness improvement in terms of $K_{IC,}$ with respect to material processed in standard condition. Table 3 also shows that tensile properties were more sensitive to up-setting temperature than hardness: this suggests a significant fine precipitation variation mainly following to Guiner-Preston zones [34, 35] formation acting as a barrier to grain size evolution. The precipitation distribution evolution with up-setting temperature was analyzed by image analysis.

Microstructures of samples A1, B1 and C1 as obtained by SEM-FEG at high magnification are shown in **Figure 4**, **Figure 5** and **Figure 6** respectively.

Such analysis allowed to divide precipitates in the following families:

1. larger precipitates located at grain and sub-grain boundaries (size ranging=100-500 nm);
2. fine precipitates inside grains and sub-grains (size ranging=20-100 nm);
3. very fine precipitates located inside grains sub-grains (size ranging= <20 nm).

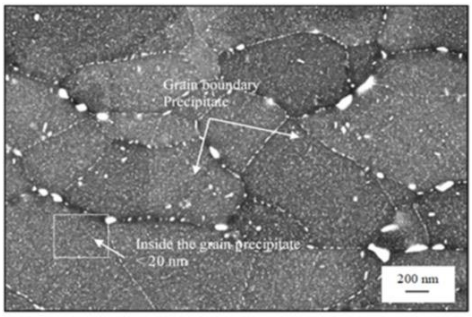

Fig. 4 Sample A microstructure (up-setting T: 293 K)

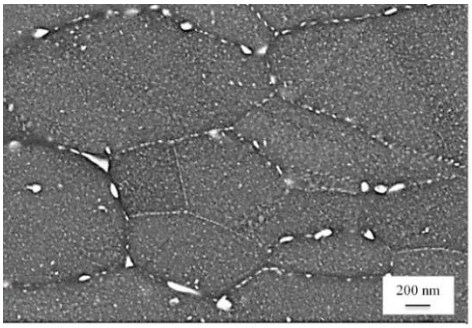

Fig. 5 Sample B microstructure (up-setting T: 423 K)

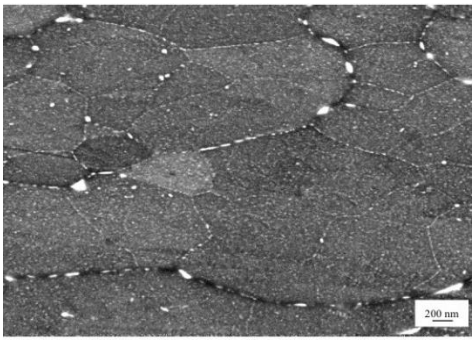

Fig. 6 Sample C microstructure (up-setting T: 473 K)

The dependence of the number of detected precipitates on the upsetting temperature is shown in **Figure 7**.
In this **Figure 7** precipitates are grouped according to their average size, considering the above reported ranges. An increase of the average fine precipitates number with the upsetting deformation temperature is put in evidence in **Figure 7.** On the other hand it is worth to be noted that the largest precipitates number seems to be almost independent on such process parameter [36-38]. The above statement agrees with the detected improved toughness and yield strength behavior.

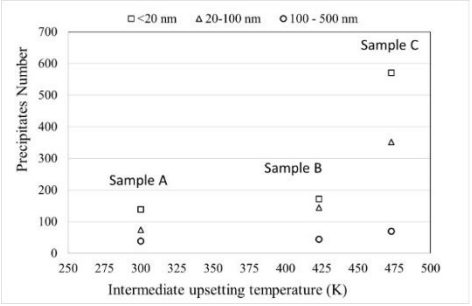

Fig. 7 Mean values of precipitates number grouped in size classes (sample A: intermediate upsetting temperature = 293 K; sample B: intermediate upsetting temperature = 423 K; sample C intermediate upsetting temperature = 473 K)

CONCLUSIONS

Results of analysis related to AA7050 alloy subjected to warm deformation showed that the precipitation state is very sensitive to intermediate deformation step included in the heat treatment cycle. It is reported that a more evident fine precipitation was found after deformation at 473 K. Such precipitation is claimed to be responsible of a grain refinement effect, hence of toughness K_{IC} improvement with respect to materials manufactured according to standard route.

REFERENCES

1. G. Napoli, A Di Schino, M. Paura, T. Vela: Metalurgija, 57, 2018, 111-113.
2. D.K. Sharma, M. Filipponi, A. Di Schino, F. Rossi, J. Castaldi: Metalurgija, 58, 2019, 347-351.
3. A.S. Warren: Developments and Challenges for Aluminum – A Boeing Perspective, *Materials Forum*, Eds. J.F. Nie, A.J. Morton, B.C. Muddle, Institute of Materials Engineering Australasia, 28, 2004, 24-31.
4. C. Gashen: Metals, 11, 2021, 114. https://doi.org/10.3390/met11010114.
5. *Aerospace Structural Materials Handbook*; DoD,Wright-Patterson Air K.F. Force Base: Dayton, OH, USA, 2001.
6. American society of materials, ASM handbook, Volume 2, Properties and selection: Nonferrous Alloys and special purpose materials, 2005.
7. O.S. Fayomi, .P. Popoola, N. Udoye: in *Aluminium Alloys - Recent Trends in Processing, Characterization, Mechanical Behavior and Applications*, Intech open: Rijeka, 2017. https://doi.org/10.5772/intechopen.71399.
8. R.S. Ranam R. Purohit, S. Das: International Journal of Scientific and Research 2, 2012, 1-7.
9. D. Manfredi, R. Bidulsky: Acta Metallurgica Slovaca, 23, 2017, 276-282. https://doi.org/10.12776/ams.v23i3.988.
10. L.F. Mondolfo: *Aluminum Alloys: Structure and Properties*, Butterworth: London, UK, 1976, p. 497-499.
11. X. Sauvage, S. Lee, K. Matsuda, M. Horita: Journal of Alloys and Compounds, 710, 2017, 199-202, https://10.1016/j.jallcom.2017.03.250.
12. J.M. Sanchez, E. Rubio, M. Alvarez, M.A. Sebastian, M. Marcos, J. Mater. Proc. Technol. 164, 2005, 911-918. https://doi.org/10.1016/j.jmatprotec.2005.02.058.

13. P. Rambabu, N.E., Prasad, V.V. Kutumbarao, R.J. Wanhill: Aluminium Alloys for Aerospace Applications. In *Aerospace Materials and Material Technologies*; Springer: Singapore, 2017; 1, 9-52.
14. A. Di Schino: Metals, 10, 2020, 327. https://doi.org/10.3390/met10030327.
15. Y.H. Zhao, Z.X. Liao, Z. Hin, R.Z. Valiev: Acta Materialia, 52, 2004, 52, 4589-4599. https://doi.org/10.1016/j.actamat.2004.06.017.
16. K.F. Adam, Z. Long, D.P. Field: Metallurgical and Materials Transactions A 48, 2017, 2062-2076. http://dx.doi.org/10.1007/s11661-017-3967-3.
17. C.G. Parker, D.P. Field: Observation of Structure Evolution during Annealing of 7xxx Series Al Deformed at High Temperature. In *Light Metals 2012*, Springer: Cham, Switzerland, 2012, 383-386.
18. S. Wang, J. Luo, L. Hou, J. Zhang, L. Zhuang: Materials and Design 107, 2016, 107, 277-289. https://doi.org/10.1016/j.matdes.2016.06.023.
19. A. Di Schino, P.E. Di Nunzio: Acta Metall. Slovaca, 23, 2017, 62-71, https://doi.org/10.12776/ams.v23i1.852.
20. D. MacKenzie, D. Scott: Heat Treating Progress, 5, 2005, 37-43.
21. AMS 4333 International Standard: *Aluminum Alloy, Die Forgings, 6.2Zn - 2.3Cu - 2.2Mg - 0.12Zr (7050-T7452), Solution Heat Treated, Compression Stress-Relieved, and Overaged*. 2015.
22. R. Wyss, R. Alcoa: *Method for increasing the strength of aluminum alloy products through warm working*, United States Patent: US5194102A, 1993, 16, 03.
23. A. Di Schino, L. Alleva, M. Guagnelli: Mater. Sci. Forum, 715-716, 2012, 860-865. https://doi.org/10.4028/www.scientific.net/MSF.715-716.860.
24. A. Di Schino: Metalurgija, 56, 2017, 349-352.
25. S. Gourdet, F. Montheillet: Acta Materialia, 50, 2002, 2801-2812. https://doi.org/10.1016/S1359-6454(02)00098-8.
26. A. Di Schino, P. Di Nunzio, G.L. Turconi: Mater. Sci. Forum, 558-559, 2007, 1435-1441. https://doi.org/10.4028/0-87849-443-x.1435.
27. F.J. Humphreys, M. Hatherly: *Recrystallization and related annealing phenomena*, 2nd ed., Elsevier, Amsterdam, 2004.
28. S. Mancini, L. Langellotto, P. Di Nunzio, C. Zitelli, A. Di Schino: Metals, 10, 2020, 186. https://doi.org/1010.3390/met10020186.
29. P.J. Jackson: Mater. Sci. Eng., 57(1), 1983, 39-47. https://doi.org/10.1016/0025-5416(83)90025-3.
30. G Saada: Mater. Sci. Eng. A, 137, 1991, 177-183. https://doi.org/10.1016/0921-5093(91)90333-I.
31. J.P. Poirier: Rev. Phys. Appl., 11, 1976, 11, 731-739.
32. A.M. Hussein, S.I. Rao, M.D. Uchic, D.M. Dimiduk, J.A. El-Awady: Acta Mater., 85, 2015, 180-190. https://doi.org/10.1016/j.actamat.2014.10.067.
33. A. Di Schino, C. Testani: Metals, 10, 2020 552. https: //doi.org/10.3390/met10040552.
34. C.V. Singh, D.H. Warner: Acta Materialia, 58, 2010, 5797. https: //doi.org/10.1016/j.actamat.2010.06.055.
35. M. van Rooyen, J.A. Sinte Maartensdijk, E. Mittemejer: Metallurgical Transactions A, 19, 1988, 2433-2443. https://doi.org/10.1007/bf02645471.
36. J. Bidulska, R. Bidulsky, M.A. Grande, T. Kvackaj: Materials, 12(22), 2019, 3724. https://doi.org/10.3390/ma12223724.
37. J. Bidulska, R. Bidulsky, T. Kvackaj, M.A. Grande: High Temperature Materials and Processes, 27(3), 2008, 203-207. https://doi.org/10.1515/HTMP.2008.27.3.203.
38. T. Kvackaj, et al.: Materials Science Forum, 633-634, 2010, 273-302. https://doi.org/10.4028/www.scientific.net/MSF.633-634.273.

ACTA METALLURGICA SLOVACA
2021, VOL. 27, NO. 2, 57-62

RESEARCH PAPER

CHARACTERIZATION OF CHROMIUM NITRIDE PRECIPITATION IN THE HEAT AFFECTED ZONE OF THE SUPERDUPLEX STAINLESS STEEL UNS S32750: AN EXPERIMENTAL AND NUMERICAL ANALYSIS

Paolo Ferro[1], *Alberto Fabrizi*[1], *Jan-Olof Nilsson*[2], *Franco Bonollo*[1]

[1]Department of Engineering and Management, University of Padova, Stradella San Nicola 3, 36100 Vicenza, Italy
[2]JON Materials Consulting, Sjögatan 2, 651 71, Arvika, Sweden

*Corresponding author: paolo.ferro@unipd.it tel.: +39 0444 998769 Department of Engineering and Management, University of Padova, Stradella San Nicola 3, 36100 Vicenza, Italy

Received: 16.03.2021
Accepted: 29.04.2021

ABSTRACT

It is well known that pitting corrosion resistance of duplex and superduplex stainless steels strongly depends on microstructural characteristics such as ferrite/austenite proportion, presence of intermetallic phases and elemental partitioning between the austenite and ferrite phases. In particular, during the welding operation, very fine chromium nitrides may precipitate within ferrite grains of the heat affected zone drastically reducing the corrosion resistance of welded joints of duplex and super duplex stainless steels. However, due to their small size and low distribution, analyzing the chemical composition and crystallography of chromium nitrides is quite difficult and only a restricted number of advanced techniques of investigation may discriminate their signal from the surrounding matrix. This work is aimed at supporting the microstructural characterization of a welded joint of a superduplex stainless steel by means of a field-emission gun scanning electron microscope. Sub-micron chromium nitride precipitates, identified within the ferritic grains of the heat affected zone, are recognized to be the main reason for the reduced pitting corrosion resistance of the analyzed welded joints. The results are supported by a multi-pass welding process numerical simulation aimed at estimating the cooling rates promoting chromium nitride precipitation in the heat affected zone. The model is proven to work well and be a useful design instrument for assessing optimal welding process parameters.

Keywords: Super duplex stainless steels, Chromium nitride, microstructure, thermal model, multi-pass welding; numerical simulation

INTRODUCTION

Duplex (DSS) and superduplex (SDSS) stainless steels are increasingly used in aggressive environments thanks to their outstanding combination of mechanical strength, corrosion resistance in various types of environments and weldability. For ensuring such excellent combination of properties, it is essential to maintain a ferrite-austenite ratio close to 50:50 and avoid the precipitation of undesired phases such as secondary austenite (γ_2), chromium nitrides, carbides, sigma (σ) and chi (χ) phases [1-12].

Unfortunately, the thermal cycles induced by welding operations alter the optimized microstructure of the parent metal. The fusion zone (FZ) and the heat-affected zone (HAZ) are generally characterized by an unbalanced ratio between ferrite and austenite because of the high temperatures reached and the high cooling rates characterizing the welding process. Since the peak temperature in the HAZ is much higher than the upper limit of phase balance between δ-ferrite and austenite, most of the γ islands in the prior duplex structure dissolve into the δ-ferrite matrix during the heating period. During cooling, in the temperature range between 1300 and 800 °C, austenite starts to re-precipitate, both in the FZ and HAZ, mainly at the ferrite grain boundaries due to higher free energy of these locations. Because of the high cooling rate of the weld metal, the ferrite–austenite transformation is inhibited, and less austenite will be formed compared with the parent material (PM). Even if very low heat input may prevent the precipitation of brittle intermetallic phases such as σ or χ, it may lead to high ferrite contents and intense nitride precipitation [13-15]. A proper filler metal, the chemical composition of which is rich in Ni, may partially restore the balance between primary austenite and δ ferrite, but unfortunately it does not solve the problem of chromium nitrides precipitation in HAZ.

In fact, it is widely reported that chromium nitride precipitation can occur within ferrite grains in different duplex grades during the welding process due to the rapid cooling rate [16-22]. Indeed, austenite grains transform to ferrite in the high temperature heat affected zone (HAZ) and the high cooling rates partially inhibit austenite re-transformation resulting in a nitrogen supersaturated ferrite which is enriched in Cr. Consequently, chromium nitride particles precipitate in ferrite grains, mainly intragranulary (**Fig. 1**), but also along the ferrite/austenite interfaces and ferrite subgrain boundaries.

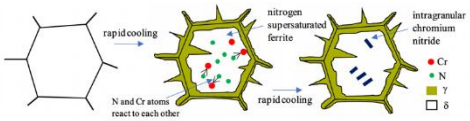

Fig. 1 Schematic of chromium nitride precipitation in HAZ

In multi-pass welding a cooperative precipitation mechanism of Cr-N and secondary austenite (γ_2) could take place [23], as well. As a matter of fact, a chromium-rich and nitrogen-poor zone forms around chromium nitride, which promotes γ_2 nucleation.
Chromium nitrides are found to drastically reduce the mechanical and corrosion properties of DSS and SDSS [24, 25] and this is the main reason why the welding engineer should know the chromium nitrides mechanism formation, the techiques available to detect them, and take care in selecting process parameters in order to prevent their existence. However, due to their small size and low distribution, the chemical and crystallographic analysis of chromium nitrides is quite difficult and only a limited number of advanced techniques may discriminate their signal from that of the surrounding matrix. In the aforementioned works, the chemical analysis of Cr-N is generally omitted or deduced. For instance, Zhang et al. [26] pointed out that after electrically etching in oxalic acid solution, some pits were observed, indicating the appearance of chromium nitride.
Only in few investigations of DSS and SDSS, transmission electron microscopy (TEM) coupled with electron diffraction were carried out to clearly identify the composition and crystallography of chromium nitrides precipitated during thermal treatments simulating welding processes [16, 22, 27].
Anyway, in practical experience, the precipitation of chromium nitrides in welded DSS and SDSS occurs in some ferrite grains confined to the thin HAZ layer resulting in a cumbersome TEM sample preparation using standard procedures.
Using Field Emission Gun-Scanning Electron Microscopy (FEG-SEM) with a significantly smaller beam and an increased current density compared to traditional SEMs, higher resolution micrographs can be collected, and consequently beneficial results are achieved also in chemical microanalysis by an Energy Dispersive Spectroscometer (EDS) attached to the microscope.
In the present work, in FEG-SEM the EDS-linescan technique was used to determine the elemental composition of submicron precipitates in the HAZ of a welded UNS S32750 SDSS and a Cr-N particle has been identified. This work is aimed both at supporting the microstructural investigation carried out in a previous work on the same SDSS welded joints [7] and to develop a numerical model of the multi-pass welding process useful to predict the conditions under which chromium nitrides precipitate. The numerical model should result in a design tool useful to the welding engineer to predict the conditions promoting Cr-N precipitation as well as the optimal process parameters to avoid them.

MATERIAL AND METHODS

Material, geometry and welding process parameters

Butt-welded joints made of SDSS thick plates (15 mm), type UNS S32750 previously solution treated at 1070 °C and then quenched, were produced by submerged-arc welding (SAW) using the groove shown in **Fig. 2** and process parameters collected in **table 1**. The heat input is obtained by using the following formula:

$$HI\,[kJ/mm] = \eta \frac{V[V] \cdot I[A]}{v[mm/s] \cdot 1000} \qquad (1.)$$

where V is the voltage, I is the amperage, v is the travel speed and ν is the thermal efficiency that for SAW is approximately equal to 0.95 [28].

In **table 2**, the nominal chemical compositions of both parent and filler metal are summarized. It can be noted that the filler metal is enriched in nickel compared to the base material in order to contrast the high cooling rate and promote the correct balanced austenite/ferrite ratio in the FZ.

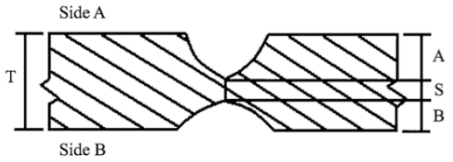

Fig. 1 Geometry of the adopted groove (T = 15 mm, A = 4 mm, S = 5 mm, B = 6 mm); figure not to scale

Metallographic examinations

For microstructure characterization, metallographic sections transverse to the weld bead were initially ground and polished using standard metallographic preparation techniques and then chemically etched with a 40%HNO3 aqueous solution that does not attack Cr-N precipitates, as reported in Ref. [16]. The resulting microstructures were evaluated using Optical Microscopy (OM) and Field Emission Gun Scanning Electron Microscopy (FEG-SEM, Quanta 250 from Fei©) equipped with Energy Dispersive Spectroscopy (EDS, Edax©). For elemental composition of a precipitate, EDS linescan microanalysis was carried out using a probe size of about ~ 50 nm and inter-spot distance of ~ 3 nm for a dwell time of 1800 ms.

Material, geometry and welding process parameters

A thermal numerical model was developed using Sysweld® numerical code with the aim at estimating the thermal fields and cooling rates that promote precipitation of chromium nitrides. In particular, the transient analysis of welding heat transfer was simulated following the experimental welding process parameters in a finite element (FE) model with a moving heat source. The temperature history at each node is obtained by solving the heat flow balance equation:

$$-\left[\frac{\partial R_x}{\partial x} + \frac{\partial R_y}{\partial y} + \frac{\partial R_z}{\partial z}\right] + q(x,y,z,t) = \rho c \frac{\partial T(x,y,z,t)}{\partial t} \qquad (2.)$$

where the rate of heat flow per unit area is denoted by Rx, Ry and Rz; the current temperature is T(x,y,z,t), the rate of internal heat generation is q(x,y,z,t), c is the specific heat, ρ is the density, and t is the time. Eq. (2) can be revised by bringing Fourier 's heat flow as

$$\begin{cases} R_x = -k_x \dfrac{\partial T}{\partial x} \\ R_x = -k_y \dfrac{\partial T}{\partial y} \\ R_x = -k_z \dfrac{\partial T}{\partial z} \end{cases} \qquad (3.)$$

where k_x, k_y and k_y are the alloy thermal conductivity in the three directions x, y and z, respectively.
Due to temperature-dependent material properties (k and c), the associated material behavior was considered to be nonlinear. Now, by substituting Eqs. (3) into Eq. (2), the differential governing heat conduction equation can be rewritten as:

$$\rho c\frac{\partial T}{\partial t}=\frac{\partial}{\partial x}\left[k_x\frac{\partial T}{\partial x}\right]+\frac{\partial}{\partial y}\left[k_y\frac{\partial T}{\partial y}\right]+\frac{\partial}{\partial z}\left[k_z\frac{\partial T}{\partial z}\right]+q \quad (4.)$$

The solution of Eq. (4) requires the definition of initial conditions:

$$T(x,y,z,0)=T_0(x,y,z) \quad (5.)$$

as well as boundaries conditions:

$$\left[k_x\frac{\partial T}{\partial x}N_x+k_y\frac{\partial T}{\partial y}N_y+k_z\frac{\partial T}{\partial z}N_z\right]+q_s+h_c(T-T_a)+h_r(T-T_r)=0 \quad (6.)$$

In Eq. (5), $T_0(x,y,z)$ is taken equal to the ambient temperature (T_a = 20 °C) or eventually the pre-heating temperature. In Eq. (6) N_x, N_y and N_z are the direction cosine of the outward projected normal to the boundary; h_c (25 W/m^{2}K [29]) and h_r are the heat transfer coefficients of convection and radiation, respectively; T is the surface temperature of the model and T_r is the temperature of the heat source instigating radiation. The boundary heat flux is designated by q_s. The heat transfer coefficient of radiation can be written as:

$$h_r=\sigma\varepsilon F(T^2-T_r^2)(T+T_r) \quad (7.)$$

where σ is the Stefan Boltzmann's constant, ε is the emissivity (0.7) and F is the configuration factor.

For the sake of simplicity and with the aim at speeding up the analysis in view of its use in welding design, a 2D model was carried out considering only the transverse section of the bead, as shown in **Figs. 3** and **4**, and exploiting the symmetry conditions. In order to simulate the effects of multi-pass welding, the whole mesh was divided into four groups. In **Fig. 2**, B1, B2, B3 are the groups of elements modelling the three fusion zones, while the remaining elements belong to the parent material (PM). An elements activation/deactivation function was used to simulate the effect of deposition of filler metal during welding. For instance, during the first pass, only the elements belonging to the parent material and group B1 were activated.

Table 1 Welding process parameters

Weld layer /run	Side	Filler metal		Current			Volt range [V]		Travel speed range [cm/min]		Average heat input
		Class	Diameter [mm]	Type polarity	Ampere range [A]						
1	A	25 9 4 NL	2.4	DC-EP	340	360	29	31	54	56	1.09
2	A	25 9 4 NL	2.4	DC-EP	390	410	32	34	46	48	1.60
3	B	25 9 4 NL	2.4	DC-EP	540	560	39	40	38	38	3.35

Table 2 Nominal chemical compositions (wt%) of parent and filler metal

	C	Cr	Cu	Mn	Mo	N	Ni	Si	P	Co	V	Ti	Nb	W	S
Parent metal	0.018	24.8	0.32	0.79	3.85	0.27	6.92	0.22	0.025	-	-	--		-	0.001
Filler metal	0.014	25.12	0.096	0.45	4.04	0.228	9.6	0.39	0.014	0.085	0.047	0.005	0.01	0.01	0.0005

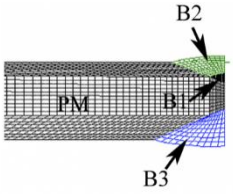

Fig. 3 Mesh of the numerical model (2427 linear finite elements) defining the groups of elements

Thermal material properties are taken as a function of temperature from Sysweld database. The heat source was modelled using a double ellipsoid power density distribution function developed by Goldak et al. [30] (Eq. 8) that is commonly used in literature to model the arc heat source [31].

$$q_g(x,y,t)=\frac{6\sqrt{3}f_{1,2}Q}{\pi\sqrt{\pi}abc_{1,2}}e^{-\frac{3x^2}{a^2}}e^{-\frac{3y^2}{b^2}}e^{-\frac{3[v(t-\tau)]^2}{c_{1,2}^2}} \quad (8.)$$

The meaning of the symbols in Eq. (8) and their values are summarized in **Tables 3** and **4**.

In 2D cross section models, the heat source is thought to move over the analyzed section with a speed equal to that used in experiments as schematized in **Fig. 4**.

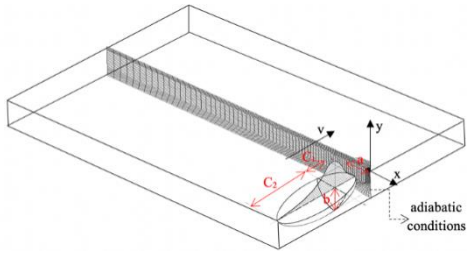

Fig. 4 Schematic of the 2D model and geometrical parameters of the heat source

More in detail, for welding pass number 2 and 3, a superposition of two Goldak's heat sources were used in order to better reproduce the weld pool shapes induced of these last two welding runs. **Table 4** specifies the different geometrical parameters of the overlapped heat sources used in runs 2 and 3.

Table 3 Goldak's source parameters (Fig. 4). *indicates that the value used depends on the run (see Table 4).

Q*	Power Input (V·I) [W]	*
η	Efficiency	0.95
Q	Absorbed power [W], with Q=ηQ*	-
a	Molten pool dimensions [mm]	*
b		*
c_1		*
c_2		*
f_1	Constants for the energy distribution of the heat flux	0.6
f_2		1.4
v	Welding speed [mm s^{-1}]	*
τ	Total duration of time before the welding source has traversed the transverse cross section of the plate [s]	*

Table 4 Geometrical heat source parameters given as a function of the welding pass. Second and third pass were simulated using a superposition of two Goldak's heat sources

Welding pass	a [mm]	b [mm]	c_1 [mm]	c_2 [mm]	τ [s]
1	6	6.5	5.3	10.9	32.7
2(1)	25	0.7	7	15	138.3
2(2)	2.7	2	3.5	7	
3(1)	25	0.7	7	15	647.36
3(3)	3	2	3.5	7	

RESULTS AND DISCUSSION

Microstructure

The HAZ microstructure observed by optical microscope is shown in Fig. 5. Colonies of precipitates were detected within ferrite grains. As shown in Fig. 6, the secondary electron SEM micrograph clearly reveals intragranular precipitates after chemical etching.

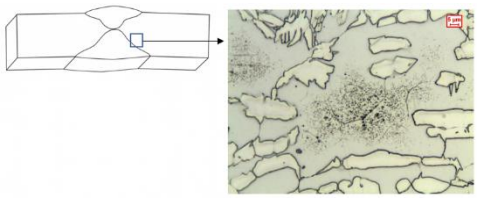

Fig. 5 OM micrograph of HAZ in weld SDSS sample

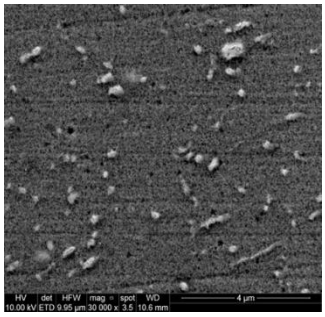

Fig. 6 Secondary electron SEM micrograph of a colony of precipitates within ferrite grain.

Figs. 7a and **7b** show the EDS-linescan image and elemental distribution profiles across the precipitate and the surrounding ferrite grain, respectively. The concentrations of N and Cr are higher within the precipitate as compared to the ferrite matrix while a Fe reduction is observed; in addition, no variations of the C content was observed along the profile excluding carbide particle precipitation. Therefore, neglecting the signal contribution of surrounding α-Fe matrix to the distribution profile, it can be concluded that the precipitate is consistent with a chromium nitride particle.

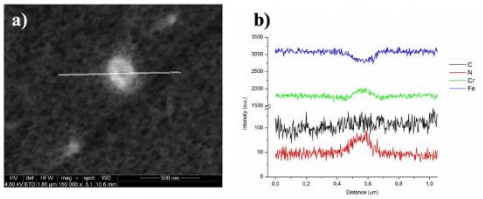

Fig. 7 a) EDS-linescan image and b) corresponding elemental profiles

Fig. 8a shows the morphology of nanometer-sized chromium nitrides at high magnification. As a comparison, in Figs. 8b and 8d TEM micrographs taken from the work of Pettersson et al. [32] and Nilsson [18], respectively, are reported. In particular, in Pettersson's work chromium nitrides were found to precipitate in a UNS S32750 SDSS cooled from 1225 °C with a cooling rate of 100K/s while Nilsson for the first time identified the rod-shaped precipitates as Cr-N using ED in TEM.
Finally, **Fig. 8c** shows another detail of chromium nitride distribution found in the present alloy. They are observed both inside the ferrite grains and in ferrite sub-grain boundaries.

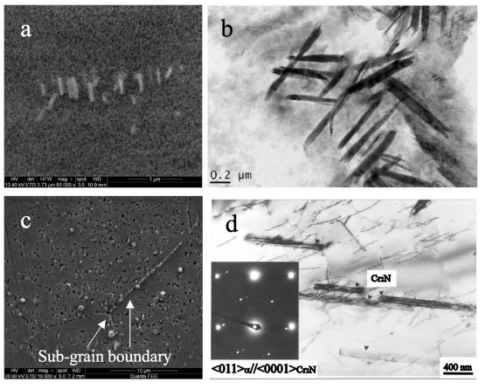

Fig. 8 a) The morphology (a) (b) (d) and distribution (c) of chromium nitrides. Pictures (b) and (d) are TEM micrographs published in ref. [32] and [18], respectively

Finally, the volume fractions of ferrite in FZ, HAZ and PM are summarized in **Fig. 9a**. It was observed that the HAZ shows the highest amount of δ ferrite (59%). This is because of the high cooling rates and the slow diffusion of Ni in the Ni-rich filler metal. Despite the relatively fast diffusion of nitrogen, the cooling rate is so high that nitrogen is unable to escape from the ferrite leading to supersaturation and subsequent Cr-N precipitation, as schematized in **Fig. 1**.

Fig. 9 Microstructure and ferrite proportion in different zones of the weld (a) and micrograph of the HAZ (b)

Numerical results

Fig. 10 shows the shape and dimension of the fusion zone (red colour) obtained by welding simulation. The use of a double heat source function was found successful in capturing the correct FZ shape of beads 2 and 3. The thermal model was used to both characterize the austenite proportion in FZ and estimate the cooling rate promoting precipitation of chromium nitrides in HAZ. In fact, during cooling, in the temperature range 1200 – 800 °C, δ-ferrite partially transforms to primary austenite. The corresponding volume fraction formed at time t (V_γ) will depend on the cooling rate according to the relation proposed by Lindblom and Hannerz [33]:

$$V_g = (Dt_{12-8})^m \quad (9.)$$

where Δt_{12-8} is the time interval elapsed during cooling from 1200 to 800 °C while m is a parameter that depends on the alloy composition. Using numerical simulation and the measured austenite volume fraction in FZ induced by the last welding pass (V_γ = 0.47, **Fig. 9**) it was obtained Δt_{12-8} = 24 s and therefore, from

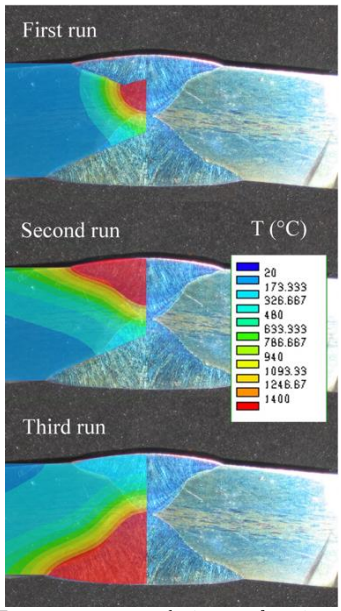

Fig. 10 Temperature maps at the instant of maximum FZ size (red color) as a function of welding pass and comparison with weld bead macrograph.

Eq. (9), m = -0.237. In **Fig. 11**, both the temperature evolution and its derivative at a node belonging to the HAZ of the third weld bead are plotted. During cooling, in the temperature interval between 1280 and 900 °C, the cooling rate ranges from -50 °C/s to -20 °C/s, that is in perfect agreement with the cooling rates promoting Cr-N precipitation in the same SDSS (-20÷-100 °C/s) found by Pettersson et al. [32].

The 2D proposed model is therefore proven to be a useful design tool instrument able to capture the conditions under which chromium nitrides may forms. Because of its rapid solution, it can be used to predict the optimal process parameters assuring the lowest risk of secondary phases precipitation.

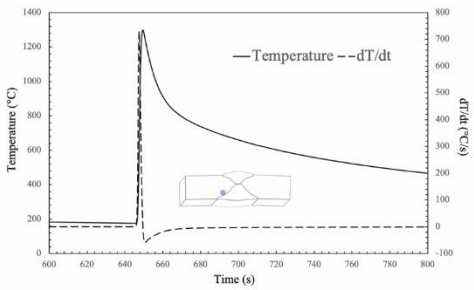

Fig. 9 Temperature and its derivative evolution in HAZ of the third weld bead

CONCLUSIONS

Rapid cooling prevents the formation of intermetallic phases but if the cooling is not properly controlled, there is a risk of forming chromium nitrides in nitrogen-rich DSS and SDSS. Chromium nitrides can promote pitting corrosion and must therefore be avoided. Unfortunately, they are not easily detectable with standard metallographic techniques, because of their sub-micron dimensions. On the other hand, investigations using advanced instruments such as the transmission electron microscope, are time-consuming and, consequently, of limited practical use for industrial application. A methodology aimed at detecting Cr-N in the HAZ of a SDSS using the field-emission gun scanning electron microscope is suggested and presented here. It was found to be more efficient and practical compared to TEM investigations. Finally, a thermal numerical model of the multi-pass welding process was also developed that allows welding engineer to estimate the cooling rates promoting Cr-N precipitation in the HAZ. The results were found to be in excellent agreement with those found in the literature.

REFERENCES

1. S.S.M. Tavares, J.M. Pardal, L.D. Lima, I.N. Bastos, A.M. Nascimento, J.A. de Souza: Materials Characterization, 58, 2007, 610–616.
https://doi.org/10.1016/j.matchar.2006.07.006.
2. P. Ferro, J.-O. Nilsson, F. Bonollo: Acta Metallurgica Slovaca, 24(2), 2018, 147-155.
https://doi.org/10.12776/ams.v24i2.1073.
3. R.A. Perren, T. Suter, C. Solenthaler, G. Gullo, P.J. Uggowitzer, H. Bohni, M.O. Speidel: Corrosion Science, 43, 2001, 727-745.
https://doi.org/10.1016/S0010-938X(00)00088-3.

4. B. Deng, Z. Wang, Y. Jiang, T. Sun, J. Xu, J. Li: Corrosion Science, 51, 2009, 2969–2975. https://doi.org/10.1016/j.corsci.2009.08.015.
5. Y.-L. He, N.-Q. Zhu, X.-G. Lu, L. Li: Materials Science and Engineering A, 528, 2010, 721–729. https://doi.org/10.1016/j.msea.2010.09.067.
6. N. Sathirachinda, R. Pettersson, S. Wessman, J. Pan: Corrosion Science, 52, 2010, 179–186. https://doi.org/10.1016/j.corsci.2009.08.057.
7. R. Cervo, P. Ferro, A Tiziani: Journal of Materials Science, 45, 2010, 4369-4377. https://doi.org/10.1007/s10853-010-4310-1.
8. R. Cervo, P. Ferro, A Tiziani, F. Zucchi: Journal of Materials Science, 45, 2010, 4378-4389. https://doi.org/10.1007/s10853-010-4311-0.
9. P. Ferro, F. Bonollo: Metallurgical and Materials Transactions A, 43, 2012 1109-1116. https://doi.org/10.1007/s11661-011-0966-7.
10. P. Ferro: Acta Materialia, 61, 2013, 3141-3147. https://doi.org/10.1016/j.actamat.2013.01.034.
11. P. Ferro, A. Fabrizi, F. Bonollo: Acta Metallurgica Sinica, 29(9), 2016, 859-868. https://doi.org/10.1007/s40195-016-0462-6.
12. P. Ferro, A. Fabrizi, J.-O. Nilsson: Research and Reports on Metals, 1(2), 2017, 1-6.
13. K. Migiakis, G.D. Papadimitriou: Journal of Materials Science, 44, 2009, 6372-6383. https://doi.org/10.1007/s10853-009-3878-9.
14. T. Ogawa, T. Koseki: Welding Journal, 68(5), 1989, 181s-191s.
15. F. Bonollo, A. Gregori, A. Tiziani, J.-O. Nilsson: A study on microstructural evolution of superduplex steels (SAF 2507) induced by isothermal heat treatment. *Proceedings of 11th congress of the international federation for heat treatment and surface engineering*, Associazione Italiana di Metallurgia, Milano, 3, 1998, 291–300.
16. A. J. Ramirez, S. D. Brandi and J. C. Lippold: Science and Technology of Welding and Joining, 9, 2004, 301-313. https://doi.org/10.1179/136217104225021715.
17. A. Gregori, J.-O. Nilsson: Metallurgical and Materials Transactions A, 33, 2002, 1009-1018. https://doi.org/10.1007/s11661-002-0202-6.
18. J.-O. Nilsson: Materials Science and Technology, 8, 1992, 685-700. https://doi.org/10.1179/mst.1992.8.8.685.
19. S.S.M. Tavares, C. Scandian, J.M. Pardal, T.S. Luz, F.J. da Silva: Engineering Failure Analysis, 17, 2010, 1500–1506. https://doi.org/10.1016/j.engfailanal.2010.05.012.
20. C.M. Garzon, A.J. Ramirez: Acta Materialia, 54, 2006, 3321–3331. https://doi.org/10.1016/j.actamat.2006.03.018.
21. D. Bruch, D. Henes, P. Leibenguth, Ch. Holzapfel: La Metallurgia Italiana, 6, 2008, 7-13.
22. A.J. Ramirez, J.C. Lippold, S.D. Brandi: Metallurgical and Materials Transactions A, 34, 2003, 1575-1597. https://doi.org/10.1007/s11661-003-0304-9.
23. Z. Zhang, H. Jing, L. Xu, Y. Han, L. Zhao, J. Zhang: Applied Surface Science, 394, 2017, 297–314. https://doi.org/10.1016/j.apsusc.2016.10.047.
24. H. Tan, Z. Wang, Y. Jiang, Y. Yang, B. Deng, H. Song, J. Li: Corrosion Science, 55, 2012, 368–377. https://doi.org/10.1016/j.corsci.2011.10.039.
25. Y. Shi, S. Cui, T. Zhu, S. Gu, X. Shen: Journal of Materials Processing Technology, 256, 2018, 254–261. https://doi.org/10.1016/j.jmatprotec.2018.02.019.
26. Z. Zhang, Z. Wang, Y. Jiang, H. Tan, D. Han, Y. Guo, J. Li: Corrosion Science, 62, 2012, 42–50. https://doi.org/10.1016/j.corsci.2012.04.047.
27. T.H. Chen, J.R. Yang: Materials Science and Engineering A, 338, 2002, 166-181. https://doi.org/10.1016/S0921-5093(02)00065-5.
28. Ø. Grong: *Metallurgical modelling of welding*. The Institute of Materials, London, Great Britain, 1997.
29. R. Goyal, E. Johnson, M. El-Zein, J. Goldak, M. Coulombe, S. Tchernov: A Model Equation for the Convection Coefficient for Thermal Analysis of Welded Structures. In *Proceedings of the Trends in Welding Research*, Proceedings of the 8th International Conference; Eds. S.A. David, T. DebRoy, J.N. DuPont, T. Koseki, ASM Intl., Ohio, United States; 2008, 321–327.
30. J. Goldak, A. Chakravarti, M. Birbby: Metallurgical and Materials Transactions B, 15, 1984, 299–305. https://doi.org/10.1007/BF02667333.
31. P. Ferro, F. Bonollo, A. Tiziani: International Journal of Computational Materials Science and Surface Engineering, 3, 2010, 114-132. https://doi.org/10.1504/IJCMSSE.2010.033148.
32. N. Pettersson, R.F.A. Pettersson, S. Wessman: Metallurgical and Materials Transactions A, 46, 2015, 1062-1072. https://doi.org/10.1007/s11661-014-2718-y.
33. J. C. Lippold, D. J. Kotecki: *Welding Metallurgy and Weldability of Stainless Steels*, Wiley-VCH, Hoboken, New Jersey, 2005.

ACTA METALLURGICA SLOVACA
2021, VOL. 27, NO. 2, 63-67

RESEARCH PAPER

EXPERIMENTAL ANALYSIS OF DAMPING PROPERTIES OF VISCOELASTIC MATERIALS

Lucjan Witek[1], Piotr Łabuński[2]

[1] Rzeszow University of Technology, Faculty of Mechanical Engineering and Aeronautics, Department of Aircraft and Aero Engines, Rzeszow, Poland.
[2] Doctoral School of Engineering and Technical Sciences, Rzeszów University of Technology, Rzeszow, Poland.

** lwitek@prz.edu.pl, d506@stud.prz.edu.pl, Tel. +48 178651324, Powstancow Warszawy Ave. 8, 35-959 Rzeszow, Poland.*

Received: 13.03.2021
Accepted: 13.05.2021

ABSTRACT

This study presents results of an experimental investigations of the materials used in passive damping vibrations. The main purpose of this paper was to examine the damping properties of selected viscoelastic materials (VEM), using the modal analysis. In presented analysis three configurations of specimens were considered. At first, the separated steel beam was analyzed. As results of this analysis, the frequencies and amplitudes of the beam during resonance were obtained. In next part of the work the modified specimen was investigated. In this modification the bitumen-based material (as a damper) was fixed to the surface of the beam. This method is known as free layer damping (FLD) treatment. In last configuration, the butyl rubber layer was connected to the steel beam. Using the Unholtz-Dickie UDCO-TA250 electrodynamic vibration system, the natural frequencies and amplitudes of free vibrations for all examined specimens were obtained. The vibration amplitude of the beam was measured using piezoelectric acceleration sensors. In order to define the damping capabilities of both the bitumen based material and the butyl rubber, the relative amplitude of specimens and the loss factor using half-power bandwidth method were calculated.

Keywords: passive vibration damping, experimental modal analysis, viscoelastic material, free layer damping, loss factor.

INTRODUCTION

There is many sources of sounds and vibrations in the aircraft structures and the cars. The main reason of vibrations is an unbalanced engine. The next sources of vibrations are related to: aerodynamics (i.e. fluctuations of pressure in the boundary layer of the stream flowing around the structure) and mechanics (i.e. driving wheeled vehicles on uneven surfaces). The large amplitudes of vibrations can be reason for decrease of the fatigue life of structures. Moreover the high level of noise in the pilots or drivers cabin has an indirect influence on the safety of the air and car transport.

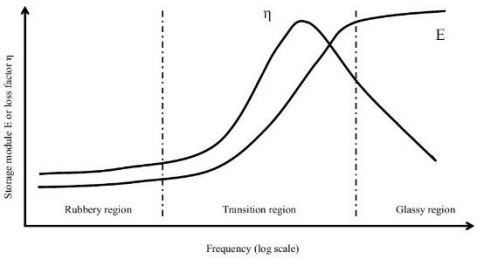

Fig. 1 Loss factor and storage modulus as a function of frequency [1, 6, 14]

From mentioned above reasons there is need to decrease a noise in the cabin, mainly in aviation and the automotive industry. The first way to decrease the vibration of aircraft structures and cars is minimization of vibrations of engine. Unfortunately each turbine engine (and especially the piston engine) cannot be perfectly balanced.

Vibrations are transmitted in various ways, generating unpleasant noise and directly affecting the human body and the vehicle structure. For example, in the aircraft during flight, the compressor blades are subjected to vibration. The resonant vibrations decrease the fatigue life of the blades [5, 15-17]. The most common way of suppressing vibration is attaching to the face of an element the layer made of damping material. Viscoelastic polymers are commonly used in automotive and aviation industry as passive damping [1, 18]. Such materials have both viscous and elastic properties. Because viscoelastic polymers have such features, after removing the load from them, some of the energy is recovered and some is dissipated in the form of thermal energy. Their damping capabilities strongly vary with the temperature and frequency (**Figs 1, 2**). The best damping effect (**Fig. 1**) is achieved in transition region, where the loss factor has the highest value. The storage modulus E' has the highest value in the glassy region.

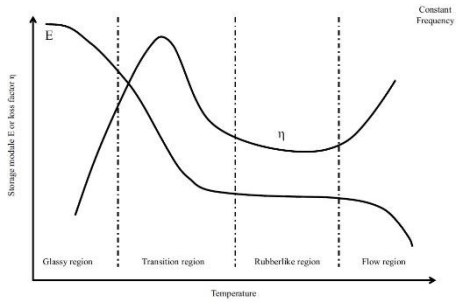

Fig. 2 Loss factor and storage modulus as a function of temperature [1, 6, 14]

The most effective way for using viscoelastic materials are free layer damping (FLD, **Fig. 3**) and constrained layer damping (CLD [18,19, 20]).

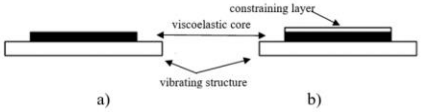

Fig. 3 Viscoelastic materials damping: FLD treatment (a) and CLD treatment (b)

The first configuration dissipates energy caused by vibration, through extension, the second one mostly due to shear. FLD treatment is basically a viscoelastic layer connected with the structure. In CLD treatment a thin constraining layer is added, providing the shear deformation [2]. The aim of those treatments is to minimize vibration amplitude of the structure. In consequence the decrease of both the noise and stress is observed. It also causes extension of the fatigue life. The most common viscoelastic materials used in automotive and aviation industry are butyl rubber and bitumen-based material. The advantage of this approach is no need of external source of power like in active vibration isolation. Viscoelastic materials work best in high range of frequency. In some situations, such passive damping cannot be used at high temperature [7].
Kerwin [8, 9] was one of the first who observed that a stiff constraining layer placed on top of the viscoelastic layer can increase the damping capabilities. In his work, he also examined the influence of temperature on the loss factor. Di Taranto [10] developed an analytical model of a freely vibrating beam with free boundary conditions, which enables the determination of the damping coefficient. Mead and Markus [11] derived mathematical formula determining the transverse displacement of a three-layer beam with a viscoelastic core. Rao [12] presented the formula for the natural frequency and the loss factor for a multi-layer beam under different boundary conditions. Hujare and Sahasrabudhe [13] conducted a study of CLD treatment with various damping materials. The damping properties of seven kinds of viscoelastic materials were investigated. The considered beam was symmetrical in the form of a sandwich structure.

EXPERIMENTAL ANALYSIS

In order to determine the damping capabilities of investigated viscoelastic materials, the experimental modal analysis was performed. During the experiment the Unholtz-Dickie UDCO TA-250 electrodynamic vibration system (equipped with the shaker, controller and the amplifier) was used. In **Fig. 4** the investigated beam covered by bitumen based material was shown. The beam was fixed to the movable head of the shaker. During the experiment the Oberst beam method was utilized [2]. As a base beam a steel cantilever was used. It is typical material for such analysis, because it has very low loss factor and its storage modulus does not depend on frequency [1].

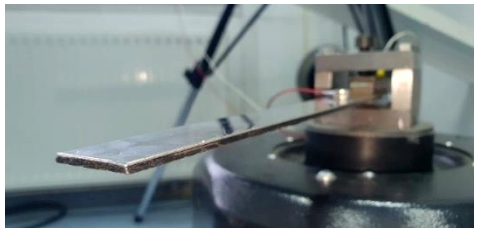

Fig. 4 View of investigated beam covered by bitumen based material. The beam was fixed to the movable head of the shaker using the special grip

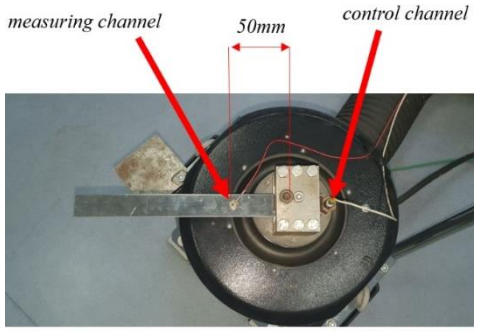

Fig. 5 Top view of the experimental setup. Location of the acceleration sensors used in modal analysis (related to the measure and control channel)

The dimensions of investigated beam were as follows: length 250 mm, width 20 mm, thickness 1 mm. The thickness of damped material was 2 mm. In performed experiment three configurations were studied. In first configuration the steel beam (specimen 1, without damping material) was examined. In second configuration the beam was covered by bitumen-based material (specimen 2). The last examined specimen (no. 3) was the steel beam with layer made of the butyl rubber. The specimens were constructed based on the ASTM Standard E756(05) [3] and were investigated at room temperature (20 °C) in frequency range from 20 Hz to 4 kHz. The modal analysis was performed at constant intensity of excitation 1g (where $1g = 9{,}81\ m/s^2$). The intensity of excitation (vibration) was measured using the piezoelectric vibration sensor on the movable head of shaker (**Fig. 5**). Signal from this sensor was assigned to the control channel. The second vibration sensor was located on the beam, 50 mm from the restraint (**Fig. 5**). Signal from this sensor was assigned to the measure channel and was used to creation of frequency-amplitude characteristics, for all investigated specimens.

RESULTS AND DISCUSSION

The results of performed modal analysis are presented as Frequency Response Function (FRF). Based on the ASTM

Standard E756(05) [3] the measure was started from the second mode of resonant vibration of the beam.
Obtained results of experimental modal analysis showed that the best damping of beam is observed for frequencies above 1000 Hz. For first considered modes (from 2nd to 4th) the moderate damping effect is observed. From fifth investigated mode, the strong damping effect of the beam is visible. The quantitative results of performed modal analysis were presented in **Table 1**. In order to compare the damping effect of investigated materials, the relative amplitudes (A2/A1 and A3/A1 were computed for each resonance. In the relative amplitude calculation, the amplitude A2 of damped beam (covered by bitumen material) was divided by amplitude A1 of separated beam (without any damping material).

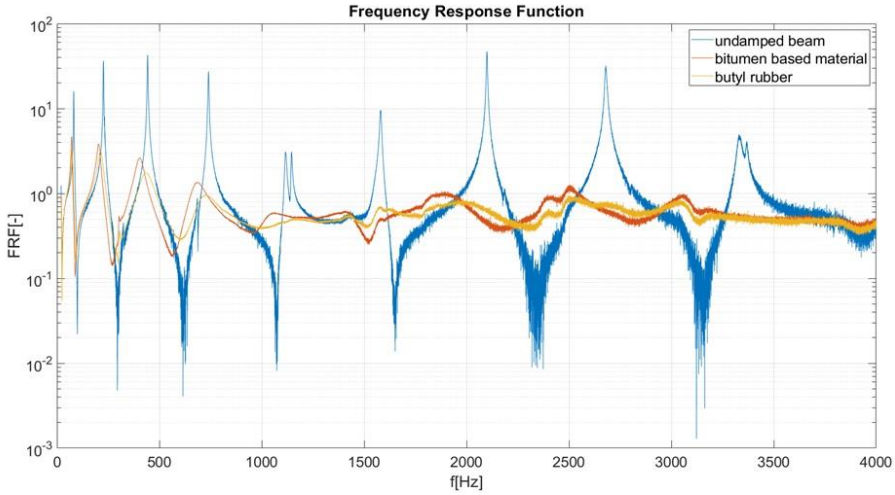

Fig. 6 Frequency response curves for considered specimens

Table 1 Frequency of resonant vibration and amplitude of acceleration of specimens

Specimen 1 (beam without damping)			**Specimen 2 (beam and bitumen-based material)**			**Specimen 3 (beam and butyl rubber)**		
No. of mode	Freq. of resonant vibration [Hz]	Ampl. of accel. A_1 [g]	Freq. of resonant vibration [Hz]	Ampl. of accel. A_2 [g]	Relative ampli-tude A_2/A_1 [-]	Freq. of resonant vibration [Hz]	Ampl. of accel. A_3 [g]	Relative ampli-tude A_3/A_1 [-]
2	81.3	15.89	71.9	4.674	0.294	74.0	3.502	0.220
3	226.8	36.27	203.7	3.852	0.106	212.1	3.128	0.086
4	444.5	42.36	403.2	2.6	0.061	434.4	1.763	0.042
5	741.5	27.2	686.2	1.351	0.050	730.5	0.9606	0.035
6	1115.8	3.098	1059	0.59	0.190	1169	0.5082	0.164
7	1146.4	3.097	1408	0.6289	0.203	1435	0.5425	0.175
8	1584.3	9.591	1581	0.521	0.054	1581	0.7061	0.074
9	2100	47.21	1879	1.073	0.023	1982	0.8722	0.018
10	2680	31.79	2503	1.266	0.040	2501	0.9557	0.030
11	3331	4.957	3059	0.9891	0.200	3057	0.8526	0.172
12	3368	4.084	3185	0.7136	0.175	3185	0.5941	0.145

Obtained results of investigations (**Fig. 6**, **Table 1**) showed that after adding the damping mats to the beam an amplitude of acceleration (during resonances) significantly decreased. The results presented in **Table 1** shows that the butyl rubber provides (for most modes) a bit more effective damping than the bitumen material. Both the butyl rubber and the bitumen material achieve the best results in damping at the following modes of vibration: 4, 5, 8-10. For these modes the amplitude of acceleration was decreased more than 10 times.

For better estimation of the damping factor from frequency domain, a half-power bandwidth method was used. In this method the amplitude of FRF was used. In first part of the procedure the amplitude A_{max} and frequency f_o for each resonance were extracted (**Fig. 7**). In next step the value of A_{max} was divided by $\sqrt{2}$. The vertical line (which has coordinate $A_{max}/\sqrt{2}$) intersects the curve at 2 points. The first coordinate of intersection points are: f_1 and f_2. These frequencies are used in half power bandwidth method (**Fig. 7**).

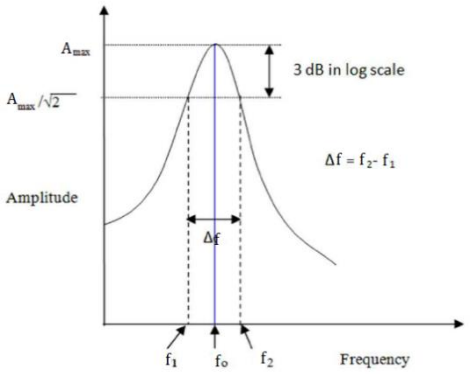

Fig. 7 Visualization of half power bandwidth method [4]

Structural loss factor η is equal to twice the viscous damping factor ζ [1]. Using equation shown below, the loss factors have been computed for every investigated mode of resonant vibration.

$$\eta = 2\zeta = \frac{\Delta f}{f_0} = \frac{f_2 - f_1}{f_0} \quad (1.)$$

where: η [-] – loss factor

ζ [-] – damping factor

f_0 [Hz] – natural frequency

f_2, f_1 [Hz] –frequencies used in half power bandwidth method (**Fig. 7**)

The frequencies f_1 and f_2 were next used for calculation of the damping capabilities of examined materials. The structural loss factor and the damping factor for considered beams are presented in **Table 2**.

Obtained results of investigations (**Fig. 6**, **Table 2**) showed that after adding the damping mats to the beam, the loss factor and the damping factor significantly increased. The beam without damping (specimen 1) has very low loss factor for all modes. The small value of loss factor is typical for the steel, which dissipates very much of energy during vibration. Performed experiment showed that both the butyl rubber and the bitumen material increased the structural damping significantly. For modes in medium frequency range the loss factor achieves the highest values (**Table 2**).

In **Fig. 8** the relative damping factor of specimen no. 2 and 3 was shown. From this figure is visible that for specimen 3 (beam with butyl rubber) the highest values of relative damping were observed. It means that the butyl rubber has better damping properties than the bitumen material. The highest values of relative damping factor were observed for modes 4-7 and 9.

Table 2 Loss factor, damping factor and relative damping factor of specimens

Specimen 1 (beam without damping)			**Specimen 2 (beam and bitumen-based material)**			**Specimen 3 (beam and butyl rubber)**		
No. of mode	Loss factor (η_1) [-]	Damping factor (ζ_1) [-]	Loss factor (η_2) [-]	Damping factor (ζ_2) [-]	Relative damping factor ζ_2/ζ_1 [-]	Loss factor (η_3) [-]	Damping factor (ζ_3) [-]	Relative damping factor ζ_3/ζ_1 [-]
2	0.032	0.016	0.067	0.033	2.1	0.095	0.047	3.0
3	0.011	0.006	0.083	0.042	7.6	0.118	0.059	10.7
4	0.006	0.003	0.104	0.052	18.5	0.147	0.074	26.2
5	0.005	0.003	0.112	0.056	20.8	0.159	0.079	29.4
6	0.008	0.004	0.154	0.077	19.1	0.256	0.128	31.7
7	0.005	0.003	0.131	0.065	25.0	0.132	0.066	25.3
8	0.005	0.003	0.021	0.010	4.1	0.025	0.012	4.9
9	0.002	0.001	0.103	0.052	48.2	0.151	0.075	70.4
10	0.003	0.002	0.033	0.016	9.8	0.053	0.026	15.7
11	0.007	0.003	0.046	0.023	7.0	0.050	0.025	7.5
12	0.004	0.002	0.026	0.013	5.9	0.038	0.019	8.6

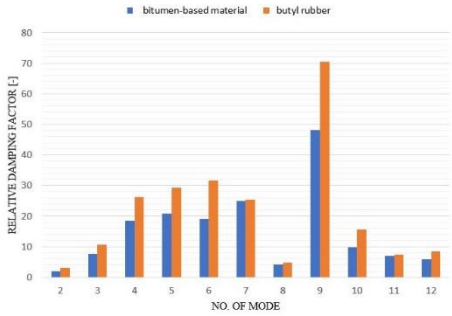

Fig. 8 Relative damping factor of specimen no. 2 and 3

CONCLUSIONS

In this study the experimental modal analysis of beams covered by the viscoelastic material was performed. Viscoelastic materials, especially the bitumen and the butyl rubber are often used in automotive and aviation industry in order to damping the vibrations of thin-walled structures. In this work three specimens were examined (steel beam without damping material, the beam with bitumen material and the beam covered by the butyl rubber layer). During experimental investigation both the natural frequencies and also the vibration amplitude of examined specimens were obtained. In order to define the damping capabilities the relative amplitude and also the loss factor using half-power bandwidth method were computed. Obtained results of investigations (**Fig. 6**, **Fig. 8**, **Table 1**, **Table 2**) showed that after adding the damping mats to the beam an amplitude of acceleration (during resonances) significantly decreased. The results presented in **Tables 1** and **2** shows that the butyl rubber provides (for most modes) a bit more effective damping than the bitumen material. The highest loss factor is achieved in medium frequency range. Obtained results are important from both the research and also the practical point of view because the passive damping of vibration is used in many branches of industry (automotive, aviation, railway technology). Reduction of vibration amplitude causes increase of the fatigue life of thin-walled structures. Moreover, the passive damping of vibration causes reduction of noise in cabins of cars and aircraft what indirectly affects the safety of transport.

REFERENCES

1. M.D. Rao: Journal of Sound and Vibration, 232, 2003, 457-474. http://dx.doi.org/10.1016/S0022-460X(03)00106-8.
2. D.I.G. Jones: *Handbook of Viscoelastic Vibration Damping*, first ed., John Wiley & Sons Ltd, West Sussex, 2001.
3. ASTM E756-05(2017), Standard Test Method for Measuring Vibration-Damping Properties of Materials, ASTM International, West Conshohocken, PA, 2017. https://doi.org/10.1520/E0756-05R17.
4. D. Ewins.: *Modal Testing: Theory and Practice*, first ed., Research Studies Press Ltd., Taunton, 1984
5. L. Witek: Engineering Failure Analysis, 16(7), 2009, 2163-2170. https://doi.org/10.2478/v10164-010-0017-7.
6. S. Mazurkiewicz: Journal of Theoretical and Applied Mechanics, 7 (1), 1969, 25-37.
7. J. Depriest: SAE International Transactions Journal of Aerospace, 109 (1), 2001. https://doi.org/10.4271/2000-01-1708.
8. D. Ross, E.M. Kerwin, E.E. Ungar: Structural Damping, 1959, 49–88.
9. E.M. Kerwin: Journal of the Acoustical Society of America, 31, 1959, 952–962. https://doi.org/10.1121/1.1907821.
10. R.A. Di Taranto: ASME Journal of Applied Mechanics, 32, 1965, 881–886. https://doi.org/10.1115/1.3627330.
11. D.J. Mead, S. Markus: Journal of Sound and Vibration, 10 (2), 1969, 163–175. https://doi.org/10.1016/0022-460X(69)90193-X.
12. Y.V.K.S. Rao, B.C. Nakra: Journal of Sound and Vibration, 34, 1974, 309–326. http://dx.doi.org/10.1016/S0022-460X(74)80315-9.
13. P.P. Hujare, A.D. Sahasrabudhe: Procedia Materials Science, 5, 2014, 726-733. https://doi.org/10.1016/j.mspro.2014.07.321.
14. A.D. Nashif, D.I.G Jones, J.P. Henderson: *Vibration Damping*. John Wiley and Sons, New York, 1985.
15. L. Witek: Engineering Failure Analysis, 13(1), 2006, 9-17. https://doi.org/10.1016/j.engfailanal.2004.12.028.
16. L. Witek: Engineering Failure Analysis, 18(4), 2011, 1223-1232. https://doi.org/10.1016/j.engfailanal.2011.03.003.
17. L. Witek: Key Engineering Materials, 598, 2014, 269-274. https://doi.org/10.4028/www.scientific.net/KEM.598.269.
18. Balmes, Etienne, et al.: Structural Dynamics, 3, 2011, 1177-1185.
19. A.A. Hanieh, A. Albalasie: Procedia Manufacturing, 33, 2019, 770-777. https://doi.org/10.1016/j.promfg.2019.04.097.
20. Z. Xie, W.S. Shepard Jr.: Journal of Sound and Vibration, 319, 2009, 1271-1284. https://doi.org/10.1016/j.jsv.2008.

ACTA METALLURGICA SLOVACA
2021, VOL. 27, NO. 2, 68-71

RESEARCH PAPER

PREDICTION THERMO-PHYSICAL CHARACTERISTICS HEAT-RESISTANT NICKEL ALLOYS DIRECTIONAL CRYSTALLIZATION

Alexander Anatolyevich Glotka[1]*, Vadim Efimovich Ol'shanetskii[1]

[1] Zaporizhzhia Polytechnic National University, Ukraine, Zaporizhzhia, st.Zhukovskogo, 64, 69063

*Corresponding author: glotka-alexander@ukr.net, tel.: +380964275651, Zaporizhzhia Polytechnic National University, Ukraine, Zaporizhzhia, st. Zhukovskogo, 64, 69063

Received: 11.01.2021
Accepted: 31.01.2021

ABSTRACT

The paper presents a comparative analysis of the practical and calculated values of the thermophysical properties of heat-resistant nickel alloys of directional solidification. Using an empirical approach, new ratios of the elements Kγ′ and Kγ have been obtained for the first time, which take into account the combined effect of alloying elements on the temperature of multicomponent compositions of cast heat-resistant alloys. The calculated values of the critical temperatures for the Ni-6Al-9Co-8W-4Re-4Ta-1.5Nb-1Mo-0.15C system are in good agreement with the experimental ones. The dependence of the Kγ ratio on the alloying system; the influence of alloying on the liquidus temperature of the alloys is studied. The ratios of the content of alloying elements and regression models that can be used to predict the width of the crystallization temperature range and the optimal homogenization temperature for a particular alloy are presented.

Keywords: casting heat-resistant nickel alloys directional solidification, thermodynamic processes phase separation, critical temperatures

INTRODUCTION

In recent years, the development of jet aircraft, the temperature of the hydrogen-containing gas at the turbine inlet has increased from 1200 K in the second-generation engines to 1800-1950 K in the fifth-generation engines. About 70% of this increase was obtained due to the improvement of air-cooling systems for gas turbine blades, and 30% - as a result of an increase in the level of mechanical properties of heat-resistant nickel alloys (HRNA) [1 - 5].

The main thermophysical and structural-phase characteristics that determined the choice of the most promising compositions of the developed alloys were the temperatures: complete dissolution of the γ'-phase in the matrix γ-solid solution $t_{c.d}$ (solvus γ '), local melting of the nonequilibrium eutectic (peritectic) γ + γ ', solidus t_S and liquidus t_L. The achievement of the maximum values these temperatures (thermodynamic stability of the phases) determines the high temperature performance and creep resistance of the HRNA [6-9]. It should be noted that while striving to increase the critical temperatures $t_{c.d}$, t_{eut}, t_S and t_L, it is necessary to provide a sufficient temperature interval - (t_{eut} - $t_{c.d}$) to eliminate the risk of melting during homogenizing annealing [10-15].

As a result of this empirical approach, heat-resistant nickel alloys are the most complex alloys for structural purposes, since they contain more than 15 alloying and microalloying elements. Currently, with alloys of this class, tests are being carried out to optimize the chemical composition, which will make it possible to obtain the required set of properties [16-23].

The purpose of this work is to obtain predictive regression models, with the help of which, it is possible to adequately calculate the critical temperatures for the HRNA directional crystallization, without conducting preliminary experiments.

MATERIAL AND METHODS

For experimental and theoretical studies of temperature performance, a working sample of alloys was formed, consisting of well-known industrial HRNA for directional crystallization of domestic and foreign production, the following brands: ZhS-26, ZhS-26U, ZhS6F, ZhS-28, ZhS-30, VZhL-20, GTD-111, Mar-M247, CM-247LC, Mar-M200 + Hf, Mar-M246 + Hf, U-500, U-700, PWA-1422, PWA-1426, CM-186LC, Rene 142, Rene 150, IN-792LC, DS-16, Mar-M002, Rene 125, Rene 80H. The selection of alloys was made from the standpoint of a variety of chemical compositions (alloying systems), which have a wide alloying range in terms of the content of the main elements.

The obtained values were processed in the Microsoft Office software package in the EXCEL package to obtain correlation dependences of the "parameter-property" type with obtaining mathematical equations of regression models that optimally describe these dependences. The dependences have a sufficiently high coefficient of determination $R^2 \geq 0.85$ and are suitable for determining the temperature characteristics of the HRNA.

RESULTS AND DISCUSSION

The heat resistance of alloys is determined by the thermodynamic stability of the phases, which is proposed to be estimated by the temperatures $t_{c.d}$, t_{eut}, t_S, and t_L. Development of a method for calculating these values from the chemical composition of the alloy is an urgent task.

All components used for alloying HRNA can be conditionally divided into three groups: dissolving mainly in the γ-solid solution (Co, Cr, Mo, W, Re), dissolving mainly in the-phase (Al, Ti, Ta, Hf) and carbide-forming elements (Ti, Ta, Hf, Nb, V, W, Mo, Cr).

On the other hand, many elements can be included in the γ′-phase: Al, Ti, Nb, Cr, Co, Mo, W, V, etc. But their content in the γ′-phase and the effect on its amount in the structure are different. This effect is associated with the ability of the elements to form stable intermetallic phases of the Ni_3Me type with nickel. Hence, it follows that the critical temperatures of alloys are influenced not only by the elements that belong to γ′-forming, but also those that are classified as γ-solid hardeners.

As a result of processing the experimental data and the above reasoning, the relationship $K_{\gamma'}=5\frac{\sum_{\gamma'}(Al+Ti+Nb+Ta+Hf)}{\sum_{\gamma}(Cr+W+Mo+Re+Co+Ru)}$ elements to assess the thermodynamic stability of phases, which takes into account the complex effect of all alloy components. This ratio correlates well with the temperatures $t_{c.d}$, t_{eut} and t_S, Δt_{homo}, °C which, in turn, correlate well with the heat resistance of the alloys. Also, this ratio can be used in the design of other types of heat-resistant nickel-based alloys [24].

The relationship between the temperatures of complete dissolution of the γ′-phase, eutectic transformation and solidus with the proposed Kγ′ ratio (**Fig. 1**) is adequately described by regression models (**Table 1**). An increase in the thermophysical characteristics of alloys with an increase in the parameter Kγ′ is associated with an increase in alloying of the alloys with both γ-forming elements and elements in the γ-solid solution. However, at a value of 1.6 ... 1.7 Kγ′, a decrease in temperatures $t_{c.d}$ and t_S is observed, due to the peculiarities of alloying in this range, namely, an increase in the content of elements that are classified as γ-hard mortar hardeners. With an increase in the value over 2.2 ... 2.3 Kγ′, an increase in the temperatures $t_{c.d}$ and t_S is observed, which is associated with a change in the interatomic bond forces (due to an increase in alloying alloying).

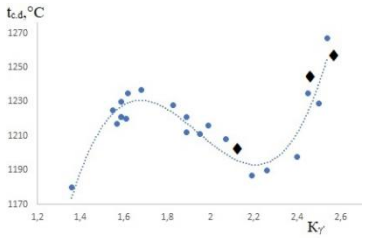

a

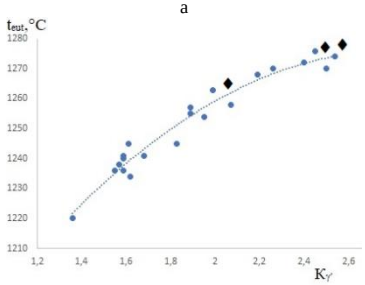

b

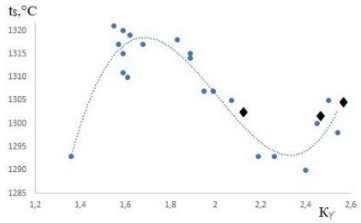

c

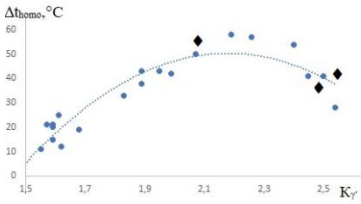

d

Fig. 1. - Dependence critical temperatures and homogenization interval on the ratio alloying elements in the composition of the HRNA: a – $t_{c.d.}=f(K_{\gamma'})$; b – $t_{eut}=f(K_{\gamma'})$; c - $\Delta t_{homo}=f(K_{\gamma'})$; d - $t_S=f(K_{\gamma'})$. (•- calculated values; ♦ - experimental values)

Using the constructed regression models (**Table 1**), it is possible to predict with high accuracy the critical temperatures of alloys without preliminary experiments by the method of differential thermal analysis, and also to calculate the width of the temperature range for efficient homogenizing annealing depending on the content of alloying elements in the alloy.

Table 1 Dependences of the thermophysical characteristics of the liquid pumping station on the parameters Kγ′ and Kγ.

Critical temperature	Predictive regression models
Temperatures of complete dissolution of the γ′-phase	$t_{c.d.}=504{,}84(K_{\gamma'})^3-2942{,}7(K_{\gamma'})^2+5611{,}1(K_{\gamma'})-2284{,}3$
Temperature of eutectic transformation γ + γ '	$t_{eut}=-26{,}039(K_{\gamma'})^2+145{,}92(K_{\gamma'})+1071{,}5$
Temperature range for homogenizing annealing	$\Delta t_{homo}=-97{,}465(K_{\gamma'})^2+424{,}79(K_{\gamma'})-412{,}46$
Solidus temperature	$t_S=186{,}75(K_{\gamma'})^3-1125{,}5(K_{\gamma'})^2+2202{,}4(K_{\gamma'})-90{,}528$
Liquidus temperature	$t_L=-10{,}235(K_{\gamma})^2+75{,}121(K_{\gamma})+1234{,}1$
Crystallization temperature range	$\Delta t_{cryst}=49{,}07(K_{\gamma'})^3-318{,}68(K_{\gamma'})^2+978{,}96(K_{\gamma'})-777{,}42$

However, the relationship between the Kγ′ ratio and the liquidus temperature turned out to be ambiguous. The initial dependence had a low coefficient of determination ($R^2 \le 0.1$). This is explained by the fact that at temperatures close to the melting point, there are two phases in the structure, a liquid and γ-solid solution. The liquidus temperature is associated with the thermodynamic stability of the solid solution, which is influenced by the refractory elements in it, they dissolve mainly in the γ-solid solution and significantly increase the thermodynamic stability of the phases in the HRNA due to the low diffusion coefficient, which leads to inhibition of the mobility of atoms in γ- phase. Therefore, after processing the experi-

mental data, and following the above judgments, the following ratio of elements was proposed for the first time:

$$K_\gamma = \frac{\sum_\gamma (Cr+W+Mo+Re+Co+Ru)}{\sum_{\gamma'} (Al+Ti+Nb+Ta+Hf)}$$, which makes it possible to accurately predict the liquidus temperature and the temperature range of the HRNA crystallization [24].

Figure 2 shows the dependences of the liquidus temperature and the crystallization interval on the Kγ ratio. The liquidus temperature increases with an increase in the value of Kγ, which is typical with an increase in elements that are in a solid solution. The dependence of the temperature range of crystallization on the value of Kγ has a similar character with $t_{c.d}$ and ts and obeys the above relationships.

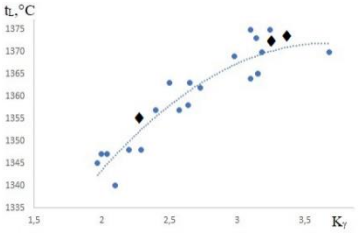

a

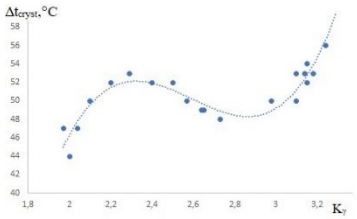

b

Fig. 2. - Dependence of the liquidus temperature (a) and the crystallization interval (b) on the Kγ ratio. (• - calculated values; ♦ - experimental values)

Thus, using the above regression models (**Table 1**), it is possible to calculate the liquidus temperature and the width of the crystallization temperature range, which significantly affects the manufacturability of the alloy during the formation of a defect-free structure in castings.

The results of calculating the thermophysical characteristics of the directed crystallization HRNA were further compared with the experimental data obtained using differential thermal analysis (DTA). To confirm the calculated data, industrial high-temperature nickel alloys of the Ni-6Al-9Co-8W-4Re-4Ta-1.5Nb-1Mo-0.15C system (ZhS32-VI, ZhS32B-VI and ZhS32E-VI) were selected. Based on the analysis of the experimentally obtained data on the critical temperatures of phase transformations on the experimental alloys, **Table 2** presents the values of the calculated thermophysical characteristics obtained using an active experiment.

Table 2 Calculated and experimental thermophysical characteristics HRNA

Method of obtaining results	Critical temperatures, °C					
	$t_{c.d}$	t_{eut}	t_S	t_L	Δt_{homo}	Δt_{cryst}
ZhS32-VI						
Calculated	1205	1265	1303	1355	55	53
Experimental	1197	1260	1298	1352	48	54
ZhS32B-VI						
Calculated	1250	1273	1302	1372	31	70
Experimental	1230	1270	1296	1368	40	72
ZhS32E-VI						
Calculated	1261	1278	1306	1376	37	69
Experimental	1250	1271	1297	1367	35	70

Table 2 shows that the calculated and experimental data are in good agreement with each other in almost all characteristics. Based on the calculated and experimental values obtained, the error does not exceed 15°C, thus, the obtained mathematical dependences make it possible to predict the thermophysical characteristics, which depend on the alloying system of the alloy, both in the development of new compositions of the HRNA for directional crystallization, and in the improvement of known industrial compositions within the brand composition.

CONCLUSION

1. On the basis of an integrated approach, both computational and experimental, for multicomponent liquid pumping stations, new regression models have been obtained that make it possible to adequately predict the thermophysical characteristics by the chemical composition of the alloy. On the basis of the thermodynamic approach, new ratios of Kγ′ and Kγ have been obtained for the first time; by their value, one can adequately predict the temperature characteristics for multicomponent compositions of directional crystallization of HRNA.

2. The dependences of the ratio of Kγ′ to the temperatures of complete dissolution of the γ′ phase, eutectic transformation and solidus have been revealed; they are explained by the connection between alloying of the alloy with γ′-forming elements, and being in the γ-solid solution.

3. It has been established that the liquidus temperature increases with an increase in the value of Kγ, which is typical with an increase in elements that are in a solid solution. The dependence of the temperature range crystallization on the value of Kγ has a similar character with $t_{c.d}$ and t_S.

4. The results obtained show that the ratios of such a group of elements practically unidirectionally affect the diagrams (behavior of figurative points of state diagrams from virtual alloys) of the considered heat-resistant alloys. Good agreement between the calculated and experimental results made it possible to believe that the "intersection" of multidimensional

parabolas of various hypersurfaces of phase equilibria makes it possible to obtain a binary section of conditional equilibrium diagrams with lines of equilibrium phases corresponding to physical reality.

5. A promising and effective direction is shown in solving the problem of predicting the thermodynamic stability of alloy phases, which affects the service properties of alloys both in the development of new HRNA and in the improvement of the compositions of well-known industrial brands of this class.

REFERENCES

1. B. G. Choi, I. S. Kim, D. H. Kim, C. Y. Jo: Solid State Phenomena, 124–126, 2007, S1505–1508. https://doi.org/10.4028/www.scientific.net/ssp.124-126.1505.
2. M. Kvapilova, J. Dvorak, P. Kral, K. Hrbacek, V. Sklenicka: High Temperature Materials and Processes, 38, 2019, 590-600. https://doi.org/10.1515/htmp-2019-0006.
3. N. V. Petrushin, E. S. Elyutin, R. M. Nazarkin, S. I. Pakhomkin, V. G. Kolodochkina, T. V. Fesenko, E. S. Dzhioeva: Inorg. Mater. Appl. Res., 7, 2016, 824–831. https://doi.org/10.1134/S2075113316060149.
4. S. M. Seo, I. S. Kim, J. H. Lee, C. Y. Jo, H. Miyahara, K. Ogi: Metall. Mater. Trans. A, 38, 2007, 883–893. https://doi.org/10.1007/s11661-007-9090-0.
5. O. I. Balyts'kyi, O. O. Krokhmal'nyi: Mater Sci., 35, 1999, 389–394. https://doi.org/10.1007/BF02355483.
6. A. M. S. Costa, E. S. N. Lopes, R. J. Contieri, R. Caram, R. Baldan, G. E. Fuchs, et al: J. Mater. Eng. Perform, 28, 2019, 2427-2438. https://doi.org/10.1007/s11665-019-04014-1.
7. Yu. A. Bondarenko, A. B. Echin, V. E. Bazhenov, A. V. Koltygin: Russian Journal of Non-ferrous Metals, 58, 2017, 481–488. https://doi.org/10.3103/S1067821217050042.
8. A. Balyts'kyi: 6th International Conference "*Fracture Mechanics of Materials and Structural Integrity*", 16, 2019, 134–140. https://doi.org/10.1016/j.prostr.2019.07.032.
9. N. Das: Trans. Indian. Inst. Met., 63, 2010, 265–274. https://doi.org/10.1007/s12666-010-0036-7.
10. K. Mukai, Z. Li, K. C. Mills: Metall. Mater. Trans. B, 36, 2005, 255–262. https://doi.org/10.1007/s11663-005-0027-y.
11. Z. Li, K. C. Mills: Metall. Mater. Trans. B 37, 2006, 781–790. https://doi.org/10.1007/s11663-006-0060-5.
12. J. Huang, X. Yang, D. Shi, H. Yu, X. Hu: J. Mater. Sci., 49, 2014, 7625–7638. https://doi.org/10.1007/s10853-014-8418-6.
13. L. Li, A. Deceuster, C. Zhang: Metallogr. Microstruct. Anal., 1, 2012, 92–98. https://doi.org/10.1007/s13632-012-0016-x.
14. M. Z. Alam, N. Hazari, D. K. Das: Bull. Mater. Sci., 37, 2014, 1551–1561. https://doi.org/10.1007/s12034-014-0110-6
15. Yu. H. Kvasnytska, L. M. Ivaskevych, O. I. Balytskyi, I. I. Maksyuta, H. P. Myalnitsa: Mater. Sci., 56, 2020, 432–440. https://doi.org/10.1007/s11003-020-00447-5.
16. L. Li: J. Mater. Sci., 41, 2006, 7886–7893. https://doi.org/10.1007/s10853-006-0948-0.
17. O. A. Glotka, S. V. Haiduk: Metallofiz. Noveishie Tekhnol., 42(6), 2020, 869-884 (in Russian) https://doi.org/10.15407/mfint.42.06.0869.
18. J. Song, D. Tang, C. Xiao, D. Wang, Q. Yu: Rare Metals, 30, 2011, 383–387. https://doi.org/10.1007/s12598-011-0308-3.
19. M. Suave, L. Muñoz, A. S. Gaubert: Metall. Mater. Trans. A, 49, 2018, 4012–4028. https://doi.org/10.1007/s11661-018-4708-y.
20. O. N. Senkov, D. W. Mahaffey, S. L. Semiatin: Metall. Mater. Trans. A, 45, 2014, 5545–5561. https://doi.org/10.1007/s11661-014-2512-x.
21. J. Zhang, R. F. Singer: Metall. Mater. Trans. A, 35, 2004, 1337–1342. https://doi.org/10.1007/s11661-004-0308-0.
22. H. Y. Qi, J. S. Yang, X. G. Yang, L. Shao-Lin: Rare Metals, 38, 2019, 227–232. https://doi.org/10.1007/s12598-016-0862-9.
23. A. A. Glotka, S. V. Gaiduk: J Appl Spectrosc, 87, 2020, 812–819. https://doi.org/10.1007/s10812-020-01075-2.
24. A. A. Hlotka, S. V. Haiduk: Mater. Sci., 55, 2020, 878–883. https://doi.org/10.1007/s11003-020-00382-5.

ACTA METALLURGICA SLOVACA
2021, VOL. 27, NO. 2, 72-76

RESEARCH PAPER

IMPROVING THE MECHANICAL PROPERTIES OF Al-Cu-Mg-Mn ALLOY TUBES THROUGH PLASTIC DEFORMATION

Trung-Kien Le*[1], Dac-Trung Nguyen[1], Tuan-Anh Bui[1]

[1]School of Mechanical Engineering, Hanoi University of Science and Technology, No. 1 Dai Co Viet Road., Hanoi, Vietnam

*Corresponding author: kien.letrung@hust.edu.vn, Hanoi University of Science and Technology, No. 1 Dai Co Viet Rd., Hanoi, Vietnam.

Received: 07.01.2021
Accepted: 17.02.2021

ABSTRACT

The effect of plastic deformation upon the grain structure and mechanical properties of Al-Cu-Mg-Mn alloy tubes under upsetting was investigated. It was found that plastic deformation techniques such as cold upsetting can overcome the disadvantages of the cutting process, such as the anisotropy of the original material, no grain structure, and not high mechanical properties, while also improving the mechanical properties of the product in local plastic deformation zones by changing the grain and fiber structure of the material. This article presents the results of our research and evaluates the increase of material durability in the tubes' deformation zones compared with the initial state. In this study Al-Cu-Mg-Mn alloy material had been cutting with turn machine and plastic deformation by upsetting. Microstructures and hardness variations of cut surfaces that are obtained with different processes have been investigated.

Keywords: Al-Cu-Mg-Mn; Fiber structure; metal forming; tube cold upsetting

INTRODUCTION

Aluminum alloy is a light-weight, corrosion-resistant metal with a good load capacity; however, its strength is insufficient for many applications in engineering and equipment operating under high mechanical loads. Therefore, it is important to find ways to improve the mechanical properties while maintaining the lightness and specific strength of aluminum alloys. Modern approaches to this problem include ultrafine grinding of the alloys' grain structure by methods such as plastic deformation [1-7], as well as heat treatment methods such as annealing by stimulating static recrystallization [8], and aging after hardening and high-pressure torsion [9]. In fact, plastic deformation is often applied to increase the mechanical properties of a solid material [10-14]. Presently, few studies have considered hollow parts. Methods for steels [15], such as extrusion, rolling, and brazing [16], can also be applied as a hydrostatic forming method for copper [17]. These studies are mainly for tubes with a relatively small thickness and height. Currently, aluminum tubes with a special long shank shape and relatively large thickness are mainly machined from solid workpieces [18, 19]. The major disadvantage of cutting methods is the low coefficient of the using material, especially when the part has a variable cross section and diameter [20]. The machined parts are often stress concentrated at the changed sections, so they are often broken or destroyed when working. Tubular parts can also be fabricated by an extrusion method; however, because direct extrusion generates tremendous friction and heat between the billet and the container wall, pressure and temperature vary during the extrusion process. The result is an inconsistent grain structure and compromised metallurgical properties in the finished product [21]. To overcome the shortcomings of manufacturing parts with these methods, our research team has proposed the application of pressure machining techniques such as upsetting and testing for thin tubes of variable thickness. The tube upsetting technology has the advantage of optimizing the weight of the workpiece. This saves materials because, during the formation process, the tube thickness will be distributed according to the structure of the workpiece. Additionally, this method will save time, reduce the cost of the machining process, and improve the part's mechanical properties because the deformation process will create the necessary grain direction, avoiding stress concentration at the position where the cross section changes [1].

When using a tube upsetting technology, folding defects may appear because the upsetting height is much larger than the tube thickness. Therefore, it is necessary to calculate and select suitable technological parameters [22-24]. Currently, the tube upsetting technology is quite suitable for forming aluminum materials in a cold state. After shaping a specific workpiece, it is necessary to evaluate and analyze its ability to meet technical requirements based on the consideration of the folding defects, metal microstructure in deformed areas, and metal-grain direction and to compare its mechanical properties with those of the original material. To evaluate the above factors, the authors selected a tubular product (as shown in Fig. 1) made from Al-Cu-Mg-Mn alloy using the local upsetting technology. Currently, the above part is made using a machining method with a tensile strength, σ_b, of 420–430 MPa and a hardness $HV_{0.05}$ of 86.2. To improve the mechanical properties to ensure that the part meets the requirements, the pressure machining method has been used.

This tubular part is made by cutting from a Φ75 × Φ40 × 190 mm tubular billet with a material efficiency reaching 31.58% a very low efficiency that wastes materials and pushes up production costs. Eight tasks are used to fabricate the part, namely, cutting, rough turning, face trimming, inner rough turning, inner cylindrical turning, thread turning, outer-surface

turning, and aging the tube surface. Furthermore, if a pressure deformation machining method is used, the ratio of the final pipe thickness S_1 at the forming part to the original pipe thickness S_0 will determine the number of forming steps. It is necessary to define the critical ratio S_1/S_0 that ensures that the parts will not be destabilized. This study performs numerical simulations to determine the critical ratio, and the results are verified experimentally while evaluating the metal structure and properties of the material Al-Cu-Mg-Mn alloy before and after deformation.

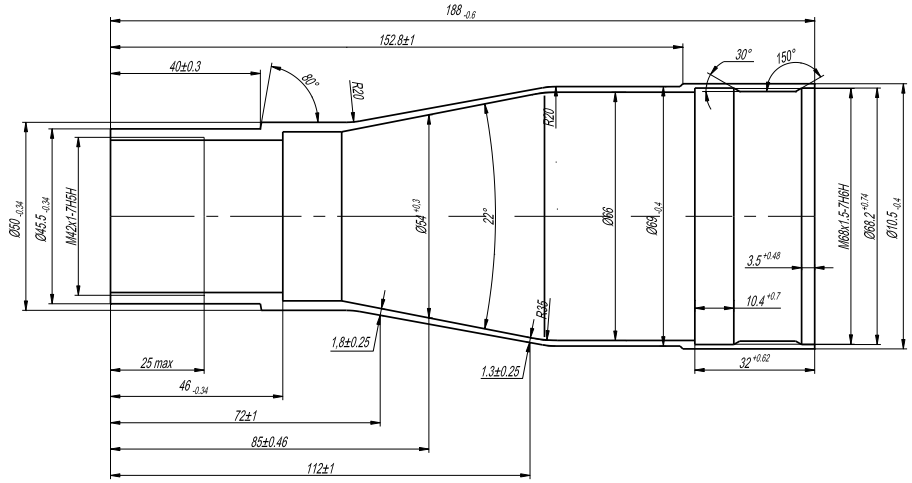

Fig. 1 Technical drawing of a tabular workpiece

MATERIAL AND METHODS

Experimental material

A tube of Al-Cu-Mg-Mn alloy (named D16 alloy) in its initial state (as-delivered) had a standard chemical composition (Al-4.4Cu-1.4Mg-0.7Mn, wt.%) with a diameter of Φ75 × Φ65 × 185 mm; it was heterogeneous, coarse-grained, and had low hardness values, of which the average was $HV_{0,05}$ = 86.2. Table 1 shows the mechanical properties of Al-Cu-Mg-Mn alloy.

Table 1 Mechanical properties of Al-Cu-Mg-Mn alloy

Elastic modulus E (10^{-5})	Tensile strength σ_b (MPa)	Yield stress σ_c (MPa)	Hardness, $HV_{0,05}$ for Al-Cu-Mg-Mn alloy
0.72	390–420	255	86.2

The material parameters and deformation curve of Al-Cu-Mg-Mn alloy are included in the material model [25]. The coefficient of friction when pressing is 0.1, and the displacement of the punch is 25 mm. After performing the simulation, the stress distribution, strain, force diagram, and mesh deformation corresponding to the case of the most suitable critical thickness ratio S_1/S_0 were obtained.

Estimation of critical thickness ratio by numerical simulation

The critical thickness ratio S_1/S_0 is determined by simulation. The initial workpiece thickness, S_0, is 4.08 mm.

The simulation model is built according to the technology diagram shown in Fig. 2, including the billet, punch, ring, and pilot punch (positioning pestle) with sizes designed to create the product shown in Fig. 1. The boundary conditions are indicated; for example, the coefficient of friction when pressing is 0.1, and the displacement of the punch is 25 mm.

Experimental process

The tubular workpiece was made by machining pressure from a tube billet with a size of Φ75 × Φ65 × 185 mm. The material-use efficiency is 56.53%. The number of tasks was reduced, and the remaining ones included cutting, narrowing of the head (step 1), renarrowing of the head (step 2), annealing, trimming, upsetting, aging, turning, hole turning, and threading the M42x1.

Based on the simulation results, a stamping step is used to ensure a critical thickness ratio of S_1/S_0, which is the most feasible for the technical requirements of the part. The cold upsetting deformation area located in region II serves to increase the size of the workpiece, as shown in Fig. .

+ Region I (billet storage area) provides materials for a local upsetting process in a closed die located in region II. The height, Δh, of the upsetting workpiece is 9 mm; the workpiece height is reduced in region I, but the cross section increases in region II.
+ Region II (upsetting deformation): Metal is filled by upsetting in the mold cavity, increasing the thickness from 4.08 to 5.87 mm.
+ Region III (without deformation): The shape of this part is kept intact during deformation. Hence, to prevent this area from deforming, a positioning and clamping mechanism for which the shape of the workpiece does not change under the axial compression effect from region II should be used. Additionally, the forming process is performed on a 315 ton hydraulic press machine.

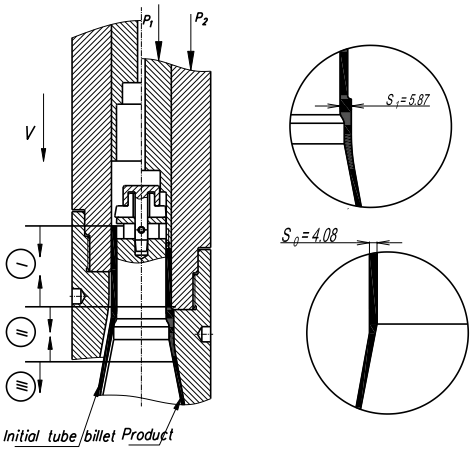

Fig. 2 Cold upsetting forming region

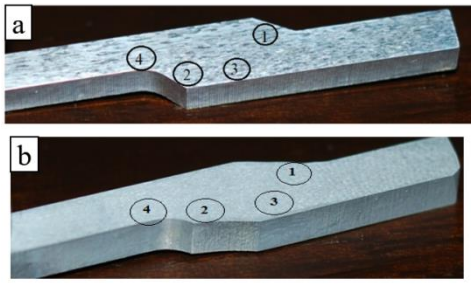

Fig. 3 Microstructure observation positions: (a) the sample is machined; (b) the sample is deformed by upsetting

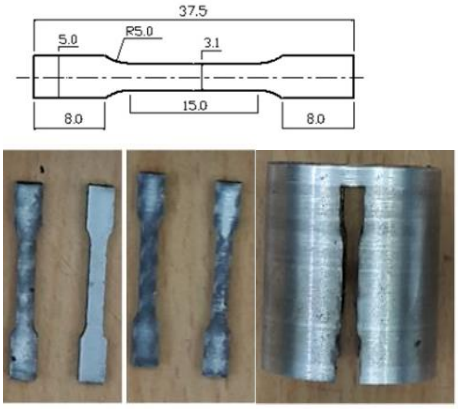

Fig. 4 Tensile testing experimental samples

After fabrication, the workpiece is cut in half to measure the part's diameter and thickness dimensions. These dimensions have the same values as shown in the part's technical drawing. In the upsetting position, the direction of the metal grain is observed to run along the part, and no folding defects appear.
To consider the appearance of the folding defects and microstructure investigated in the deformation area when using a cold upsetting process, the experimental sample was cut and enlarged at locations 1, 2, 3, and 4, as shown in Fig. . The investigated locations correspond to the positions of deformed region II. Hence, in the deformation region, an investigation was conducted at different positions to evaluate the uniformity of the metal microstructure. Additionally, an observation of the workpiece's cross section in the upsetting area shows that no folding defects appear. The metal fiber is compressed, swollen, and used to gradually fill the mold cavity. No metal flows in different directions, which would lead to creases in the substrate material.
To compare the tensile strengths of the samples, several experiments were conducted using the tensile testing process in region II before and after deformation on the tensile testing machine MTS–809. Figure 4 shows the images of the testing samples used in the experiments. The fabricated samples and the tensile testing procedure are performed as specified. Furthermore, to evaluate the stiffness of the samples after deformation, measurements were made on the HUATEC MHV1000 hardness-measuring device at three points on the deformation zone of the investigated sample. The calculation result is the average value of the measurements; it is used to evaluate the stiffness of the shaped parts.

RESULTS AND DISCUSSION

As shown in Table 2, the simulation results of the critical thickness ratio S_1/S_0 are obtained.

Table 2 Thickness and critical thickness ratio of the workpiece

S_0	S_1	S_1/S_0
4.08	5.87	1.44

This critical value ensures the ability to fill the part in the closed die. Without the stress exceeding the limit value, the filling part is free of defects. The maximum compressive stress on the part is −371 MPa, smaller than the value of the breaking stress.

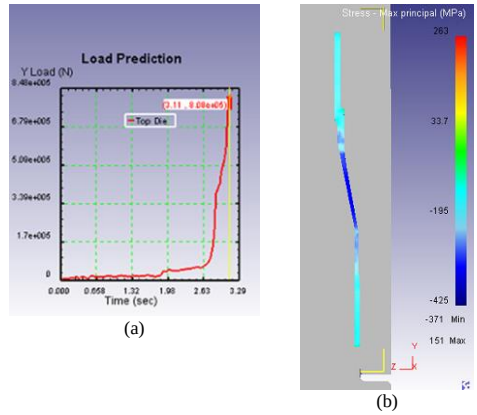

(a) (b)

Fig. 5 Distribution diagram of upsetting force (a) and stress state (b) on the workpiece

Investigation of the microscopic organization of the deformation area after upsetting

At the survey locations, the sample was magnified 50 and 200 times, respectively. Fig. 6 shows the microstructure of the material in region II, corresponding to four positions before the

upsetting deformation. The metallic structure observed at these points is almost the same. It can be seen that the organized metal of the tubular workpiece was produced by bar melting. The metal grains are elongated and oriented parallel to the tube's centerline. The layer metal structure distributed in the texture is the input metal structure for a melt-pressing process. The initial horizontal particle size ranges from 10 to 20 µm.

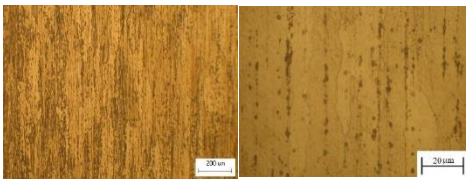

Fig. 6 Microstructure of the sample before the upsetting deformation in position 2

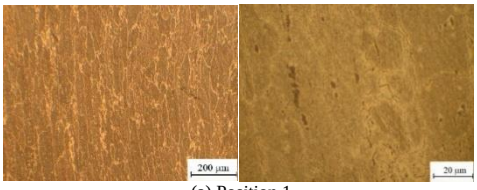

(a) Position 1

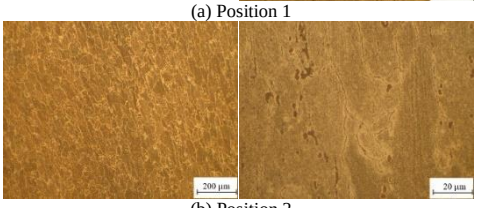

(b) Position 2

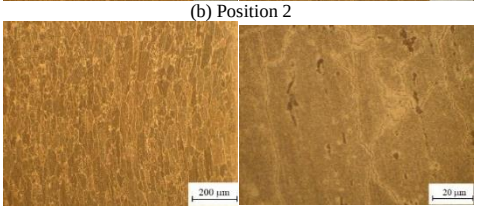

(c) Position 3

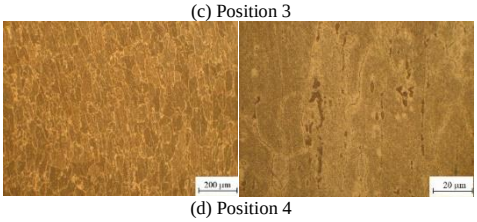

(d) Position 4

Fig. 7 Microstructure of the samples shaped by upsetting at different survey positions

Fig. shows the photos of the metal microstructures after the upsetting deformation, as taken at positions 1, 2, 3, and 4. It can be seen that at the positions of deformation (such as positions 2 and 3 in the upsetting metal area), the substrate's structure is in an alpha phase. Simultaneously, there exist scattered intermetallic phases in the metal.

- Position 1: Based on the dimension H = 46.96 mm (shown in Fig.), the metal grain is deformed in the axial direction, the grain boundaries are clear, and the intermetallic phases exist, scattering in the grain structure. The 200× magnified image shows the microscopic grain arrangement along the body of the part, forming a longitudinal fiber. There is not large deformation in zone I, but it moves into deformation zone II; thus, the grain direction remains the same as in the original material. The layered structure of the original material has been eliminated.
- Positions 2 and 3: The grain is deformed in the direction of curvature, and there exists a horizontal flow. The metal whirling in the direction of material flow is due to the tendency to fill in the corner positions of the mold, which greatly improves the material's mechanical properties. The particle density is tighter, although the particle size is insignificantly smaller, and the grains usually appear with sizes of about 5 to 10 µm. Because the metal is compressed, the metal grain no longer elongates but tends to be curved. The grain border is therefore clear, and there exist scattered intermetallic phases in the grain structure. Based on the 200× magnification image, one can clearly see that the grain tends to curl according to the upsetting device profile. Thus, this direction of curvature will create a part with superior tensile load capacity.
- Position 4: Since the metal is not deformed in this area, it only affects the direction of zone II, so the grain direction and grain form are the same as in the original material.

Compare the strength of the material in the upsetting strain zone with the original material

The samples for tensile test are separated from the formed part by upsetting and turning (Fig. 4) and they are stretched in the longitudinal direction of the tube or z-direction. The sample tensile testing results are shown on Z-axis stresses comparison graph, as shown in Fig. 8. There is a sudden kink in the Stress in Z-direction and strain plot for machining sample due to the low ductility of the machined sample, and no grain direction as in the case of deformed samples. During tensile testing, the uniform deformation occurs only for a short time or for several percent of elongation, then the sample is non-uniformly deformed and the necking appears. When necking occurs, the z-axis stress will decrease dramatically. After upsetting, the metal exhibits an increase in deformability and tensile strength, which is explained by grain deformation in the direction of curvature. Such a material construction helps the part to better withstand traction in both the radial and axial directions. The elongation of the original metal sample reaches a maximum of approximately 3.3%. The maximum achievable elongation of the sample after upsetting increases approximately three times and reaches 9%. A fine grain size will certainly improve the yield strength and stress relaxation resistance of the finished product.

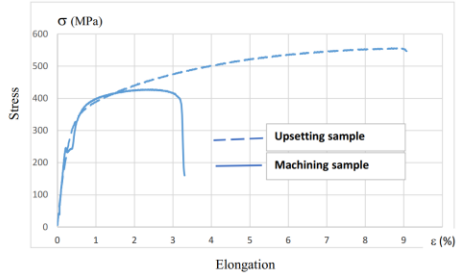

Fig. 8 Comparison of the tensile strengths of the sample formed using upsetting and the original sample

Comparison of the microscopic hardness of the material at the upsetting strain area with the original material

Table 3 presents the hardness evaluation ($HV_{0.05}$) results of the samples. After upsetting, the microscopic hardnesses measured at three points on the upsetting deformation area are 103.6, 104.2, and 103.9 HV, respectively. The average hardness value obtained is 103.9 HV. Hence, hardening significantly increases the microhardness to 103.9 $HV_{0.05}$.

Table 3 Mechanical properties of the Al-Cu-Mg-Mn alloy before and after upsetting

N^0	Condition	Tensile strength σ_b (MPa)	Hardness (HV)
1	Original material	427	86.2
2	After upsetting	556	103.9

CONCLUSION

The hollow parts with variable thickness and diameter can be fabricated using plastic deformation of material such as upsetting technology. However, the upsetting technology of tube or hollow billet needs to be carefully calculated using numerical simulation and experiments must be performed to take the advantages of plastic deformation process compared to machining technology.

The result of this study shows that the mechanical properties like hardness and tensile strength for the Al-Cu-Mg-Mn alloy have been improved by 20–30% by plastic deformation.

The application of an upsetting technology for hollow cylindrical parts with variable cross sections and diameters enables an increased thickness ratio of 1.44, that leads to material-use efficiency increasing of 56.53% compared with machining methods only about 31.58%.

The mechanical properties of materials after upsetting have improved, For example the tensile strength improved by 1.3 times from 427 to 556 MPa and the hardness HV0.05 in the strain area improved by 1.2 times from 86.2 to 103.9 HV.

The upsetting technology will be applied to manufacture the mechanical parts to reduce machining steps and improve productivity and economic efficiency.

ACKNOWLEDGEMENTS

The work was funded by the Hanoi University of Science and Technology (HUST) under project number T2020-PC-202.

REFERENCES

1. A. Tuzun: *Analysis of tube upsetting*. Master thesis at Middle East Technical University, Metallurgical and Material Engineering Department of Middle East Technical University, 2004.
2. H. Roven, M. Liu, M. Murashkin, R. Valiev, A. Kilmametov, T. Ungár, L. Balogh: Materials Science Forum, 604-605, 2009, 179-185. https://doi.org/10.4028/www.scientific.net/MSF.604-605.179.
3. R. Z. Valiev, I. V. Alexandrov: Nanostructured Materials, 12(1), 1999, 35-40. https://doi.org/10.1016/S0965-9773(99)00061-6.
4. C. Wang, F. Li, B. Chen, Z. Yuan, L. Hongya: Rare Metal Materials and Engineering, 41, 2012, 941–946. https://doi.org/10.1016/S1875-5372(12)60049-6.
5. Z. G. Chen, Z. Q. Zheng, D. F. Han: Materials Science Forum, 519-521, 2006, 1925-1930. https://doi.org/10.4028/www.scientific.net/MSF.519-521.1925.
6. T. Kvackaj, J. Bidulska, M. Fujda, R. Kocisko, I. Pokorny, O. Milkovic: Materials Science Forum, 633-634, 2010, 273-302. https://doi.org/10.4028/www.scientific.net/MSF.633-634.273.
7. J. Bidulská, R. Bidulský, M. Actis Grande, T. Kvačkaj: Materials (Basel), 12(22), 2019, 3724. https://doi.org/10.3390/ma12223724.
8. R. R. Ilyasov, E. V. Avtokratova, S. V. Krymskiy, O. S. Sitdikov, M. V. Markushev: IOP Conference Series: Materials Science and Engineering, 447, 2018, 012047. https://doi.org/10.1088/1757-899x/447/1/012047.
9. O. Paitova, E. Bobruk, M. Skotnikova, J. Wu: Key Engineering Materials, 822, 2019, 101-108. https://doi.org/10.4028/www.scientific.net/KEM.822.101.
10. I. Polozov, A. Popovich, V. Sufiiarov, E. Borisov: Key Engineering Materials, 651-653, 2015, 665-670. https://doi.org/10.4028/www.scientific.net/KEM.651-653.665.
11. T. S. Kol'tsova, F. M. Shakhov, A. A. Voznyakovskii, A. I. Lyashkov, O. V. Tolochko, A. G. Nasibulin, A. I. Rudskoi, V. G. Mikhailov: Technical Physics, 59(11), 2014, 1626-1630. https://doi.org/10.1134/S1063784214110139.
12. J. Liu, T. Liu, H. Yuan, X. Shi, Z. Wang: Materials Transactions, 51, 2010, 341-346. https://doi.org/10.2320/matertrans.M2009288.
13. M. B. Hanamantraygouda, B. P. Shivakumar, P. N. Siddappa, L. Sampathkumar, L. Prashanth: IOP Conference Series: Materials Science and Engineering, 310, 2018, 012072. https://doi.org/10.1088/1757-899x/310/1/012072.
14. L. Shen, J. Zhou, X. Ma, X. Z. Lu, J. W. Tu, X. Shang, F. Gao and J. S. Zhang: Journal of Materials Processing Technology, 239, 2017, 147-159. https://doi.org/10.1016/j.jmatprotec.2016.08.020.
15. A.R. Mishetyan, G.A. Filippov, Yu.D. Morozov, O.N. Chevskaya: Problems of ferrous metallurgy and materials science, 2, 2011, 12-19.
16. D. Tang, X. Fan, W. Fang, D. Li, Y. Peng, H. Wang: Materials Characterization, 142, 2018, 449-457. https://doi.org/10.1016/j.matchar.2018.06.010.
17. M. Motallebi Savarabadi, G. Faraji, M. Eftekhari: Metals and Materials International, 2019. https://doi.org/10.1007/s12540-019-00525-7.
18. M. Singh, D. Chauhan, M. Gupta, A. Diwedi: Journal of Material Science & Engineering, 04, 2015. https://doi.org/10.4172/2169-0022.1000202.
19. A. Akkurt: Engineering Science and Technology, an International Journal, 18(3), 2015, 303-308. https://doi.org/10.1016/j.jestch.2014.07.004.
20. A. Handbook: ASM Handbook Committee, 16, 1989, 761-804.
21. [04.17.2014], https://www.productionmachining.com/articles/how-metallurgical-structure-affects-the-machinability-of-aluminum.
22. O. N. Cora: *Friction analysis in cold forging*, The graduate school of natural and applied sciences of Middle East Technical University, Middle East Technical University, 2004.
23. P. Gao, X. Yan, M. Fei, M. Zhan, Y. Li: The International Journal of Advanced Manufacturing Technology, 104(1), 2019, 1603-1612. https://doi.org/10.1007/s00170-019-04145-8.
24. J.P.M. Poursina: AIP Conference Proceedings, 712, 2004, 486-491. https://doi.org/10.1063/1.1766572
25. S.M.S.A.B. Abdullah, Z. Samad, H.M.T. Khaleed, N.A. Aziz: Scientific Research and Essays, 7(15), 2012, 1630-1638.

ACTA METALLURGICA SLOVACA
2021, VOL. 27, NO. 2, 77-86

RESEARCH PAPER

NUMERICAL AND EXPERIMENTAL STUDY OF CERAMIC/STEEL COMPOSITE FOR STRUCTURAL APPLICATIONS

Olawale Monsur Sanusi[1,2]*, Olatunde Ajani Oyelaran[2], Mounir Methia[1,3], Anurag Dubey[1], Adeolu Adesoji Adediran[4]

[1]INSA CVL, Univ. Tours, Univ. Orléans, LaMé, 3 rue de la Chocolaterie, BP 3410, 41034 Blois Cedex, France
[2]Department of Mechanical Engineering, Federal University Oye-Ekiti, Ekiti State, Nigeria
[3]Laboratoire de Mécanique, Matériaux et Energétique (L2ME), Faculté de Technologie, Université de Bejaia, 06000 Bejaia, Algeria
[4]Department of Mechanical Engineering, Landmark University, Omu Aran, Kwara State, Nigeria

*Corresponding author: olawalem.sanusi@fuoye.edu.ng, tel.: +33602120550, LaMé / INSA Centre Val de Loire, 41000, Blois, France

Received: 06.01.2021
Accepted: 11.03.2021

ABSTRACT

The terminal ballistics is the study of science that deals with the interaction involved in two impacting bodies. Identifying the optimum thickness ratio of layered composites that offers efficient resist to impending projectile is a great challenge in ballistics engineering. This research focused on the high-impact resistance of layered composite comprising of alumina ceramic and armour steel using numerical approach (Abaqus) in determining the composite thickness ratio. The composite was designed to have ceramic as the facial plate with armour steel as its backing plate. From the numerical study, the ceramic thickness was varied (6, 8, 10, 12 mm) while keeping the thickness of backing steel constant (7 mm). The projectile, 7.62 mm armour-piercing (AP), was set with a velocity of 838 m/s and made to impact the different ceramic–steel composite target configurations at zero obliquity. The study captured fracture processes of the ceramic, the deformation of projectile, and backing steel. An effective optimum thickness ratio of 1.4 (ceramic:steel; 10/7) for the ceramic/steel components with less deformation of the backing steel was found. Thereafter, the result of the numerical study was validated by experimental ballistic investigation of the determined optimum ceramic/steel ratio. The experiment corroborated the simulation results as the alumina ceramic provided efficient protection to armour steel component after a severe interaction with the impacting projectile.

Keywords: ceramics; steel; composites; armour; terminal ballistics

INTRODUCTION

Armour structure provides ballistic defeat to imminent projectiles or blast fragments. Traditionally, ballistic protection is primarily made of high hardness steel owing to its high strength and rigidity. However, most systems requiring ballistic protection are mobile (military vehicle, tank, aircraft and/or military/security personnel). Thus, thickness of the protective materials, related to weight, becomes a critical issue in armour design. Two, it is becoming easy to defeat strong steel via armour piecing (AP) projectile that causes a major setback for conventional steel. Understanding this weakness, ammunition designers are replacing standard metallic projectile nose with toughened-ceramic nose in an attempt to increase projectile penetration capability in protection targets [1]. These led to search for high-performance but lightweight and low-cost protective materials (for personnel and vehicles) to improve manoeuvrability, survivability and reduce injury when subject to threats including blast [2,3]. Thus, enhanced mobility, high strength to weight ratio with the high impact resistance are the primary concept of lightweight armour design [4].

Consequently, ceramic-steel composites have been introduced to offer the solution for efficient lightweight armours [5-10]. Precisely, low density, high hardness, high rigidity and compression strength of ceramics [1,5] makes it popular and suitable for armour systems; including aircraft structures, personal armour and military vehicles [11-15]. Several ceramic materials are used for facial ballistic armours: alumina [16-18], boron carbide (B4C) [19], silicon carbide (SiC) [20]. The backing steel provides structural integrity as ceramics lack strength under tension [21].

The experimental research requires many samples to be prepared and evaluated ballistically against several projectiles at varying conditions. This consumes much time, cost and often lead to abandoning of quite a few scenarios. So, to predict various cases of material behaviour, modelling and simulation are adopted through discrete numerical methods (e.g. finite element method, FEM or smoothed particle hydrodynamics, SPH) [22]. Besides, the high speed involved in terminal ballistics makes it challenging to visualize and analyze projectile-target interaction damage, but numerical simulation permits such studies [23].

Fawaz et al. [24] used finite element code LS-DYNA in simulating the normal and oblique ballistic impact of projectile against alumina ceramic plate and carbon/epoxy composite at low velocity (315 m/s). They found that the bullet erosion in the oblique impact was slightly more than that of normal impact, while the distributions of global kinetic, internal and total energy versus time were similar for normal and oblique impacts. Akella [7] studied the layering effect of ceramic

armour in an effort to improving toughness property over aluminium-alloy backing using numerical methods of Autodyn. A monolithic ceramic or layers of ceramic at a given thickness were studied over a constant thickness of the backing. The simulated impact velocity was 800 m/s using 5 mm diameter steel projectile. It was observed that increasing the layers lowered the penetration resistance of ceramic but with better multi-hit capacity when compared with monolithic ceramic of the same strength. It was reported that the reduction in layer thickness leads to increase in the system strength.
Alumina ceramic had been previously prepared by sintering process from purified corundum [25, 26]. This study strives to determine the ballistic influence of the ceramic on ceramic/steel composite as well as finding the optimum thickness of the ceramic required to make an applied component of ceramic/steel armour system for structural ballistic applications.

2. MODEL AND MATERIAL DESCRIPTION

The simulations models were developed and carried out using the Abaqus/Explicit 6.12 simulation software in a computer equipped with Intel core i5 CPU at 2.20 GHz [27].

2.1 Creation of the models
2.1.1 Projectile

The conical-point cylindrical projectile was modelled as 7.62 mm in diameter using the revolving tool after creating the 2D profile with a length of 28.1 mm; following NIJ Standard 0108.01 (1985) [28]. The revolve command was set at 90° to produce a quarter model of the projectile (symmetry) as shown in **Fig. 1(a)**.

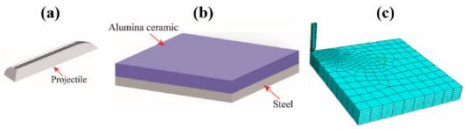

Fig. 1 Model and finite element representation of impacted alumina ceramic/steel composite amour target (a) projectile (b) laminate (c) projectile-laminate finite element assembly.

2.1.2 Components (layers) of the armour system

The rectangular armour target has its frontal plate as alumina ceramic with varying thickness (6, 8, 10 and 12 mm), and a 7 mm steel backing. These plates were created by extrusion tool of ABAQUS after creating 2-D square profiles (50 X 50 mm), **Fig. 1b**. Then the parts created separately were imported into assembly environment of the software. Mates command were applied to the components to create the parts assembly. The assembled meshed model in the ABAQUS interface is as shown in **Fig. 1c**.

2.2 Models definition and constraints

Two different material models were used for this simulation. The Johnson-Cook (JC) constitutive model was used to predict the material behaviour of the backing steel plate and projectile. JC model is commonly used to predict the material response of metals: armour steel, aluminium alloy and projectile material [28]. The model is supported by most finite element code, and the model constitutive dynamic flow stress (σ_f) relation is expressed in Eq. (1) [29-32].

$$\sigma_f = \left\{A + B\left(\varepsilon_{ef}^{p}\right)^{N}\right\}\left[1 + CIn\frac{\dot{\varepsilon}_{ef}^{p}}{\dot{\varepsilon}_o}\right]\left[1 - \left(\frac{T-T_o}{T_m-T_o}\right)^{M}\right] \quad (1.)$$

Where, $\dot{\varepsilon}_o$ is the equivalent plastic strain rate, $\dot{\varepsilon}_{ef}^{p}$ is the effective plastic strain rate, ε_{ef}^{p} is the effective plastic strain. T_o and T_m are reference and melting temperature, respectively. A, B, C, N, M are the material property constants required for the material model.
The JC model is also incorporated with a failure model which is related to von Mises stress ($\bar{\sigma}$), the three normal stresses average (σ^m), temperature, T and $\dot{\varepsilon}_{ef}^{p}$. The expressions for the damage, D is given in Equation 2 - 3, according to Lamberts [32].

$$D = \left[\frac{\varepsilon_{ef}^{p}}{\dot{\varepsilon}_o}\right] \quad (2.)$$

$$\dot{\varepsilon}_o = \left\{D_1 + D_2 exp\left(D_3\frac{\sigma^m}{\bar{\sigma}}\right)\right\}\left[1 + D_4 In\frac{\dot{\varepsilon}_{ef}^{p}}{\dot{\varepsilon}_o}\right]\left[1 + D_5\frac{T-T_o}{T_m-T_o}\right] \quad (3.)$$

Where D_1, D_2, D_3, D_4 and D_5 are material parameters. Johnson Holmquist (JH-2) material models was implemented into ABAQUS as user-defined material model in predicting the material behaviour of the alumina. JH-2 predicts mechanical characteristics of brittle materials (e.g. rock, ceramics, concrete) subjected to excessive loading [29]. The key features of the model comprise pressure-dependent strength, damage and fracture, substantial strength after fracture, bulking and strain rate effects [33, 34]. According to Kędzierski et al. and Ming and Pantalé [29, 35], the normalized equivalent stress, σ^*, is given in Eq (4),

$$\sigma^* = \sigma_i^* - D\left(\sigma_i^* - \sigma_f^*\right) \quad (4.)$$

Where, σ_i^* is the normalized intact equivalent stress; σ_f^* is the normalized fracture strength stress and D is the damage variable; ($0 \leq D \leq 1$). Eqs (5) and (6) give the expressions for the normalized intact equivalent stress and normalized fracture equivalent stress, respectively given as

$$\sigma_i^* = A(P^* + T^*)^N\left(1 + Cln(\dot{\epsilon}^*)\right) \quad (5.)$$

$$\sigma_f^* = B(P^*)^M\left(1 + Cln(\dot{\epsilon}^*)\right) \quad (6.)$$

A, *B*, *C*, *M* and *N* are material constants; P^* is the normalized pressure; $\dot{\epsilon}^*$ is the normalized strain-rate; with energy conversion factor (β) and equation of state parameters (K_1, K_2, K_3).
The material property constants required for the models were sourced from literature [7, 24, 29, 33, 34] and presented in **Tables 1** and **2**. The constrained tied with Surface-To-Surface Contact element was selected to connect the ceramic and backing plate. The boundary or contact procedures between the projectile and the armour system were defined with Contact-Eroding-Surface-To-Surface. The nodes that make up the projectiles mesh were allocated an initial velocity of 838m/s in accordance to (NIJ Standard 0108.01, 1985). The projectile was impacted normally on to the different ceramic–steel composite target configurations.

3. NUMERICAL SIMULATION RESULTS
3.1 Projectile/target interaction

For this simulation, the evaluating parameter was the optimum thickness of the ceramic on armour system in order to avoid any complete penetration of the target at the limit velocity of the projectile, as well as saving both space and weight for a

lightweight armour system. Therefore, various target configurations are modelled and simulated by varying the ceramic thickness (6, 8, 10, 12 mm) over a constant 7 mm backing armour steel.

Table 1 JC model parameters for projectile core and armour steel

Property	Unit	Projectile	Backing steel
Density	g/cm^3	7.85	7.85
Young's modulus	GPa	202	202
Poisson ratio		0.3	0.3
JC Constants:			
A	GPa	1.576	0.849
B	GPa	2.906	1.39
N		0.1172	0.0923
C		0.00541	0.00541
M		0.87	0.87
Melting temperature	K	1800	1800
Transition temperature	K	293	293
Referential strain rate	1/s	1	1
Failure Constants:			
D_1		0.0356	-0.4
D_2		0.0826	1.5
D_3		-2.5	-0.5
D_4		0	0.002
D_5		0	0.61

Table 2 JH-2 model parameters for alumina ceramic

Property	Unit	Alumina Ceramic
Density	kg/m^3	3700
Shear modulus	GPa	90.16
JH-2 Constants:		
A		0.93
B		0.31
N		0.6
C		0
M		0.6
Referential strain rate	1/s	1
JH-2 Failure:		
D_1		0.005
D_2		1
EOS Constants:		
K_1	Pa	1.3095 E11
K_2	Pa	0
K_3	Pa	0
Beta, β		1

3.1.1 6mm-ceramic/7mm-backing steel (6-7 Armour System)

The computational impact process for the 6-7 armour system at different time interval is shown in **Fig. 2(a-f)**. It illustrates the position of the projectile in the impact process at different times, according to the von Mises stress. By the impact of the projectile, fractures are initiated instantaneously in the facial ceramic plate around the region of projectile impact periphery. The fractures occur in 2 μs of the total 40 μs of projectile-armour target interaction which is ascribed to the extreme compressive stress at that point. The ceramic plate is observed to be fully eroded by the projectile in **Fig. 2(f-h)**; all depict the same final stage of erosion. **Fig. 2(g)** only carries the meshing feature, while the worn projectile was hidden (removed) in **Fig. 2(h)**, from the impact site, in order to vividly reveal the destruction state at 40 μs. A conical crushed ceramic region remains in front of the deformed projectile while the fractures reach the interface of ceramic-metal composite. The result is in agreement with the literature [24]. At the interface, the projectile is seen to be squashed, stopped but caused severe bulging on the armour steel backing.

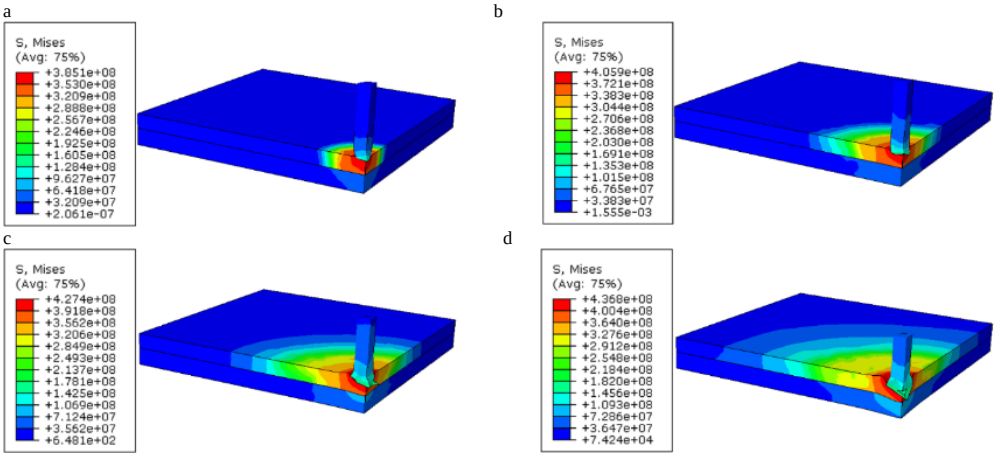

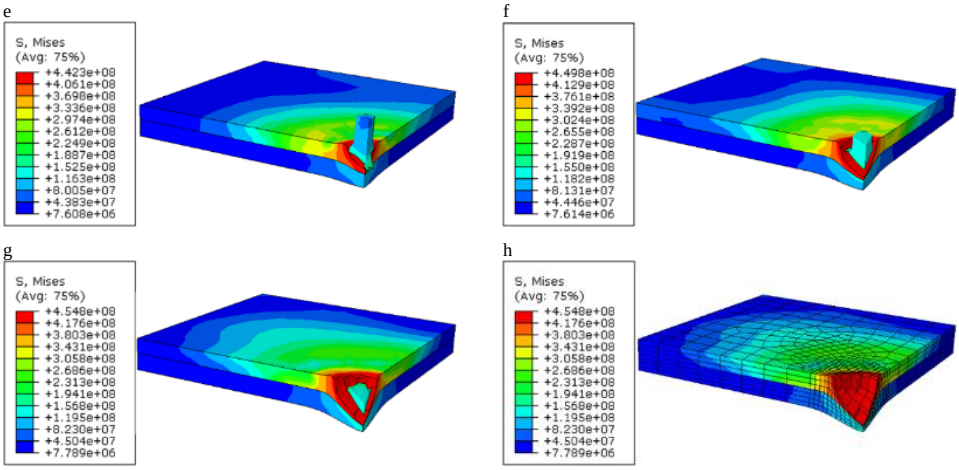

Fig. 2 Impact processes for 6mm ceramics/7mm backing steel composite

3.1.2 8 mm-ceramics/7mm-backing steel (8-7 Armour System)

A similar occurrence is observed when the configuration with 8mm-ceramics/7mm-backing steel plate was impacted with the same projectile; see **Fig. 3**. The gradual erosion of the projectile and the ceramic commenced from **Fig. 3(a-f)**, while tensile deformation of the backing plate without complete perforation was also observed but is less than 6-7 armour system.

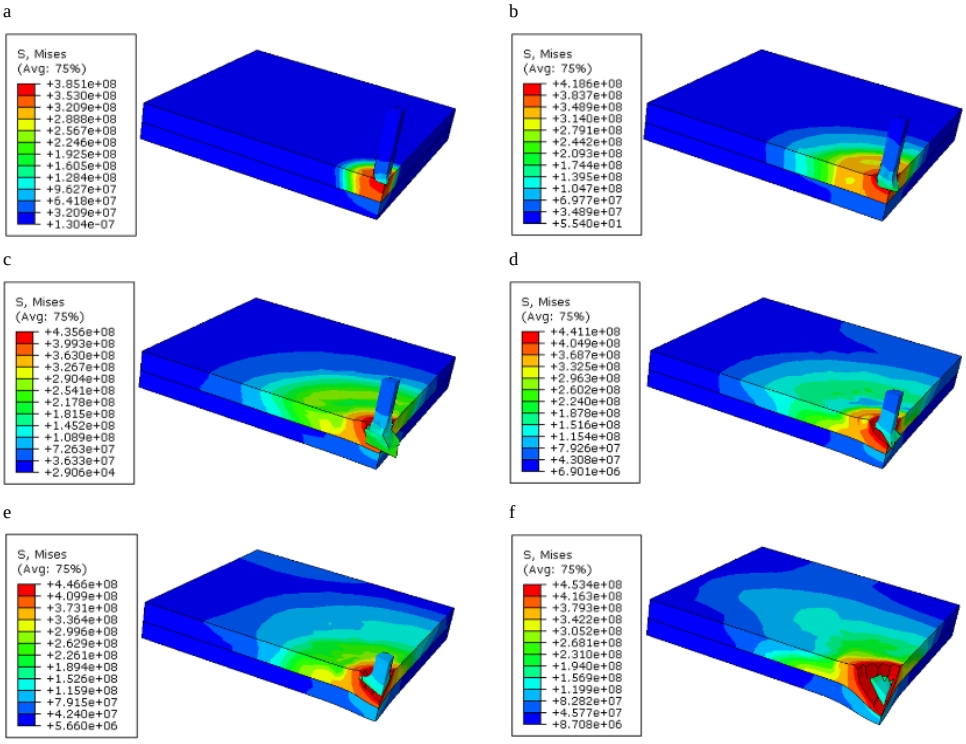

g

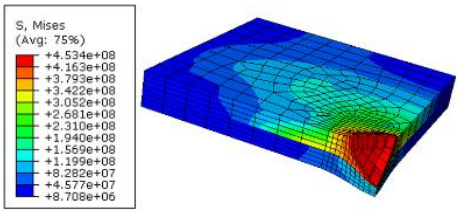

Fig. 3 Impact processes for 8mm ceramics/7mm backing steel composite

3.1.3 10 mm-ceramics/7mm-backing steel (10-7 Armour System)

The gradual erosion of the projectile and the ceramic commenced from **Fig. 4(a)** through to **Fig. 4(g)**, while tensile deformation of the backing plate without perforation was observed. The worn projectile was hidden (**Fig. 4(f** and **g)**) from the impact site in order to reveal the destruction level. Interestingly, 10-7 armour system, in comparison with 6-7 and 8-7 armour systems (**Table 3** and **Fig. 6**), is observed to leave less deformation or stress on the backing after the projectile-ceramic mass erosion. Residue thickness of the compressed fractured ceramic layer is also visible after the impact phenomenon; **Fig. 4(e** and **g)**.

a

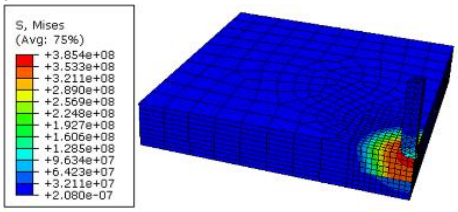

b

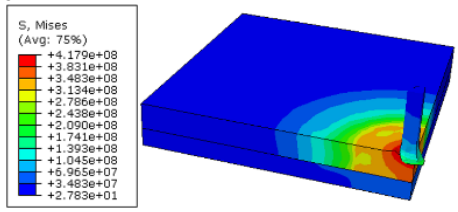

c

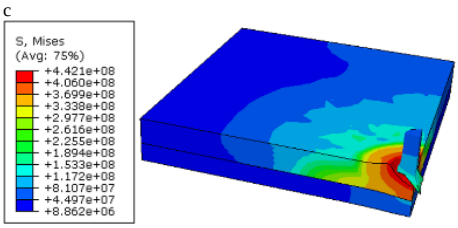

d

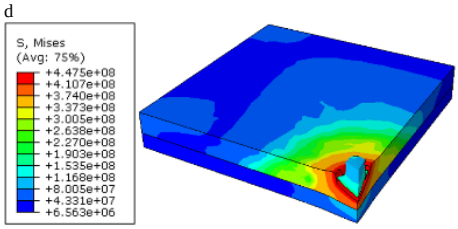

e

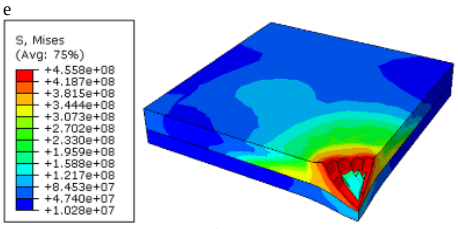

f

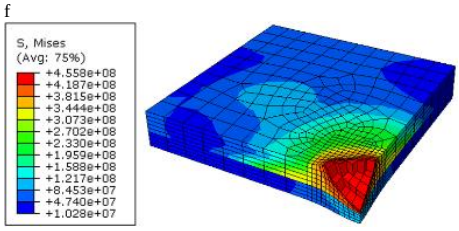

Fig. 4 Impact processes for 10mm ceramics/7mm backing steel composite

3.1.4 12 mm-ceramics/7mm-backing steel (12-7 Armour System)

Similarly, on increasing the ceramic thickness to 12 mm over the same thickness of metal backing, the projectile penetration phenomenon was the same with low bulging of the backing steel, **Fig. 5**. The erosion of the projectile and ceramic commenced from **Fig. 5(a-f)**. The worn projectile was hidden (removed), in **Fig. 5(f)**. The 12-7 configuration, in comparison with 10-7 armour systems (**Table 3**), is also observed to leave less deformation or tensile stress on the backing after the projectile-ceramic mass erosion. In comparing with 10-7 system, higher residue thickness of the fractured ceramic layer is visible after the impact phenomenon, **Fig. 5(f)**.

At various stages, **Fig. 2 - 5** have revealed the resulting contours of damage during the impact processes. The damages were initiated at the instance of affecting points, followed with the fracture front growing outwards, generally, in the radial direction. It was also appreciated that the impact generated compression on the armour laminate systems and this travelled (across the laminates) considerably faster than the damage

fronts. Usually, at the second stage of the penetration phase of the projectile, the compression waves were always observed to have travelled through the thickness of the ceramic and the metal composite. The metallic backing experienced lesser compression as it is seen from the simulation result that the backing has the next deep blue colouration to the original deep blue colour of the backing plate. As reported by Cronin et al. [36] that used LS-DYNA tool for simulating impact on ceramic material, the wave was reflected at the free surface bringing about a tensile wave with sufficient pressure to initiate tensile or spall failure of the ceramic component. The penetration of the projectile through the target materials led to erosion and massive change of the projectile shape. In addition, the deformed bullet left crater of higher diameter than the projectile, which is in agreement with the works of Hub and Kneys [37] and Şenyilmaz et al. [23]. The deformation on the backing steel, as the ceramic get thicker, was observed to reduce, probably due to energy released from the fractured ceramic particles [38].

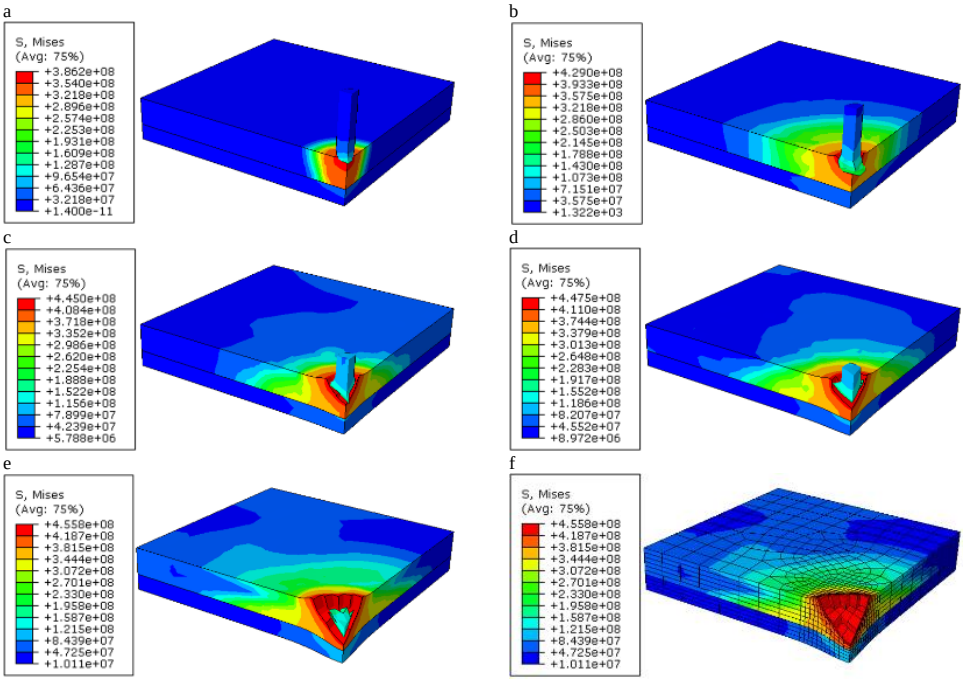

Fig. 5 Impact processes for 12mm ceramics/7mm backing steel composite

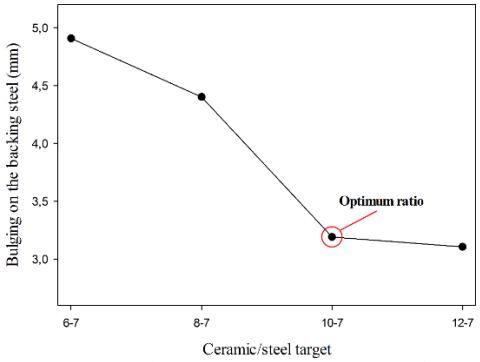

Fig. 6 Bulging left on the backing armour steel after the fracture of the facial ceramic on the different ceramic/steel composite configurations

Table 3 shows the final stages of the different simulated configurations in order to compare the deformation levels. **Fig. 6** depicts that the level of bulging left on the backing steel reduced with increase in ceramic thickness until an optimal ceramic thickness 10 mm is attained. Beyond this thickness (ceramic:steel = 10:7), increase in the ceramic thickness insignificantly influenced the ballistic resistance of the target system against 7.62 mm AP projectile. Therefore, the 10/7 armour assembly was considered to be the optimum system which could save space and weight in the composite armour assembly. Hence, the composite was selected and processed for experimental validation in section 4. From the numerical simulation result, it is concluded that the optimum erosion of 7.62 mm projectile could be achieved with a composite armour system comprising of 10 mm thick alumina ceramic on the steel plate.

3.2 Deformation energy history

The global energy history plots generated during the impact process for 10^{-7} armour system is presented in **Fig. 7**. It was observed that the kinetic energy (**Fig. 7a**) gradually reduced as the projectile penetrated the armour. In contrast, the system internal energy was observed to have increased, which agrees with literature [24, 39]. The dissipation of kinetic energy from 1.4 x 10^3 KJ to approximately zero in 40 µs resulted from deceleration on the velocity of the projectile, mass erosion of both the projectile and the armour system and the heat

losses associated with the impact phenomenon. The projectile kinetic energy is transferred to the armour composite system after impact. Hence, the internal energy, at a lower rate, increased from zero to its peak of about 900 KJ at 40 µs, **Fig. 7b**. The difference in the energy rate caused the total energy of the system to increase with decrease in kinetic energy, **Fig. 7c**. KE is computed by summation of 0.5 (nodal mass X nodal velocity^2) for both the nodes of projectile and the target. When this node-velocity comes to zero, the projectile comes to a complete rest.

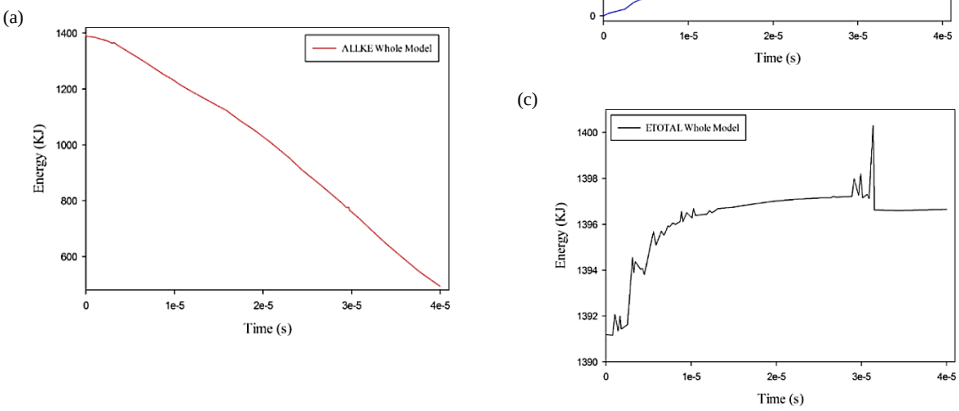

Fig. 7 Computed global energy (kJ) against time (µs) (a) kinetic energy (b) internal energy (c) total energy

Table 3 Comparison of last stages of impact simulation in armour assembly configurations

Armour configuration	Free edge laminate with projectile	Meshed laminate without projectile
6-7	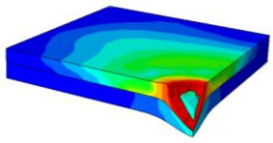	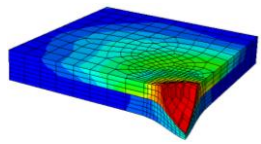
8-7	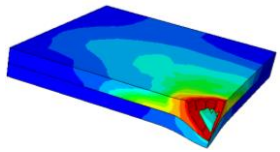	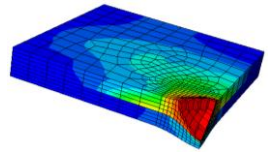
10-7	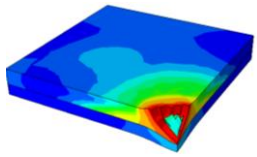	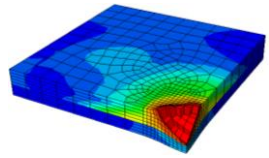
12-7	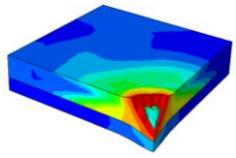	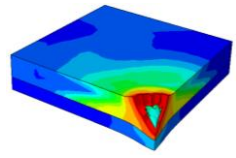

4. EXPERIMENTAL BALLISTIC STUDY

Normally, the ability of armour to stop bullets, ballistics effectiveness, is not determined by visual inspection but must be inferred from the results of live-firing test [40]. Sintered alumina ceramic (10 ×120 ×120 mm) prepared by sintering process [26] was used as the facial plate; and **Table 4** gives the physical properties of the sintered alumina (AC-86.6). The ceramic was laminated onto 7×120×120 mm armour steel (donated by Defence Industries Corporation of Nigeria), **Fig. 8a**, using synthetic Araldlte® epoxy adhesive and then left to dry for 24 hr under 26 MPa. Thereafter, the glued plates were wrapped with transparent polypropylene to enhance the firmness, **Fig. 8b**. The prepared samples were first conditioned at 23 ^{o}C for 24 h [27,41,42]. Test was taken at normal obliquity, 15 m from the weapon muzzle with projectile velocity maintained at 838 ± 15 m/s. Light automatic rifle was used for firing 7.62×51 armour piercing projectile (AP).

Table 4 Mechanical properties of sintered ceramic

	ρ g/cm^3	CS MPa	FS MPa	E GPa	K_{IC} MPa.m$^{1/2}$	BHN
AC-86.6	3.45	1912	295	270	3.75	75

Note: CS-compressive strength, FS-flexural strength, E-Young's modulus, K_{IC}-Fracture toughness and BHN-hardness

4.1 Evaluating armour steel

The as-received armour steel was first solely hit with 7.62×51 mm AP. The result of the impact against the armour steel plate at 0° obliquity is depicted in **Fig. 9**. The plate was penetrated completely through rearward petalling mode of perforation failure. This was expected as the strongest steel could easily be defeated by AP projectile [3]. The plate slightly bent inward at the impact of the projectile, which induced high circumferential stress at the impact point, and the compressive wave propagated inward leading to the failure of the armour steel [43]. The reverse side of the armour plate showed minute ductile-hole enlargement deformation, which is comparable to literature [44]. This failure mode is typically observed in a high ductile metal in which the nose of the conical bullet concentrates stresses at the contact point and results in intense deformation of the crater axis [45, 46].

4.2 Composite: Laminate of alumina ceramic and armour steel

Fig. 10(a) depicts laminate of ceramic and armour steel after impact process. The compression at the point of impact caused the debonding of ceramic and failed by pulverization into several pieces, while the backing armour steel was intact after the projectile impact. The pulverization of the ceramic occurred after the formation of microcracks, which developed into comminuted zone, also referred to as Mescall zone [9]. The ceramic, supported by high strength armour steel, significantly interacted with the projectile and lowered its energy, which resulted in the protection of armour steel with less bulge on it, **Fig. 10(b)**. As similarly observed by Guo et al. [8], bi-layered structure of ceramic/metal showed better ballistic performance because the ceramic eroded the bullet through cracking while the metal absorbed the remnant projectile kinetic energy by its deformation. Thus, the experimental results agree with the numerical simulation that predicted the wearing of the projectile by the ceramic, while the backing steel was ultimately protected.

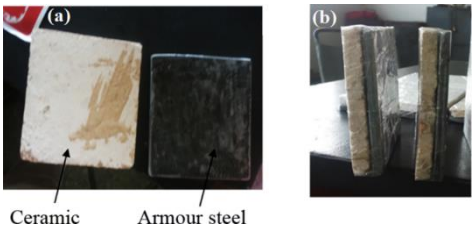

Fig. 8 (a) Sintered ceramic (left) and backing steel (right); (b) assembled composite

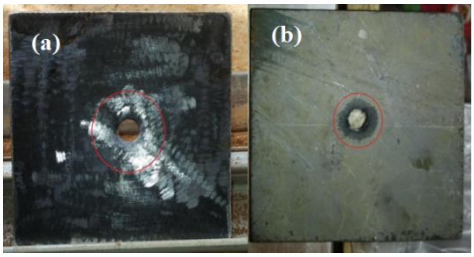

Fig. 9 Armour steel penetrated by 7.62 AP projectile (a) Front view (b) back view

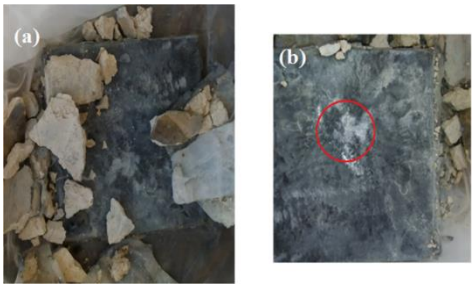

Fig. 10 (a) Fractured ceramic (b) Impression of the bullet impact on armour backing plate (red circle) after impact test

5. CONCLUSION

The numerical investigation of alumina ceramic/steel armour composite impacted by 7.62 mm AP projectile was studied to determine the optimal ceramic thickness required for providing high ballistic protection. The study captured the deformation of projectile, backing steel and fracture processes of the ceramic. The projectile was set with an initial velocity of 838m/s as per NIJ Standard and impacted on different ceramic–steel composite target configurations at zero obliquity. An optimum thickness ratio of 10:7 (ceramic/steel ratio) was found to offer the most effective composite armour system with the least trauma on the target steel. The simulation results depicted severe interaction of the projectile and the composite, wherein gradual erosion and retardation of the projectile by the ceramic component was achieved leaving armour steel plate protected. Finally, the experimental result corroborated the simulation result as the alumina ceramic provided efficient protection to armour steel component despite its failure. Therefore, the result of the finite element model was found useful in the improvement of lightweight armour laminate system design.

ACKNOWLEDGEMENT

The Defence Industries Corporation of Nigeria (DICON) is acknowledged for providing the armour steel plate and facilities for the ballistic experimental evaluation of the composites.

REFERENCES

1. D. Hu, J. Wang, L. Yin, Z. Chen, R. Yi, C. Lu: Experimental study on the penetration effect of ceramics composite projectile on ceramic/A3 steel compound targets, Def. Technol., 13, 2017, 281–287. https://doi.org/10.1016/j.dt.2017.05.011.
2. B. Quéfélec, M. Dartois: Ceramic-faced molded armor, in: *Lightweight Ballistic Composites*, Second ed., A. Bhatnagar (Ed.), Amsterdam: Woodhead Publishing, Elsevier Ltd., 2016, p. 369–391. https://doi.org/10.1016/B978-0-08-100406-7.00013-1.
3. J.R. Denzel: *Determination of shock properties of ceramic corbit 98*: 98% alumina, MSc Thesis Naval Postgraduate School (2010). https://apps.dtic.mil/dtic/tr/fulltext/u2/a524549.pdf.
4. V.C. Khan, A.K. Veldanda, G. Balaganesan, M.S. Sivakumar: Numerical study on multi layered target material subjected to impact loading, Lat. Am. J. Solids Struct., 15, 2018, 1–18. https://doi.org/10.1590/1679-78254156.
5. R. Yi, L. Yin, J. Wang, Z. Chen, D. Hu: Study on the performance of ceramic composite projectile penetrating into ceramic composite target, Def. Technol., 13, 2017, 295–299. https://doi.org/10.1016/j.dt.2017.05.009.
6. E. Medvedovski: Ballistic performance of armour ceramics: Influence of design and structure Part 2, Ceram. Int., 36, 2010, 2117–2127. https://doi.org/10.1016/j.ceramint.2010.05.022.
7. K. Akella: Studies for Improved Damage Tolerance of Ceramics Against Ballistic Impact Using Layers, Procedia Eng., 173, 2017, 244–250. https://doi.org/10.1016/j.proeng.2016.12.006.
8. X. Guo, X. Sun, X. Tian, G.J. Weng, Q.D. Ouyang, L.L. Zhu: Simulation of ballistic performance of a two-layered structure of nanostructured metal and ceramic, Compos. Struct., 157, 2016, 163–173. https://doi.org/10.1016/j.compstruct.2016.08.025.
9. L. Jinzhu, Z. Liansheng, H. Fenglei: Experiments and simulations of tungsten alloy rods penetrating into alumina ceramic/603 armor steel composite targets, Int. J. Impact Eng., 101, 2017, 1–8. https://doi.org/10.1016/j.ijimpeng.2016.09.009.
10. J.D. Clayton: Modeling and Simulation of Ballistic Penetration of Ceramic-Polymer-Metal Layered Systems, Math. Probl. Eng., 2015, 709498. https://doi.org/10.1155/2015/709498.
11. B. Tepeduzu, R. Karakuzu: Ballistic performance of ceramic/composite structures, Ceram. Int., 45, 2019, 1651–1660. https://doi.org/10.1016/j.ceramint.2018.10.042.
12. R. Chi, A. Serjouei, I. Sridhar, T.E.B. Geoffrey: Pre-stress effect on confined ceramic armor ballistic performance, Int. J. Impact Eng., 84, 2015, 159–170. https://doi.org/10.1016/j.ijimpeng.2015.05.011.
13. Q. Wang, Z. Chen, Z. Chen: Design and characteristics of hybrid composite armor subjected to projectile impact, Mater. Des., 46, 2013, 634–639. https://doi.org/10.1016/j.matdes.2012.10.052.
14. M.V. Silva, D. Stainer, H.A. Al-Qureshi, O.R.K. Montedo, D. Hotza: Alumina-Based Ceramics for Armor Application: Mechanical Characterization and Ballistic Testing, J. Ceram., 2014, 2014, 1–6. https://doi.org/10.1155/2014/618154.
15. D. Luo, Y. Wang, F. Wang, H. Cheng, Y. Zhu: Ballistic behavior of oblique ceramic composite structure against long-rod tungsten projectiles, Materials, 12, 2019, 1–13. https://doi.org/10.3390/ma12182946.
16. J. Venkatesan, M.A. Iqbal, V. Madhu: Ballistic Performance of Bilayer Alumina/Aluminium and Silicon Carbide/Aluminium Armours, Procedia Eng., 173, 2017, 671–678. https://doi.org/10.1016/j.proeng.2016.12.141.
17. A.Y. Badmos, D.G. Ivey: Characterization of structural alumina ceramics used in ballistic armour and wear applications, J. Mater. Sci., 36, 2001, 4995–5005. https://doi.org/10.1023/A:1011885631876.
18. E.G. Pickering, M.R. O'Masta, H.N.G. Wadley, V.S. Deshpande: Effect of confinement on the static and dynamic indentation response of model ceramic and cermet materials, Int. J. Impact Eng., 110, 2017, 123–137. https://doi.org/10.1016/j.ijimpeng.2016.12.007.
19. S.G. Savio, K. Ramanjaneyulu, V. Madhu, T.B. Bhat: An experimental study on ballistic performance of boron carbide tiles, Int. J. Impact Eng., 38, 2011, 535–541. https://doi.org/10.1016/j.ijimpeng.2011.01.006.
20. M. Cegła, W. Habaj, W. Stępniak, P. Podgorzak: Hybrid Ceramic-Textile Composite Armour Structures for a Strengthened Bullet-Proof Vest, Fibres Text. East. Eur., 1, 2015, 85–88. https://doi.org/www.fibtex.lodz.pl/2015/1/85.pdf.
21. C. Evci, M. Gülgeç: Effective damage mechanisms and performance evaluation of ceramic composite armors subjected to impact loading, J. Compos. Mater., 48, 2014, 3215–3236. https://doi.org/10.1177/0021998313508594.
22. N.A. Nordendale: *Modeling and simulation of brittle armors under impact and blast effects*, Tennessee: Vanderbilt University, 2013. https://etd.library.vanderbilt.edu/available/etd-08132013-114834/unrestricted/Nordendale.pdf.
23. H.K. Şenyilmaz, G. Ceylan, V. Alankaya, A. Kurultay: Effect of material model to the result of high velocity impact analysis, J. Nav. Sci. Eng., 10, 2014, 48–65.
24. Z. Fawaz, W. Zheng, K. Behdinan: Numerical simulation of normal and oblique ballistic impact on ceramic composite armours, Compos. Struct., 63, 2004, 387–395. https://doi.org/10.1016/S0263-8223(03)00187-9.
25. O.M. Sanusi, O.A. Oyelaran, J.A. Badmus: Ballistic study of alumina ceramic-steel composite for structural applications, J. Ceram. Process. Res., 21, 2020, 501–507. https://doi.org/10.36410/jcpr.2020.21.4.501.
26. O.M. Sanusi, M. Dauda, M. Sumaila, A.S. Ahmed, M.T. Isa, O.A. Oyelaran, O.O. Martins: Compositions Optimization of Antang Corundum for Developing Advanced Ceramic, Aceh Int. J. Sci. Technol., 7, 2018, 32–43. https://doi.org/10.13170/aijst.7.1.8770.
27. Abaqus: *Abaqus Theory Manual and User's Manual*, Dassault Systemes Simulia Corp., Providence, RI, USA, 2012.
28. NIJ Standard 0108.01: *Ballistic Resistant Protective Materials*, National Institute of Justice. (1985). https://www.ncjrs.gov/pdffiles1/nij/099859.pdf.
29. P. Kędzierski, A. Morka, G. Sławiński, T. Niezgoda: Optimization of two-component armour, Bull. Polish Acad. Sci. Tech. Sci., 63, 2015, 173–179. https://doi.org/10.1515/bpasts-2015-0020.
30. C.W. Isaac, O. Oluwole: Numerical modelling of the effect of non-propagating crack in circular thin-walled tubes under dynamic axial crushing, Thin-Walled Struct., 115, 2017, 119–128. https://doi.org/10.1016/j.tws.2017.02.012.
31. M. Lee, Y.H. Yoo: Analysis of ceramic/metal armour systems, Int. J. Impact Eng., 25, 2001, 819–829. https://doi.org/10.1016/S0734-743X(01)00025-2.
32. C.W. Isaac: Crushing response of circular thin-walled tube with non-propagating crack subjected to dynamic oblique

impact loading, Int. J. Prot. Struct., 11, 2020, 41–68. https://doi.org/10.1177/2041419619849087.
33. A.P.T.M.J. Lamberts: Numerical simulation of ballistic impacts on ceramic material, Netherlands: Eindhoven University of Technology, 2007.
http://www.mate.tue.nl/mate/pdfs/8206.pdf.
34. D. Burger, M. V Donadon, F. Cristovao, S.F. Muller: Formulation and implementation of a constitutive model for brittle materials in Abaqus explicit finite element code, in: *Proc. COBEM—20th Int. Congr. Mech. Eng.*, Gramado, Brazil, Gramado-RS: Brazilian Association of Engineering and Mechanical Sciences, p. 1–12, 2009.
35. L. Ming, O. Pantalé: An efficient and robust VUMAT implementation of elastoplastic constitutive laws in Abaqus/Explicit finite element code, Mech. Ind., 19, 2018, 308. https://doi.org/10.1051/meca/2018021.
36. D.S. Cronin, K. Bui, C. Kaufmann, G. Mcintosh, T. Berstad: Implementation and Validation of the Johnson-Holmquist Ceramic Material Model in LS-Dyna, in: *4th Eur. LS-DYNA Users Conf.*, Germany, Ulm: DYNA, p. 47–60, 2004.
37. J. Hub, P. Kneys: 3D Simulation Analysis of Aircraft Protection Material, University Review, 7, 2013, 15–19.
38. L. Turhan, Ö. Eksik, E.B. Yaln, A. Demirural, T. Baykara, V. Günay: Computational simulations and ballistic verification tests for 7.62mm AP and 12.7mm AP bullet impact against ceramic metal composite armours, WIT Trans. Built Environ., 98, 2008, 379–388. https://doi.org/10.2495/SU080371.
39. M. Hajheydari, S.A. Eftekhari: Simulation and numerical analysis of optimized ceramic-composite armor under vertical ballistic impact, Int. J. Basic Sci. Appl. Res., 3, 2014, 184–199.
40. A. Healey: *Understanding the ballistic event: Methodology and observations relevant to ceramic armour*, England: University of Surrey, 2017.
41. MIL-STD-662F: *V50 Ballistic Test for Armor*, Dep. Def. Test Method Stand., 1997. http://everyspec.com/MIL-STD/MIL-STD-0500-0699/MIL-STD-662F_6718/.
42. P. Gotts: International ballistic and blast specifications and standards, in: *Lightweight Ballistic Composites*, Second, A. Bhatnagar (Ed.), Amsterdam: Woodhead Publishing, Elsevier Ltd., p. 115–156, 2016.
https://doi.org/http://dx.doi.org/10.1016/B978-0-08-100406-7.00005-2.
43. Ş.H. Atapek: Development of a New Armor Steel and its Ballistic Performance, Def. Sci. J., 63, 2013, 271–277. https://doi.org/10.14429/dsj.63.1341.
44. N. Kiliç, B. Ekici: Ballistic resistance of high hardness armor steels against 7.62 mm armor piercing ammunition, Mater. Des., 44, 2013, 35–48.
https://doi.org/10.1016/j.matdes.2012.07.045.
45. T. Wierzbicki: Petalling of plates under explosive and impact loading, Int. J. Impact Eng., 22, 1999, 935–954. https://doi.org/10.1016/S0734-743X(99)00028-7.
46. P.K. Jena, B. Mishra, K. Siva Kumar, T.B. Bhat: An experimental study on the ballistic impact behavior of some metallic armour materials against 7.62mm deformable projectile, Mater. Des., 31, 2010, 3308–3316. https://doi.org/10.1016/j.matdes.2010.02.005.

ACTA METALLURGICA SLOVACA
2021, VOL. 27, NO. 2, 87-93

RESEARCH PAPER

MECHANICAL DAMPING CHARACTERISTICS OF DUCTILE AND GREY IRONS MICRO-ALLOYED WITH COMBINATIONS OF Mo, Ni, Cu AND Cr

Sylvester Olanrewaju Omole[1*], Kenneth Kanayo Alaneme[1, 2], Akinlabi Oyetunji[1]

[1]Department of Metallurgical and Materials Engineering, School of Engineering and Engineering Technology, Federal University of Technology, Akure, PMB 704. Ondo State Nigeria.

[2]Centre for Nano Engineering and Tribo Corrosion, School of Mining, Metallurgical and Chemical Engineering, University of Johannesburg, Johannesburg South Africa.

*Corresponding author: sylvesteromole@yahoo.com, soomole@futa.edu.ng Tel. 2347033089934, Department of Metallurgical and Materials Engineering, Federal University of Technology, Akure. P. M. B 704. Ondo State Nigeria.

Received: 10.12.2020
Accepted: 24.01.2021

ABSTRACT

Damping behaviour of ductile and grey cast irons micro alloyed with combinations of Mo, Ni, Cu and Cr, was investigated in this study. This was aimed at establishing the effect of composition and microstructural parameters on the damping properties of the micro alloyed cast irons. Grey cast iron was micro alloyed randomly with molybdenum, nickel, chromium and copper at an amount not more than 0.2 % each; magnesium was added to the melt in ladle prior to casting. The microstructures showed that ductile iron was formed and grey iron was also formed due to insufficient 'nodulizer', the ductile iron consisted of pearlite and ferrite phases with their nodular graphite. The micro-alloyed ductile iron generally had higher storage (78906 – 120868 MPa) and loss modulus (5375 – 6715 MPa) than that of the grey cast iron and ductile iron composition without alloying elements. Although the damping capacity of the composition without micro alloying elements was initially higher for all the cast irons (~ 0.085), but failed at approximately 110 °C, while most of the micro-alloyed ductile irons exhibited relatively satisfactory capacity for vibration energy dissipation up to 190 °C than the micro-alloyed grey irons.

Keywords: Damping; microalloying; mechanical, ductile and grey cast iron, temperature; frequency

INTRODUCTION

The utilization of ductile irons has increased globally as a result of its good mechanical properties, low cost of production, and adaptability for mass production [1]. However, they possess moderate to low corrosion, fracture, wear resistance and damping capacity – properties that are now critical requirements for several nascent automobile and machinery components [2, 3]. This has raised concerns about the continued suitability of ductile irons, for the design of these mechanical systems [4]. This development has challenged the iron metallurgy community to explore ways of enhancing the material property spectrum of ductile irons while still maintaining low cost processing which has been an age long attraction for ductile irons [5, 6].

Several researchers have explored the use of micro alloying elements such as nickel, copper, chromium, molybdenum, among others to improve the properties of ductile irons [7]. Rao et al. [8] reported that manganese/copper ratio can be optimally selected for enhanced pearlite formation, which results in improved mechanical properties in ductile irons. Similar outcome was achieved with the use of manganese, nickel, molybdenum, and copper as micro alloying addition, as long as the composition of these elements did not exceed 0.5% [9].

It has been reported that optimal selection of combinations of Mo, Cr, Ni and Cu as micro alloying addition in ductile irons, results in improved strength, toughness and wear resistance [10, 11]. However, the effect of these micro alloying additions on the damping properties of ductile irons has not come under scrutiny. High damping capacity is considered as one of the required properties needed in the selection of material for several machinery and automobile elements, where high vibration damping resistance is very critical for optimal service performance [12]. The performance of dynamic mechanical and construction equipment, often results in undesirable vibration which have negative impact on the life of the machine [13]. Generally, the damping capacity of cast irons is reported to be influenced by factors such as the internal friction mechanism of the graphite, graphite volume fraction, count and morphology, matrix structure, matrix phase surrounding the graphite, presence of alloying elements, among others [14-16]. These microstructural variables are largely dependent on the composition, and processing deployed for the cast iron production [17, 18]. Pereira et al. [19] stated that generally, any material that has the capacity to dissipate energy of vibration otherwise known as loss modulus, will minimize noise and vibration. In the case of ductile irons, solid solution strengthening of the ferritic matrix phase of a ductile iron as well as increase in the nodule density, was reported to help improve the damping capacity in ductile irons. However, the impact on these phase and graphite parameters and the consequential effect on the damping properties of the specific alloy combinations selected as micro-alloying additions in this

study, to the best of our knowledge has not received attention from literature.

Hence, the aim of this study is to evaluate the influence of the selected microalloying combinations on the mechanical damping properties (storage modulus, loss modulus and damping capacity) of the ductile and grey irons developed. The research questions which the present study intends to provide answers to are: does the micro alloying composition influence damping properties of the ductile irons produced? How are the damping properties influenced by the test conditions such as test frequency and temperature? What are the underlying mechanisms responsible for the damping characteristics displayed by the ductile irons? Are these postulations supported by microstructural evidences? That is, can the microstructures help elucidate the damping behaviour manifested by the ductile irons? It is envisaged that the outcomes from the investigation will help establish the reliability of the selected micro alloying combinations for practical utilization of ductile irons in component design for automobile and machinery applications, where an excellent balance of damping, mechanical and wear properties are desirable.

MATERIAL AND METHODS

Ductile Irons Production

The procedures adopted for the production of the ductile irons have been reported in details by Omole et al. [10, 11]. The process summarily, involved utilization of grey cast iron scrap as base metal, while ferro-molybdenum (72%), ferro-chrome (64% Cr), copper and nickel, were utilized as micro alloying additions. Ferrosilicon magnesium (5 % Mg, 45 % Si), graphite (as recarburiser), calcium carbide (as sulphur removal) and calcium carbonate (as flux), were other materials utilized as casting additives. Seven charge compositions were prepared for the ductile iron production with micro alloying combinations and weight percent, added in proportions as presented in **Table 1**.

The cast irons were produced by melting the base metal (grey iron scraps) and then adding the respective alloying elements to the melt. The melt was super-heated to 1430 °C and then tapped into a ladle containing magnesium in the ladle pocket and was cast to produce the ductile irons. Cast irons were allowed to solidify to room temperature in green sand mould before knockout of the castings in the mould. The chemical compositions of the cast irons produced are shown in **Table 2**. After the production, it was noted that two of the seven compositions did not develop ductile iron structures but that of grey irons, thus the compositions were designated AG1 and AG2, to distinguish them from the other compositions which developed nodular structures.

Characterization with Optical Microscope

Each specimen was first prepared through metallographic processes of grinding and polishing. This was done using different grits of grinding and polishing paper with pastes to obtain a mirror finished surface. The polished surfaces were etched using 4% nital for 10 seconds. The structures were examined with Zeiss optical microscope with Axiom5 camera attachment.

Damping Test

Assessment of the damping properties of both the ductile and grey irons were carried out on a Dynamic Mechanical Thermal Analyzer (DMTA) using three-point bending mode in accordance with ASTM 756 -05 (2017) [20] standard. Specimens used for this study were machined to a flat rectangular shape of dimension 5 mm width by 2 mm thickness and 55 mm length. The thermal analysis determines the stiffness of the materials under the application of dynamic load as a function of temperature, frequency, amplitude and time. The test was performed using strain amplitude of 2 µm (2×10^{-6}), vibration frequency of 1 and 5 Hz, temperature range of room temperature to 200 °C and heating rate of 5 °C per minute. The parameters evaluated are: the storage modulus (dynamic modulus) (E'), loss modulus (E") and damping capacity (also known as tan δ) – which was determined using the relation [21]:

$$\text{Tan } \delta = \frac{E''}{E'} \quad . \qquad (1.)$$

Table 1 Charges Combination for Melting in the Furnace

Melt/ Sample	Initial Charge Material in the Furnace
AD1	Fe scrap, graphite (C), Si, Mn (in base metal), 0.15%Mo, 0.15%Ni, 0.15%Cu
AD2	Fe scrap, graphite (C), Si, Mn (in base metal), 0.15%Mo, 0.15%Ni
AD3	Fe scrap, graphite (C), Si, Mn (in base metal), 0.15%Cu, 0.15%Cr
AD4	Fe scrap, graphite (C), Si, Mn (in base metal), 0.15%Mo, 0.15%Ni, 0.15%Cr
D5	Fe scrap, graphite (C), Si, Mn (in base metal),
AG1	Fe scrap, graphite (C), Si, Mn (in base metal), 0.15%Mo, 0.15%Cr, 0.15%Cu
AG2	Fe scrap, graphite (C), Si, Mn (in base metal), 0.15%Ni, 0.15%Cu, 0.15%Cr

Note: AD denotes alloyed ductile iron, D5 unalloyed ductile iron and AG denotes alloyed grey iron

Table 2 Chemical Composition of the Specimens Produced

6.5	AD1	AD2	AD3	AD4	D5	AG1	AG2
CE	4.27	4.38	4.14	4.23	4.18	4.16	4.33
%C	3.42	3.50	3.20	3.40	3.30	3.30	3.45
%Si	2.50	2.60	2.80	2.45	2.62	2.53	2.60
%Mn	0.35	0.39	0.53	0.50	0.42	0.58	0.47
%Mo	0.11	0.19	-	0.24	-	0.13	-
%Ni	0.16	0.22	-	0.18	-	-	0.16
%Cr	-	-	0.12	0.10	-	0.11	0.11
%Cu	0.20	-	0.21	-	-	0.19	0.19
%Mg	0.073	0.086	0.095	0.091	0.081	0.039	0.032
%S	0.030	0.034	0.026	0.031	0.027	0.026	0.030
%P	0.048	0.042	0.030	0.048	0.029	0.041	0.042

RESULTS AND DISCUSSION
Microstructure Characterization

The microstructures of the cast irons produced are presented in **Figure 1**. It is observed that **Figures 1(a) – 1(e)** contain nodular/spheroidal graphite morphology, which indicates that the structures are that of ductile irons. It is noted that the matrix structure of the ductile irons consists of pearlite and ferrite phases with proportions as presented in **Table 3**.

The nodular graphite structures are observed to be circumscribed by ferrite in their immediate vicinities. This is in accordance with microstructure study by many authors [22-24]. However, it is more pronounced for the compositions AD1, AD2 and AD4, which contain Mo-Ni-Cu, Mo-Ni, and Mo-Ni-Cr, respectively as micro-alloying elements. AD3 which contains Cu-Cr did not have as much ferrite surrounding the nodular graphite as in the other micro-alloyed ductile iron compositions. It is also confirmed from **Table 3** that it has the least volume fraction of ferrite for all the cast iron compositions produced. Figures 1(f) and 1(g) on the other hand, show flaky graphite structure, which is characteristic of grey irons. It is noted that the two compositions, AG1 and AG2, both contain micro alloying elements – Mo-Cr-Cu and Ni-Cr-Cu, respectively. The quantified microstructural parameters for the cast irons produced are presented in **Table 3**.

Table 3 Results of Microstructure Characterization of all the Samples (Omole et al. [11]).

Sample	Volume fraction of Pearlite	Volume fraction of Ferrite	Volume fraction of Nodule/ Pearlite	Nodularity %	Nodules count (per mm^2)
AD1	49.38 % ±2.55	38.93 % ±2.35	11.14 % ±1.82	91	110
AD2	49.70 % ±2.82	40.11 % ±2.64	10.98 %±1.68	90	115
AD3	56.06% ±1.85	29.83 % ±2.43	14.51 %±2.08	88	105
AD4	56.59 % ±2.32	32.68 % ±2.42	11.31 %±1.95	92	120
D5	30.63 % ±2.12	59.37 % ±2.71	10.27% ±2.10	88	107
AG1	37.37% ± 2.26	39.86 % ±2.25	22.73% ±2.20	-	-
AG2	33.12% ± 2.22	51.82 % ±2.18	15.50% ±2.16	-	-

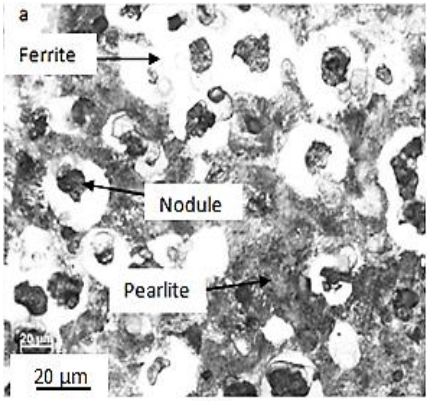

AD1

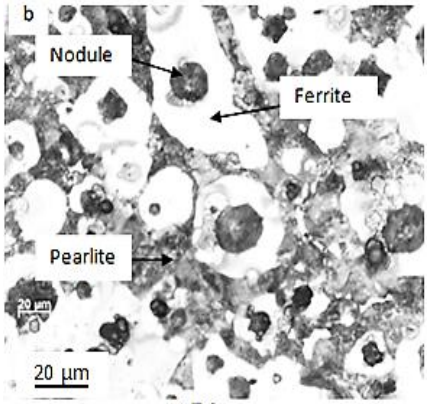

AD2

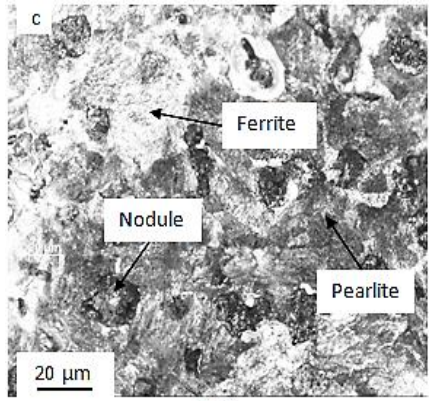

AD3

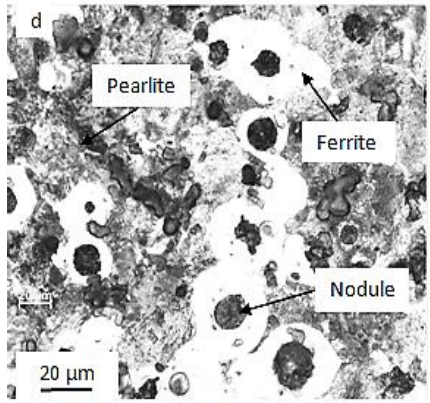

AD4

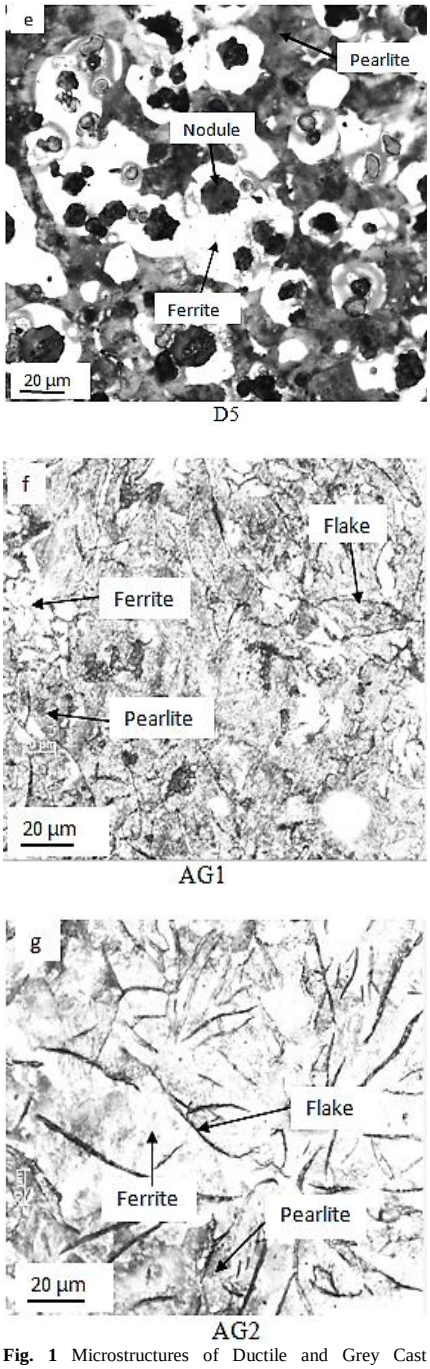

Fig. 1 Microstructures of Ductile and Grey Cast Irons Produced (a to e are the microstructures of ductile iron with nodules while f and g are the microstructures of grey iron containing flakes)

Damping Behaviour

The results of the damping tests are presented in **Figures 2 – 4**. It is observed from **Figures 2(a) and (b)** that the storage modulus, which serves as a measure of the capacity of a material to absorb/store vibration energy is marginally influenced by the test frequencies (1 and 5 Hz) utilized in the study. From **Figure 2(a)**, it is noted that the ductile iron composition designated AD2 (which contains Mo-Ni), had the highest storage modulus values (120868.51 MPa), compared to the other ductile and grey irons investigated. Generally, it is noted that the storage modulus of the micro alloyed ductile irons (78906.39 – 120868.51 MPa) were higher than that of the micro alloyed grey irons (61118.79 – 79314.9 MPa), and the ductile iron composition without micro alloying elements, had the least storage modulus (19890.19 – 19699.15 MPa). This can be confirmed in **Table 4**.

The way of absorbing energy during damping test by cast irons is said to depend on the graphite count of the iron, graphite surface areas and the contact interaction of ferrite phase with the graphite [16]. The additional effect of contact interaction between the ferrite and graphite phases, which is more pronounced in the micro-alloyed ductile irons, may be linked to the higher storage modulus exhibited by the micro-alloyed ductile irons compared with the micro-alloyed grey irons. It is also noted that with the exception of the ductile irons designated AD1 and AD4, there was basically slight reduction in storage modulus with increase in temperature within the range of 40 – 190 °C used in the study.

Alaneme and Fajemisin [25] reported that decrease in storage modulus is associated with increase in temperature, because of the decrease in dynamic stiffness of the material with temperature, which arises on account of the weakening of inter-atomic bonds in the material. The implication of the higher storage modulus of the micro alloyed ductile irons is that they possess higher energy absorption capacity compared to the other cast iron grades produced. Virtually the same trend and arguments subsists for the storage modulus values assessed at both test frequencies of 1 and 5 Hz.

The loss moduli of the ductile and grey irons produced are presented in **Figure 3**. It is observed that why apparently the loss modulus appears to follow the same trend at both 1 and 5 Hz test frequencies, the loss modulus values in most cases, are slightly higher at test frequencies of 1 Hz compared to 5 Hz, as can be confirmed from **Table 5**. The effect of cast iron composition and test temperature was however, more distinct and consistent than that of test frequency. It is observed from **Figure 3** that for both test frequencies, the micro alloyed ductile irons with the exception of AD2 had higher loss modulus values which decreased with intermittent high peaks at temperatures between 40 to 190 °C than the other cast iron compositions produced. Ibrahim et al. [16] reported that increase in energy dissipation is enhanced in cast irons with greater graphite count and higher amount of ferrite surrounding the graphite nodules. That is, the ferrite surrounding the graphite serve as additional vent for energy dissipation due to the easier plastic flow that occurs in the interface between the graphite and ferrite phases [2]. In the grey irons, the energy dissipation is ideally linked squarely to the internal friction mechanism which occurs in the graphite precipitate [14, 15]. But in the ductile irons, the ferrite surrounding the graphite contributes to the greater energy dissipation observed. The least loss modulus and storage modulus was observed in the ductile iron composition without micro-alloying addition.

The decrease in loss modulus with temperature may be as a result of reduction in internal friction of the material as the kinetic energy increases with increase in temperature. The

implication is that there is slight reduction in energy dissipation capacity of the irons with increase in temperature.

The damping capacities of the cast irons produced are presented in **Figure 4**. It is observed that the damping capacity variation pattern was slightly different at the test frequencies of 1 and 5 Hz. It is observed that at 30 °C, the damping capacities of the micro alloyed ductile irons AD3, AD1 and AD4 are higher than that of other cast irons investigated. The damping capacities are observed to drop sharply from ~ 0.07 – 0.08 at 30 °C to ~ 0.06 at 50 °C; after which fairly more stable values with intermittent high and low peaks were obtained for these ductile iron compositions. The ductile iron composition without micro alloying elements (D5), exhibited the reverse trend as its damping capacity values increased from 0.057 at 30 °C to approximately 0.09 at 110 °C, which was the temperature at which the sample failed. Despite the higher damping capacity values above that of samples AD3, AD1 and AD4, the fact that it failed at a relatively lower temperature of 110 °C compared to the other cast irons tested to temperature of 190 °C, raises concerns on its suitability compared to the other cast irons produced. The ductile iron composition AD2 is observed to have the lowest damping capacity, which can be linked to its high energy absorption capacity and relatively low energy dissipation characteristics. It is also noted that the micro-alloyed grey irons had damping capacity values lower than that of the other micro alloyed ductile irons – AD3, AD1, AD4.

The generally higher damping capacity of the micro-alloyed ductile irons can be attributed to contributions of the graphite nodules and the ferritic matrix surrounding the graphite [16], as is observed in **Figure 1.** The ferrite phase circumjacent to the spherical graphite ensures that plastic flow occurs more readily in the interface between the graphite and ferrite phases, thereby resulting in higher damping capacity. Thus, the higher the number of graphite nodules and nodules surrounded by ferrite, the higher the damping capacity due to the higher (energy absorption/dissipation centres) contact surface between graphite and ferrite, which help attenuate vibration effects and thus resulting in higher damping capacity in the ductile irons. It is also worth remarking that the effect of the test frequency was more consistent at near room temperature, where it is observed that the damping capacity values for AD3, AD1 and AD4, are lower at test frequency of 5 Hz than that observed at 1 Hz (as shown in **Table 6**).

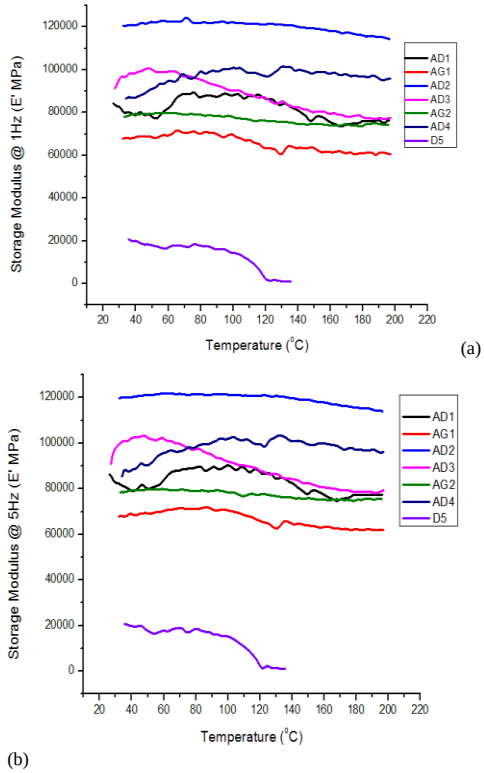

Fig. 2 Storage Modulus as a function of Temperature at (a) 1 and (b) 5 Hz Frequencies

Table 4 Storage Modulus of all the Specimens @ 40 °C and 190 °C for Test Frequencies of 1 and 5 Hz

Sample	Storage Modulus (MPa) @ 40 °C		Storage Modulus (MPa) @ 190°C	
	1 Hz	5 Hz	1 Hz	5 Hz
AD1	78906.39	79165.72	76184.99	77360.41
AD2	120868.51	120245.91	115283.00	114702.71
AD3	98523.26	102349.12	77429.42	78493.48
AD4	87073.29	88296.05	95879.31	97159.99
D5	19890.19	19699.15	-	-
AG1	68490.37	68965.09	61118.79	62006.61
AG2	79272.43	79314.91	74634.42	75452.19

Table 5 Loss Modulus of all the Specimens @ 40 °C and 190 °C for Test Frequencies of 1 and 5 Hz

Sample	Loss Modulus (MPa)@ 40 °C		Loss Modulus (MPa)@ 190 °C	
	1 Hz	5 Hz	1 Hz	5 Hz
AD1	5757.99	5375.53	3909.57	3261.29
AD2	2833.05	2727.13	2332.38	2460.96
AD3	6124.51	6016.62	3197.31	3523.58
AD4	6715.14	5351.41	3949.63	3518.53
D5	1338.41	1272.11	-	-
AG1	3889.74	3023.77	2690.81	2258.51
AG2	2026.64	1841.51	2471.03	2063.11

Table 6 Damping Capacity of all the Specimens @ 40 ^{O}C and 190 ^{O}C for Test Frequencies of 1 and 5 Hz

Sample	Damping Capacity (tan δ) @ 40^{O}C		Damping Capacity (tan δ) @ 190^{O}C	
	1 Hz	5 Hz	1 Hz	5 Hz
AD1	0.07298	0.06790	0.05131	0.04216
AD2	0.02343	0.02268	0.02023	0.02146
AD3	0.06217	0.05878	0.04128	0.04489
AD4	0.07714	0.06062	0.04120	0.03621
D5	0.06477	0.06007	-	-
AG1	0.05678	0.04384	0.04402	0.03643
AG2	0.02557	0.02322	0.03311	0.02734

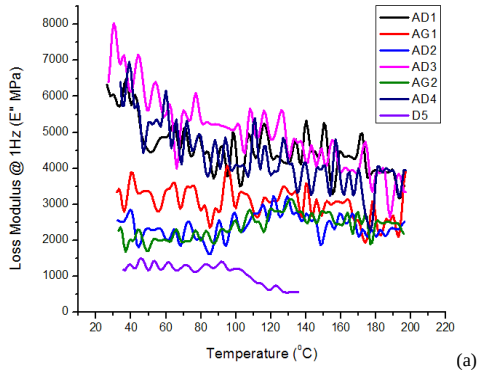

(a)

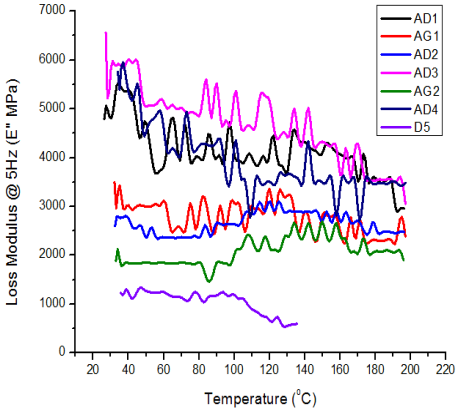

(b)

Fig. 3 Loss Modulus as a function of Temperature at (a) 1and (b) 5 Hz Frequencies.

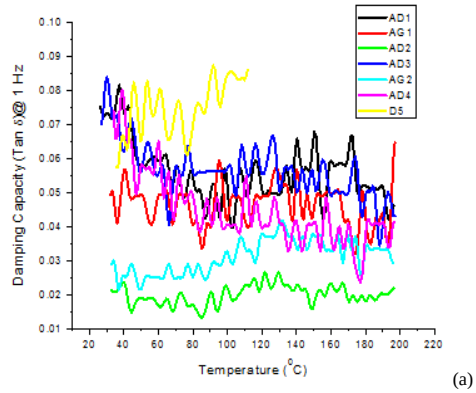

(a)

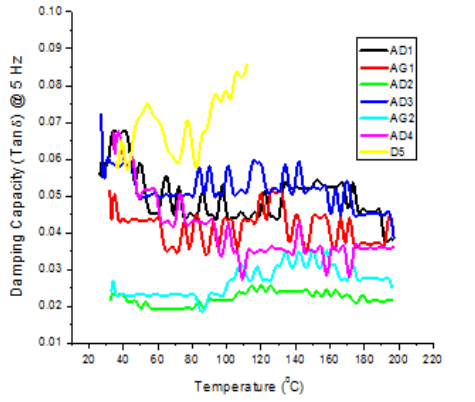

(b)

Fig. 4 Damping Capacity (Tan δ) as a function of Temperature at (a) 1and (b) 5 Hz Frequencies.

CONCLUSIONS

In this study, the damping characteristics of ductile and grey cast irons, micro alloyed with Mo, Ni, Cu and Cr, investigated using dynamic mechanical thermal analysis, were reported. The results indicated that:

The Microstructures of the ductile irons contain pearlite, ferrite and graphite nodules with nodules count in various proportions. The presence of ferrite phase surrounding the nodular graphite with the nodule count, accounted for the high damping capacity obtained.

Ductile iron without micro alloying elements had the least storage modulus (19890.19 – 19699.15 MPa), while the micro alloyed ductile irons had higher storage modulus (78906.39MPa – 120868.51 MPa) than the micro alloyed grey cast iron (61118.79 – 79314.9 MPa). So, the energy absorption was noticed to be dependent on the graphite count and interaction of ferrite phase with the graphite among others.

The loss modulus of all the samples was distinctly affected by the composition and test temperature than the test frequency. However, for both test frequencies, most of the micro alloyed ductile irons basically had higher loss modulus values than the grey cast iron.

Damping capacity of sample D5 (without micro alloying elements) increased progressively from 0.06007-0.06477 at room temperature to ~ 0.085 at about 110 ^{o}C and failed, while samples AD1 AD3 and AD4 damping capacity was higher at room temperature but dropped at 50 ^{o}C and after which stable values was observed even at high temperatures. Therefore, samples AD1, AD3 and AD4 displayed the compositions most suitable for mechanical damping.

ACKNOWLEDGEMENTS

The authors wish to thank the Head, School of Mining, Metallurgy and Chemical Engineering, and Centre for Nano Engineering and Tribo-corrosion, University of Johannesburg, Johannesburg South Africa, Prof. P. A. Olubambi, who assisted in the provision of facilities needed for the research.

REFERENCES

1. J. L. Hernandez-Rivera, R. E. Compos Cambranis, A. De la Garza: Materials Design, 32, 2011, 4756–4762. https://doi.org/10.1016/j.matdes.2011.06.030.
2. C-Y. Kang, J-H. Sung, G-H. Kim, B-S. Kim, I-S. Kim: Materials Transaction, 50(6), 2009, 1390–1395. https://doi.org/10.2320/matertrans.MRA2008427.
3. F. Iacoviello, D. Iacoviello, V. D. Cocco, A. D. Santis, L. D. Agostino: Procedia structural integrity, 3, 2017, 283–290. https://doi.org/10.1016/j.prostr.2017.04.042.
4. C. Fragassa: Journal of Mechanical Engineering Science, 231(1), 2017, 18–30. https://doi:10.1177/0954406216639996.
5. M. M. Rashidi, M. H. Idris: Materials Science and Engineering A, 597, 2014, 395–407. https://dx.doi.org/10.1016/j.msea.2013.12.070.
6. J. Laine, K. Jalava, J. Vaara, K. Soivio, T. Frondelius, J. Orkas: International journal of Metal casting, 2020. https://doi.org/10.1007/s40962-020-00473-8.
7. G. Lannitti, A. Ruggiero, N. Bonora, S. Masaggia, F. Veneri: Theoretical and Applied Fracture Mechanics, 92, 2017, 351-359. https://dx.doi.org/10.1016/j.tafmec.2017.05.007.
8. L. Rao, W. Tao, S. Wang, M. Geng, G. Cheng: Indian Journal of Engineering and Materials Science, 21, 2014, 573-579.
9. K. J. Mohammed: Unified Journal of Engineering and Manufacturing Technology, 1(1), 2016, 001-006.
10. S. O. Omole, A. Oyetunji, K. K. Alaneme, P. A. Olubambi: Tribology in industry, 40(4), 2018, 584–593. https://doi.10.24874/ti.2018.40.04.07. 2018.
11. S. O. Omole, A. Oyetunji, K. K. Alaneme, P. A. Olubambi: Journal of King Saud University-Engineering Sciences, 32, 2020, 205-210. https://doi.org/10.1016/j.jksues.2018.11.00.
12. M. Ramadan, N. Fathy: Journal of Minerals and Materials Characterization and Engineering 2, 2014, 26–31. https://dx.doi.org/10.4236/jmmce.2014.21005.
13. P. Kovacikova, J. Vavro, J. Vavro Jr, A. Dubec: Manufacturing Technology, 18(1), 2018, 57–59. https://doi:10.21062/ujep/53.2018/a/1213-2489/MT/18/1/57.
14. P. Millet, R. Schaller, W. Benoit: Journal de Physique Colloques, 46(C10), 1985, C405-C408.
15. T. Murakami, T. Inoue, H. Shimura, M. Nakano, S. Sasaki: Materials Science and Engineering A, 432, 2006, 113–119. https://doi.10.1016/j.msea.2006.06.090.
16. M. M. Ibrahim, M. M. Mourad, A. A.Nofal, A. I. Z. Farahat: International Journal of Cast Metals Research, 30(2), 2017, 61-69. https://doi.org/10.1080/13640461.2016.1239895.
17. J. Cui, L. Chen: Journal of Materials Science and Technology, 33(12), 2017, 1549-1554. https://dx.doi.org/10.1016/j.jmst.2017.08.03.
18. T. Sun, R-B. Song, X. Wang, P. Deng, C-J Wu: Materials Science and Engineering A, 626, 2015, 375-381. https://dx.doi.org/10.1016/j.msea.2014.12.078.
19. I. Pereira, G. Alonso, V. Anjos, L. F. Malheiros, R. Suarez: International journal of metal casting, 14, 2020, 802–808. https://doi.org/10.1007/s40962-020-00426-1.
20. ASTM E756-05: Standard test method for measuring vibration damping properties of materials. *ASTM standard 2017* www.astm.org.
21. D. Silva-Prasad, C. Shoba: Engineering Science and Technology - International Journal, 18, 2015, 674–679. https://doi.org/10.1016/j.jestch.2015.05.001.
22. H. Ananda, S. Sathyashandra, V. S. Ramakrishna: Journal of Mechanical Engineering and Sciences, 13(1), 2019, 4356-4367. https://doi.org/10.15282/jmes.13.1.2019.01.0371.
23. N. S Tiedje: Materials Science and Technology, 26(5), 2010, 505-514. https://doi.org/10.1179/026708310X12668415533649.
24. C. Fragassa, N. Radovic, A. Pavlovic, G. Minak: Tribology in Industry, 38(1), 2016, 45-56.
25. K. K. Alaneme, A. V. Fajemisin: Engineering Science and Technology, an International Journal, 21, 2018, 798-805. https://doi.org/10.1016/j.jestch.2018.05.007.

ACTA METALLURGICA SLOVACA
2021, VOL. 27, NO. 2, 94-98

SHORT COMMUNICATION

OPTIMIZATION OF THE THERMAL PROCESS OF ABRASIVE METAL WORKING

Viacheslav Oleksenko[1*]

[1] Institute of Education and Science in Mechanical Engineering and Transport, National Technical University „Kharkiv Polytechnic Institute“, 61002, 2, Kyrpychova str., Kharkiv, Ukraine

*Corresponding author: Viacheslav.Oleksenko@khpi.edu.ua, tel.: +38057-707-60-35, Institute of Education and Science in Mechanical Engineering and Transport, National Technical University „Kharkiv Polytechnic Institute“, 61002, 2, Kyrpychova str., Kharkiv, Ukraine

Received: 09.03.2021
Accepted: 15.03.2021

ABSTRACT

The main problem that arises from grinding metal is the generation of a large amount of heat. Exceeding a critical temperature will damage the part. However, determining the heat of the metal being processed is a difficult task both practically and theoretically. The correct choice of parameters for the abrasive processing is essential to obtain the required quality. This article describes a mathematical model that simulates the determination of the maximum heat on the surface of a metal part during grinding. This model features the ability to change the initial parameters so that the resulting temperature does not exceed the critical one. The model has been tested by a specially developed web application written in JavaScript. It not only calculates the highest temperature in the machining zone of the workpiece, but also optimizes the thermal grinding process to give appropriate recommendations. The features of such a program are disclosed, including its practical use in production.

Keywords: thermal process; metal; optimization; abrasive processing; model; computer program

INTRODUCTION

The key task in production is to create quality products. In industry, the quality of a product depends on the quality of its parts, which in turn depends on the machining of materials. Abrasive processing is widely used in factories to obtain increased accuracy and surface quality. For this purpose, special circles are used, the cutting elements of which are grains. Continuous improvement of machine tools and abrasive wheels has made this process a highly productive one. The workpieces can be processed with micron precision and excellent roughness, which can be achieved, for example, by grinding or polishing.

A common problem in abrasive metal working is an increase in temperature. Heat is generated when the abrasive grain is loaded. Thermal phenomena arise and are concentrated in rather small areas. The generated heat energy provides intensive heating of the part, which can lead to a decrease in quality or damage. Temperatures can rise so high that changes in the structural composition of the surface layer, local melting, deformation, and the formation of microcracks are possible. As a result, the quality of the workpiece decreases or it becomes unsuitable for further use. This is a significant problem for industry, especially in those industries that require a lot of cutting and grinding. Enterprises thus suffer substantial losses. There are known cases of manufacturer's recalls occurring for batches of already sold product due to the fact that the defect was detected during operation. The fact is that the human eye may not notice thermal damage to the metal. A defected part which becomes part of the final product may make it unusable before the end of the warranty period.

In [1-3] the features of the thermal process in the processing of materials are discussed. This has also been further investigated by many scientists in various aspects [4-7].

Knowing the temperature of not only the part but also the contact surfaces of the cutting grain is important, since thermal conductivity to the grains is possible. Moreover, the temperature of these surfaces determines the diffusion breakdown and wear of the grinding wheels themselves. Therefore, the temperature factor becomes the main limitation in this process.

In [2, 3], contact and non-contact methods of measuring the temperature of the workpiece are studied. The disadvantages and problems of such operations are described. It is even more difficult to measure the temperature inside a metal part.

Temperature can be found from the well-known differential heat equation. However, as a partial differential equation, it has an infinite number of solutions. To select the solution that describes the grinding process from this set, additional conditions must be imposed on the sought temperature function. These are called initial or boundary conditions. Due to the stochasticity of abrasive machining, this is a very difficult task. At the moment, the variety of mathematical descriptions available does not reflect all the nuances of the grinding process. However, this is not necessary if only the basic patterns are being studied. Therefore, scientists followed the path of rational systematization and used simplified models.

The creation of a model that is as close as possible to the real grinding process and the development on its basis of a computer program that calculates the temperature, speed, force, and other parameters of grinding and which gives appropriate practical recommendations will change the production of products around the world. In view of the importance of this model and without exaggeration, I note that the demand for

such a program would be greater than that for the vaccine against COVID-19.

The results of the analysis of publications indicate the great interest of researchers in the problem of thermal modeling in the processing of materials. In the 20th century, many scientists made a significant contribution toward a solution, including Jaeger (1942), Rikalin (1959), Hahn (1962), Rediko (1962), Makino (1966), Malkin (1971), Maslov (1974), Snoeys (1978), Lavine (1989), Morgan (1991), Qi (1993), Rowe (1994), and Tonshoff (1995).

In [8] formulas are obtained that allow calculating temperatures during friction at a constant speed. This studies considers two cases, and it assumes that the friction surface has the shape of a strip or the shape of a square bar. This study makes a significant contribution to the thermal physics of grinding. Thus far, scientists have used these results to study the moving belt heat source [4, 9]. Without diminishing the importance of these studies, I note that in belt grinding, the problem of temperature is not so acute, and it has narrow application in practice.

Another important approach is to consider a single abrasive grain as a source of heat. In this case, the average contact temperatures developing at the grinding site are determined. In [10], a method is proposed for determining the grinding temperature, taking into account the multiple superposition of heat pulses from the grains. Equations are obtained for the temperature not only at the contact surface of the abrasive grain, but also for the part depth. The sought equations are obtained from the differential heat equation. A criticism of this method can be found in [2, p. 124].

A general analysis of the literature of the 20th century makes it possible to conclude that initially the temperature of the part was judged by the nature and intensity of phase transformations in the surface layer during grinding. The dependence of the contact temperature on the grinding conditions was mainly determined experimentally. The theoretical calculation of grinding temperatures was carried out in accordance with the basic laws of heat transfer. Scientists, under certain conditions, determined the amount of heat in the grinding zone, established its distribution between the part and the wheel, or took into account coolants, etc. As a result, formulas and basic laws of thermal phenomena of the process under study were obtained from the differential heat equation, empirical results, the Fourier problem.

The modern metallurgical industry is constantly producing new types of alloys, which have their own coefficients of thermal conductivity, hardness, and other characteristics. Thermal phenomena occur differently for each material. Therefore, abrasive processing should take into account the latest scientific advances in this area such as:

- hard alloys [11],
- ceramics [12],
- polymorphic metals [13],
- aluminum alloys [14-16],
- composite materials [17],
- steels [18-21].

In the new millennium, the number of publications on the problem of thermal modeling has increased. In [9, 21, 22], the modeling of the temperature field of the workpiece, which is formed during the grinding process, is discussed.

Analysis of the literature of the 21st century with a focus on the problem posed makes it possible to conclude that scientists continue to solve the problem for a specific narrow case. The results are interesting, but not all are suitable for computer forecasting or use in factories. For example, the unsuitability for computer processing of the behavior of steel studied in [21] is explained by the use of volumetric heating. In practice, when grinding, this is surface heating.

The purpose of the article is to reveal the features of the thermal model during grinding and, on its basis, to develop a computer program for the approximate calculation of the maximum temperature on the surface of the workpiece and optimization of the grinding process in the thermal aspect.

MATERIAL AND METHODS

Particularly noteworthy is the Reznikov method, which calculates the temperature both on the cutting grain of an abrasive and grinding wheel, and on the material being processed. In [1, p. 126] the temperature on the surface of the part by the calculation method is determined. The method is shown using the example of flat grinding with an abrasive wheel. The law of temperature distribution on the surface of the part in the moving coordinate system associated with the circle is established, which is expressed by the formula:

$$Q_{max} = 52(1 - b^*)\frac{\sqrt{\omega}}{\lambda}\frac{m^{0.05}P_z v}{b\sqrt{v_1}B^{0.4}}, \quad (1.)$$

where b^*– coefficient characterizing the relative distribution of grinding heat between the wheel and the part,
λ – coefficient of thermal conductivity of the processed material,
ω – coefficient of thermal diffusivity,
P_z – tangential force during grinding,
v – circle speed,
m – the rate of decrease in the intensity of heat generation. Depending on the properties of the circle and the material of the workpiece, m = 0.01-0.03,
B, b – dimensions of the contact area of the circle with the part,
v_1 – speed of the part.

In [4] the theorem for finding maximal temperature in wet grinding is considered. It has been proven that such a temperature always occurs on the workpiece surface in the contact zone. The limitations concerned the constant heat transfer coefficient for the coolant acting on the workpiece surface and a constant or linear heat flux profiles entering into the workpiece.

RESULTS AND DISCUSSION

Mathematical model

To achieve the goal of the article, the following tasks are set:

- to create a mathematical model that allows for the determination of the maximum temperature in the contact zone of a metal part with an abrasive grain;
- to develop a program for calculating such a temperature;
- to create a program that provides pre-calculated values to ensure an optimal temperature for the grinding process.

The subject of research is the thermal process during metal grinding. The objective of the study is to determine the maximum temperature on the surface of the part and to optimize the thermal grinding process.

I will solve the assigned tasks on the assumption that the main results of [1, 4] are correct. Firstly, I will prove the theorem.

Theorem. The maximum temperature occurs on the surface of the grinded material with or without coolants.

Proof. Only two cases are possible when grinding:
(I) using coolants,
(II) not using coolants.

Consider case (I). In [4] it is found that the maximum temperature is reached at the surface of a part during wet grinding. Thus, in this case the theorem is proved.
Consider case (II). The proof is realizable by contradiction.
Suppose that the maximum temperature is not reached at the surface, but inside the material to be processed. I denote this with Q_1. Let Q_1 be at a distance $\Delta r > 0$ from the surface. Let Q_2 be the highest temperature on the surface of the processed material. Then

$$Q_1 > Q_2. \quad (2.)$$

Let me apply coolants at this moment. They come to the surface of the processed material. Therefore, cooling starts from the surface and Q_2 does not increase but can only decrease. According to the proved (I), the temperature Q_2 is the maximum in the entire material:

$$Q_2 > Q_1. \quad (3.)$$

The cooling action will reach the distance Δr in some time $\Delta\tau$. During this time inequality (3) will be fulfilled. But this contradicts inequality (2). The resulting contradiction proves the theorem, and thus the theorem is proved.
According to this theorem, the maximum grinding temperature is reached on the surface of the part, not inside. This means that defects caused by thermal phenomena can be detected from the outside. Moreover, if they are not on the surface, then there is no thermal damage inside the part. Consequently, finding the maximum temperature is reduced to calculating it only in the grinding zone on the surface of the part.
Therefore, I will consider a one-dimensional thermal model, where the maximum temperature is reached at the surface of the processed material. This greatly simplifies the solution to the problem. The purpose of the model is to find the maximum temperature on the surface of the part during grinding. It is important to be able to adjust the grinding parameters (time, depth, speed, thermal diffusivity of the cutting grain, etc.) and to carry out abrasive processing so as not to reach the temperature at which thermal defects of the part occur.
I then get the inequality:

$$Q_{cr} > Q_{max}, \quad (4.)$$

where Q_{max} is the maximum temperature on the surface of the part in the grinding zone, and Q_{cr} is the temperature at which thermal defects of the part begin (burns, microcracks, deformation, etc.). This temperature is referred to as the critical temperature.
Let me consider the operator

$$T: X_0 \to Q_{max}, \quad (5.)$$

where X_0 is a set of initial conditions or output data.
The model is studied under the assumption that the cutting grain has a cylindrical shape. Ellipses are obtained in their section when grinding. In unimportant cases, ellipses were replaced by circles to simplify calculations. After refining (1), the following equality was obtained:

$$Q_{max} = T(X_0) = 52.19(1 - b^*)\frac{\sqrt{\omega}}{\lambda}\frac{m^{0.05}P_z v}{\sqrt{v_1}bB^{0.4}}. \quad (6.)$$

The operator (5) allows the setting of the maximum temperature on the surface of the part in the grinding zone according to the values of the wheel and part speeds, the thermal diffusivity and thermal conductivity coefficients, the coefficient that characterizes the relative distribution of the grinding heat between the wheel and the part, and the force and dimensions of the contact area of the wheel with the part.
Such a mathematical model provides the possibility for the given initial data to calculate the missing data and find Q_{max}. Moreover, it allows one to analyze the effect on Q_{max} of changes in the initial conditions. The use of coolants can also be attributed to the initial conditions. They have a smell and therefore affect the purity of the air. Their disposal pollutes soil and groundwater. In addition to environmental problems, there are other problems associated with their use. Therefore, in my research I have tried to solve the problem without using coolants.
To meet the set research tasks, it became necessary to automate the implementation of the created mathematical model for determining the temperature on the surface of the part during grinding. To achieve this, I have developed a computer program that, after entering the initial conditions X_0 of the process of abrasive processing of the material, gives the result of the calculations. According to the analysed information needs in production, first of all the computerized algorithm should determine the highest temperature at the contact surface of the wheel with the part.

Model check

Consider task 1. Create a program for calculating the values (6) of operator (5).
First of all, I emphasize that my program allows for the user to enter the parameters of the grinding process. These include data on the material to be processed, the grinding tool, the type and mode of grinding, as well as the dimensions of the contact area of the wheel with the part. In this case, it is taken into account that the circle goes beyond the length of the workpiece being processed.
At the first stage, the program calculates the dimensionless Fourier complex using the formula:

$$F_0 = \frac{\omega_1 \cdot b}{10 \cdot v \cdot x_n^2},$$

where ω_1 is the coefficient of thermal diffusivity of grain, and x_n is found by the formula:

$$x_n = 0.875\bar{x}\sqrt[3]{0.6},$$

where $\bar{x}$ is the most probable grain size.
At the second stage, the algorithm determines the proportion of heat in the part $1 - b^*$, where b^* is found by the formula:

$$b^* = \frac{1}{1 + 2.25\frac{\lambda}{\lambda_1}A^*\sqrt{F_0}},$$

where λ is the thermal conductivity coefficient of the material being processed, and λ_1 is the thermal conductivity coefficient of the cutting grain, A^* is a function that depends on the time of contact of the grain with the part in one cut and the ratio of the thermal conductivity coefficients of the grain and the circle.
At the third stage, the program calculates the tangential force during grinding P_z, which is a function of the depth of grinding, the speeds of the part and the grinding disk, and the contact area of the wheel with the part. The formulas depend on how the part is machined.
Based on the data obtained, my program has all the necessary values to determine the highest temperature on the contact surface of the wheel with the part according to formula (6). Task 1 has been solved.

After obtaining the maximum temperature at the contact area between the grinding tool and the workpiece, it is necessary to compare it with the critical temperature according to formula (4). If it turns out that the maximum temperature of the part is higher than the critical one, then the grinding process cannot be carried out. To avoid negative consequences, the process must be optimized by changing the grinding parameters, such as speed. This will reduce the heat load and reduce the maximum temperature. The search for the optimal speed is implemented in the second part of the software product.

Consider task 2. Create a program to optimize the temperature process of grinding with a change in speed.

The program provides a critical temperature analysis based on user-defined input values. The algorithm calculates the maximum temperature at the contact surface and compares it with the critical temperature. When inequality (4) is satisfied, the program displays a message that the processing under the given conditions will be of high quality and will not bring any losses. Otherwise, the grinding parameters must be changed to avoid thermal damage to the part. This function is also implemented in my program by changing the speed of the part. The program calculates the speed at which the heating of the part will be decreased. As a result, the workpiece will not suffer thermal damage.

The solution to task 2 depends on the type of grinding, the material being processed, and the characteristics of the grinding wheel. For example, in the case of flat grinding of hard alloys with a cup diamond wheel, the program algorithm is based on formula (7):

$$v_1 = \left(\frac{\lambda Q_{max}}{31.31(1-b^*)\sqrt{\omega}\, m^{0.05} t^{0.69} v^{0.41} b^{0.18} B^{0.78} \prod_i K_i}\right)^{9,09}, \qquad (7.)$$

where $\prod_i K_i$ is the product of correction coefficients that take into account the bond of the wheel, the concentration of grains and the processed material. The corresponding coefficient is also taken into account in the case of liquid grinding. Task 2 has been solved.

Similarly, the problem of optimizing the temperature process of grinding is solved depending on the change in depth, grinding force, or characteristics of the wheel. If optimization is not possible under the given initial conditions, or the maximum temperature remains above the critical one, the program issues appropriate recommendations and suggests entering other initial parameters. One of the recommendations is the use of coolants.

Consider an example. **Fig. 1** shows the calculation by the program of the maximum temperature of a workpiece made of hard alloy BK8 during flat grinding with the butt face of a cup diamond wheel, a grain size 80/63, and an organic bakelite bond B1. The obtained temperature turned out to be lower than the critical one (614 < 690), which ensures high-quality processing of the part without thermal defects. Note that 614°C is predicted without the use of coolants. It should be emphasized that an experimental temperature value of 600°C was obtained with the same initial grinding parameters.

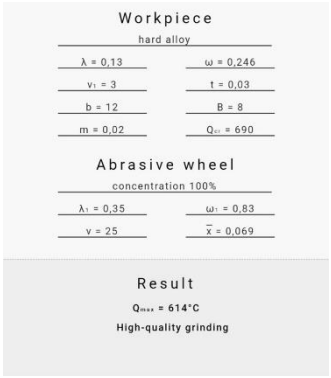

Fig. 1 Calculation of the maximum temperature

Technical features of the program

I have analysed the conditions for further use of the program. For maximum convenience and efficiency of work, I decided to organize the process of interaction with the program continuously. In other words, all input fields are always active, and the result is recalculated whenever the input data changes. This approach is most convenient in various situations in production using different types of devices. From the foregoing, it follows the need to support the software product on a large number of devices running different operating systems. To achieve this goal, the algorithm is implemented as a website, which makes it possible to work from any device with a web browser. Also, the user can enter data using the mouse and keyboard and using touch input. The result is displayed graphically equally well on colour monitors, laptop screens, tablets, and even monochrome displays. An integral advantage is the ability to modernize and expand the program without interfering with client devices on factories, limited only to changes on the server with the site.

Following the current trends in the development of sites using mathematical logic, JavaScript was chosen as the main programming language. It is a flexible tool with dynamic data typing and relatively high performance. It is currently supported by all known browsers and is a generally accepted standard in the field of creating web applications. JavaScript is an object-oriented language. This feature allows you to organize a program as a collection of objects, each of which is an instance of a certain class with support for an inheritance hierarchy.

An equally important part of the application is its appearance and the quality of the interface. I have paid enough attention to this aspect, which will allow even inexperienced users to intuitively interact with the program, as well as spend a minimum of time getting acquainted with the basic functions. At the same time, the speed of work increases, which is an important factor in mass production. The above was achieved using the modern standard of the hypertext markup language – HTML 5. This is the standard for web pages all over the world. The code is interpreted by browsers, and the resulting page is displayed on any display. Styling is applied to the created html document, implemented using a formal language for describing the appearance of web pages – CSS. The latest css3 standard provides the ability to use smooth animations and transitions, which improves the responsiveness of the interface.

The development of my software product was carried out using the editor Sublime Text 3. At the stage of creation, the project was thoroughly checked and tested in the Google Chrome web

browser. Moreover, the use of multi-browser solutions guarantees correct operation in any modern browser.
According to the implementation, there are two ways to run my program. The first one is to copy the project files to the client device and then open the html file in any browser. The described method does not require an Internet connection and does not depend on the performance of a third-party server. However, to update the algorithms of the program, it will be necessary to replace the project files on the device, which will require intervention in each computer or tablet. The second method involves the location of the project on the server. In this case, access to the program is carried out by going to the web address issued by the host provider. To do this, the client devices must have an Internet connection. If the server fails, the program will stop working. The advantage of this method is the convenience of upgrading and expanding the program. It is enough to update the files on the server, and all clients will have access to the new functions. In both cases, the same files are used. Thus, my development can be used in both ways, the choice of which depends on the status of the Internet connection.

CONCLUSION

It has been proven by contradiction that the maximum temperature is reached on the surface of the part during its grinding. The significance of this theorem also lies in the fact that if thermal damage is absent from the outside, then there is none inside the part. If the maximum temperature was reached inside, then the resulting damage might not be visible on the surface. Thus the problem of how to detect this maximum temperature would arise, along with many other problems. However, because the theorem states this is not possible, these problems do not arise by virtue of the theorem.
The considered model makes it possible to determine the maximum temperature of the part during grinding. Based on the model and analysis of parameters that affect the temperature rise of a metal part during grinding, a program has been created. It not only calculates the temperature, but also allows the user to ensure the optimal temperature process by varying the basic parameters of metal processing. If there is a possibility of negative consequences, the algorithm will determine that the maximum temperature on the surface of the part during grinding is higher than the critical one. Comparison of the values obtained experimentally and calculated by the program shows an adequate reflection of real temperatures in the process of grinding. Thus, the mathematical model simulates the process under study reasonably.

ACKNOWLEDGMENTS

Author would like to thank to Associate Professor A. V. Kotliar, PhD for the consultation.

REFERENCES

1. A. N. Reznikov: *Abrasive and diamond processing of materials*, Moscow: Mechanical Engineering, 1977.
2. E. N. Maslov: *Grinding materials theory*, Moscow: Mechanical Engineering, 1974.
3. A. N. Reznikov: *Thermal physics of materials machining processes*, Moscow: Mechanical Engineering, 1981.
4. J. L. Gonzalez-Santander, G. Martin: CIRP Annals-Manufacturing Technology, 2015, 2015, 1-13. http://dx.doi.org/10.1155/2015/150493.
5. J. Bidulska, T. Kvackaj, R. Bidulsky, M. A. Grande: High Temperature Materials and Processes, 27, 2008, 203-207. https://doi.org/10.1515/HTMP.2008.27.3.203.
6. R. Bidulsky, M. A. Grande, E. Dudrova, M. Kabatova, J. Bidulska: Powder Metallurgy, 59(2), 2016, 121-127. https://doi.org/10.1179/1743290115Y.0000000022.
7. Andrea Di Schino: Acta Metallurgica Slovaca, 26(3), 2020, 111-115. https://doi.org/10.36547/ams.26.3.564.
8. J. C. Jaeger: Proceeding of Royal Society NSW, 1942, 203-224.
9. A. S. Lavine: International Journal of Heat and Mass Transfer, 43(24), 4447-4456, 2000. https://doi.org/10.1016/S0017-9310(00)00024-7.
10. S. G. Rediko: *Heat generation processes when grinding metals*, Saratov: Saratov University, 1962.
11. P. D. Doan, T. B. Tran, Ch. D. Le, H. B. Tran: Acta Metallurgica Slovaca, 25(2), 2019, 123-129. https://doi.org/10.12776/ams.v25i2.1270.
12. Y. N. Nguyen, A.-T. Dao, M.-H. Le, Kh. Q. Dang, M. Nanko: Acta Metallurgica Slovaca, 25(3), 2019, 186-192. https://doi.org/10.12776/ams.v25i3.1313.
13. O. B. Girin, V. I. Ovcharenko, D. G. Korolyanchuk: Acta Metallurgica Slovaca, 25(4), 2019, 267-275. https://doi.org/10.12776/ams.v25i4.1357.
14. J. Bidulska, R. Bidulsky, M.A. Grande, T. Kvackaj: Materials, 12(22), 2019, 3724. https://doi.org/10.3390/ma12223724.
15. M. K. Pal, A. Vikram, V. Bajaj: Acta Metallurgica Slovaca, 25(4), 2019, 253-258. https://doi.org/10.12776/ams.v25i4.1359.
16. J. Petrík, P. Blaško, A. Vasilňaková, P. Demeter, P. Futaš: Acta Metallurgica Slovaca, 25(3), 2019, 166-173. https://doi.org/10.12776/ams.v25i3.1310
17. R. Bidulsky, M.A. Grande, J. Bidulska, T. Kvackaj: Materiali in Tehnologije, 43(6), 2009, 303-307.
18. Y. Kalinin et al.: Acta Metallurgica Slovaca, 25(2), 2019, 114-122. https://doi.org/10.12776/ams.v25i2.1269.
19. P. Petrousek et al.: Acta Metallurgica Slovaca, 25(4), 2019, 283-290. https://doi.org/10.12776/ams.v25i4.1366.
20. H. Leitner, M. Schober, R. Schnitzer, S. Zinner: Materials Science and Engineering, 528(15), 2011, 5264-5270. https://doi.org/10.1016/j.msea.2011.03.058.
21. E. V. Pezeloma, A. Shekhter, M. K. Miller, S. P. Ringer: Acta Materialia, 52(19), 2004, 5589-5602. https://doi.org/10.1016/j.actamat.2004.08.018.
22. D. L. Skuratov et al.: Applied Mathematical Modelling, 31(6), 1039-1047, 2007. https://doi.org/10.1016/j.apm.2006.03.023.